

# Manipulation of Superparamagnetic Microbeads on Soft Magnetic Microchips

Dissertation

zur Erlangung des akademischen Grades Doktor der  
Ingenieurwissenschaften (Dr.-Ing.)



Faculty of Engineering  
Christian-Albrechts-Universität zu Kiel

Umer Sajjad

2018



## **Reviewers:**

1. Reviewer: Prof. Dr.-Ing. Jeffrey McCord
2. Reviewer: Prof. Dr. Christine Selhuber-Unkel

Date for the oral exam: 10.12.2018





# Abbreviations

<b>SPM</b>	superparamagnetic	<b>MACS</b>	magnetically activated cell sorting
<b>FG</b>	field gradient	<b>LoC</b>	lab on chip
<b>MB</b>	microbead	<b>CTCs</b>	circulating tumor cells
<b>MBs</b>	microbeads	<b>MOKE</b>	magneto optical Kerr effect
<b>MT</b>	magnetic track	<b>MM</b>	micromagnetic
<b>MA</b>	magnetic array	<b>MFM</b>	magnetic force microscopy
<b>MS</b>	magnetic structure	<b>ccw</b>	counter clockwise
<b>MSs</b>	magnetic structures	<b>2-D</b>	two dimensional
<b>TMS</b>	trisymmetric magnetic structures	<b>1-D</b>	one dimensional
<b>HMS</b>	hexasymmetric magnetic structures	<b>NiFe</b>	Ni <sub>81</sub> Fe <sub>19</sub> , Permalloy
<b>MPM</b>	magnetophoretic mobility	<b>FeCoSiB</b>	Fe <sub>70.2</sub> Co <sub>7.8</sub> Si <sub>12</sub> B <sub>10</sub>



# Symbols

$M$	magnetization	$F_{mag}$	magnetic force
$H_{ext}$	externally applied magnetic field	$F_{drag}$	hydrodynamic drag force
$H_{str}$	stray magnetic field	$\varphi_H$	magnetic field angle
$H_{s,z}$	stray magnetic field in the z-direction	$\varphi_{MB}$	bead angle
$\left  \frac{dH_{s,z}}{dz} \right $	magnetic field gradient in the z-direction	$\varphi_{sw}$	opening angle or bisect angle of switching field
$f_{rot}$	rotational frequency of the field	$\Delta$	angular phase lag between applied field and moving bead
$f_{crit}$	critical frequency of moving bead	$\Delta_{lock}$	phase lag locked at a fixed field frequency
$f_{swit}$	switching frequency of applied field	$\phi$	angle between magnetic arrays
$\alpha$	orientation of the applied rotating field	$v_{ave}$	average velocity of bead
$\varnothing_{MB}$	diameter of microbead	$\Delta x$	cumulative distance traveled along MT
$p_{MB}$	position of the microbead	$\chi_v$	magnetic volume susceptibility of a single MB
$\lambda$	periodic length of the structure		





# Abstract

Labeling of biological analytes (e.g. protein, DNA) with superparamagnetic microbeads (SPM-MBs) serves as a handling tool in microfluidic lab-on-chip applications. Using an externally applied magnetic field  $H_{ext}$ , the separation of bio-labeled MBs on magnetic structures (MSs) of a chip is an emerging trend in biomedical research and to realize the future diagnostic tools. However, a high separation efficiency of mixed MBs populations together with a high throughput is a bottleneck, limiting the adaptability of these devices. Freely movable MBs with a control over single MBs can simplify the size dependent MBs' separation. Enabling the manipulation of MBs' population on a magnetic chip can offer a high separation efficiency and thus, fast and accurate diagnostics of differently labeled analytes.

This thesis presents manipulation techniques of MBs on soft magnetic microchips in a flow-less aqueous medium. Starting with the circulating motion of a single MB around a magnetic MS, the response is accurately reproduced by simulating the MB movement patterns. These findings laid the foundation of MBs motion along a 1-D magnetic array. Using the symmetrically (asymmetrically) in-plane rotating field on magnetic arrays, composed of asymmetric (symmetric) MSs, the underlying directed movements of MBs are revealed. Individual MBs with different sizes are moved with different speeds along 1-D magnetic tracks, indicating the separation opportunities. It is possible to maximize the transport speed with an appropriate geometric combination of the magnetic track and the magnetic particle.

The experimentally acquired motion patterns of MBs are phenomenologically explained by micromagnetic MM simulations, magnetic force microscopy MFM measurements and magneto-optical Kerr effect MOKE imaging. 2-D periodic distribution of triangular MSs enables a free motion of MBs to a chosen location along the trisymmetric pathways on a chip. A simultaneous two-way motion of different sized MBs results in a cell sorting possibility. Selective transport of mixed populations of MBs is achievable with a separating efficiency of more than 97%.

Circular MSs in the hexasymmetric 2-D arrangement enable the driving of a single MB and its population by means of an elliptically rotating  $H_{ext}$  in the chip plane. Adjusting the strength and orientation of  $H_{ext}$  can steer the moving MBs in multiple directions on the magnetic surface. The developed novel structures have provided the first possibility of a simultaneous separating motion of three different sizes of MBs in three lateral directions. Finally, to confirm the functionality of these magnetic surfaces, an example of a MB inside a *Dictyostelium* amoeba is shown for a selectable directed movement on triangular MSs.



# Zusammenfassung

Zur Analyse biologischer Substanzen, wie z.B. von Proteinen oder von DNA, mittels Lab-on-Chip Systemen, werden häufig Marker aus superparamagnetischen Microbeads (SPM-MBs) verwendet. Ein aufkommender Trend zur Realisierung zukünftiger Diagnoseinstrumente in der biomedizinischen Forschung besteht darin, durch SPM-MBs markierte Analyte anhand von Magnetfeldern auf funktionalisierten Oberflächen gezielt zu trennen. Eine Herausforderung, die den Einsatz gegenwärtig erschwert, besteht darin, einen hohen Analytendurchsatz mit gleichzeitig hoher Trenneffizienz zu realisieren. Die Kontrolle von einzelnen frei beweglichen MBs kann z.B. dazu genutzt werden, um eine größenabhängige Trennung der Beads zu erreichen. Wird die Bewegung ganzer Gruppen von MBs auf magnetischen Oberflächen beherrschbar, so kann eine hohe Trenneffizienz und damit eine schnelle und genaue Analyse von unterschiedlich markierten Substanzen erreicht werden.

In dieser Dissertation werden Methoden zur kontrollierten Bewegung von MBs auf weichmagnetischen strukturierten Oberflächen untersucht. Die Untersuchung der kreisenden Bewegung eines einzelnen MBs um eine runde Struktur liefert experimentelle Daten, die durch die simulierten Mikrobeadbewegungsmuster treffend beschrieben werden können. Diese Ergebnisse liefern die Grundlage für die Realisierung der Bewegung von MBs entlang eindimensionaler magnetischer Strukturen. Durch die Verwendung von symmetrischen Magnetfeldern an asymmetrischen Strukturen, bzw. der Verwendung von asymmetrischen Feldern an symmetrischen Strukturen, kann eine gerichtete Bewegung von MBs erreicht werden. Einzelne MBs verschiedener Größe können mit unterschiedlichen Geschwindigkeiten entlang eindimensionaler Strukturen bewegt werden. Daraus ergibt sich die Möglichkeit zur Trennung von MBs. Außerdem wird gezeigt, dass die Geschwindigkeit von MBs durch eine optimierte Geometrie der Strukturen bezüglich der MBs maximiert werden kann.

Die experimentell bestimmten Bewegungsmuster werden phänomenologisch und durch mikromagnetische Simulationen, magnetische Rasterkraftmikroskopie und magneto-optische Kerr-Effekt-Mikroskopie erklärt. Magnetische Dreieckstrukturen auf periodisch strukturierten Oberflächen ermöglichen die gezielte Bewegung von MBs entlang der Strukturkanten der Elemente. Die gleichzeitige Bewegung unterschiedlich großer MBs in entgegengesetzten Richtungen ermöglicht die effiziente Trennung von markierten Substanzen, wie z.B. von biologischen Zellen, von Proteinen oder von DNA. Hierdurch ist die Trennung in Gruppen gleichgroßer MBs mit einer Genauigkeit von 97% erreicht worden.

Kreisrunde Strukturen in einer hexagonalen periodischen Anordnung ermöglichen

die gerichtete Bewegung sowohl eines einzelnen MBs, als auch ganzer Gruppen mit Hilfe elliptisch rotierender Magnetfelder. Durch Anpassung der Feldstärke und Richtung des externen Magnetfeldes kann eine kontrollierte Bewegung der MBs entlang unterschiedlicher Richtungen auf der Chipoberfläche erreicht werden. Somit ermöglichen die entwickelten Strukturen und Feldprozeduren erstmalig die laterale Trennung von drei unterschiedlich großen MBs. Schlußendlich wird, zur Bestätigung der Anwendbarkeit der entwickelten Methoden am Beispiel einer mit einem MB markierten *Dic-tyostelium* Amöbe, die gezielte und gerichtete Bewegung auf magnetischen Strukturen demonstriert.

# Contents

<b>Abbreviations</b>	<b>i</b>
<b>Symbols</b>	<b>iii</b>
<b>Abstract</b>	<b>v</b>
<b>Zusammenfassung</b>	<b>vii</b>
<b>1 Introduction and Fundamentals</b>	<b>1</b>
1.1 Introduction . . . . .	1
1.1.1 State-of-the-art . . . . .	2
1.1.2 Research Goals . . . . .	4
1.1.3 Thesis Contents . . . . .	5
1.2 Fundamentals . . . . .	6
1.2.1 Magnetic Materials for Microchip Surfaces . . . . .	6
1.2.2 Forces and Energies in Magnetic Microchips . . . . .	7
1.2.3 Superparamagnetic Microbeads . . . . .	8
1.2.4 Microbeads . . . . .	10
1.2.5 Forces on a Microbead . . . . .	11
<b>2 Numerical and Experimental Methods</b>	<b>15</b>
2.1 Micromagnetic Calculations . . . . .	15
2.1.1 Magnetization and Stray Magnetic Field . . . . .	15
2.1.2 Absolute Stray Field Gradient in z-direction . . . . .	16
2.2 Fabrication of Magnetic Structures . . . . .	17
2.3 Experimental Methods . . . . .	18
2.3.1 Magneto-optical Kerr Effect Microscopy . . . . .	18
2.3.2 Magnetic Force Microscopy Imaging . . . . .	18
2.3.3 Experimental Setup . . . . .	20
<b>3 Microbead Motion on Single Magnetic Structures</b>	<b>21</b>
3.1 Magnetomechanics of a Microbead . . . . .	21
3.1.1 Circular Pattern as a Model Structure . . . . .	21
3.1.2 Microbead Looping . . . . .	22

3.1.3	Numerical Modelling of Microbead Motion . . . . .	23
3.2	Characterization of Magnetic Microbeads . . . . .	27
3.3	MB Circulating Motion Dependence on Magnetic Structures . . . . .	29
3.3.1	Angular Phase Lag of Moving Microbeads . . . . .	31
3.4	Microbead Transport on Magnetic Tracks . . . . .	32
3.4.1	Directed Transport on a Curvilinear Track . . . . .	33
3.4.2	Directed Transport on a Zigzag Track . . . . .	36
3.4.3	Directed Transport on a Convex Track . . . . .	39
3.4.4	Directed Transport on a Concave-pointed Track . . . . .	43
3.4.5	MB Velocity Dependence on $H_{ext}$ Amplitude and Track Size . . . . .	46
<b>4</b>	<b>Microbead Motion on 1-D Magnetic Arrays</b>	<b>49</b>
4.1	1-D Motion based on Structures' Asymmetry . . . . .	50
4.1.1	1-D Motion on an Array of Asymmetric Structures . . . . .	50
4.1.2	MB Velocity on an Array of Asymmetric Structures . . . . .	51
4.2	Directed Motion based on Applied Field's Asymmetry . . . . .	52
4.2.1	Directed Motion on an Array of Symmetric Structures . . . . .	53
<b>5</b>	<b>2-D Movement of Microbeads on a Trisymmetric Magnetic Surface</b>	<b>55</b>
5.1	Trisymmetric Magnetic Patterns . . . . .	56
5.1.1	Stray Magnetic Fields on Triangular Patterns . . . . .	56
5.1.2	Bidirectional Motion of Microbeads . . . . .	57
5.2	Motion Dependence on Geometric and Magnetic Configurations . . . . .	60
5.2.1	Transport Velocity of Microbeads . . . . .	61
5.2.2	Microbeads Separation Schemes . . . . .	65
5.3	Trilateral Transport of Microbeads . . . . .	69
5.3.1	Selective Movement of MBs from a Mixture . . . . .	70
<b>6</b>	<b>Multilateral Motion of Microbeads on a Hexasymmetric Magnetic Surface</b>	<b>75</b>
6.1	Hexasymmetric Magnetic Surface . . . . .	76
6.2	Trilateral Motion of a Microbead . . . . .	77
6.3	Trilateral Separation of Multiple Size Microbeads . . . . .	79
<b>7</b>	<b>Magnetic Manipulation of a Social Amoeba (Cells)</b>	<b>83</b>
<b>8</b>	<b>Conclusions and Outlook</b>	<b>87</b>
<b>Appendix-A</b>		<b>viii</b>
A.1	Phase Lag Dependence on the Speed of a Microbead . . . . .	viii
A.2	Normalized Magnetization of Single Microbeads with Different Sizes . . . . .	ix
A.3	Linear Increase and Decrease in the Velocity of a MB . . . . .	x
A.4	$H_{ext}$ Amplitude defining the MB's Velocity on Zigzag Tracks with $\alpha = \pi / 2$	xi
A.5	$H_{ext}$ Amplitude defining the MB's Velocity on Zigzag Tracks with $\alpha = \pi / 3$	xii
A.6	$H_{ext}$ Amplitude defining the MB's Velocity on Curvilinear Tracks . . . . .	xiii
A.7	$H_{ext}$ Amplitude defining the MB's Velocity on Convex and Concave Tracks	xiv

<b>Appendix-B</b>	<b>xv</b>
B.1 MFM Imaging on Egg-shaped Magnetic Structures . . . . .	xv
B.2 Varying Critical Frequencies of Single MBs on a 1-D Magnetic Array .	xvi

<b>Appendix-C</b>	<b>xvii</b>
C.1 Local deviation in Magnetization and the Resultant Field Gradient . .	xvii
C.2 Motion of MBs' Ensembles under Symmetric and Asymmetric Fields .	xviii
C.3 Inversion of a MB's Directed Motion with an Inversion of Field Direction	xix
C.4 MBs' High Yield Transport and Patterning Possibilities . . . . .	xx

<b>Appendix-D</b>	<b>xxi</b>
D.1 Trilateral Movement Patterns of a MB . . . . .	xxi
D.2 Trilateral Separation of Multiple MBs . . . . .	xxii
D.3 MBs' Motion Depending on the Rotational Frequency of Applied Field	xxii
D.4 Hexalateral Motion for a MB based on the Chip Rotation . . . . .	xxiii

<b>Appendix-E</b>	<b>xxiv</b>
E.1 Movie Captions . . . . .	xxiv
E.1.1 Movies-Chapter 3 . . . . .	xxiv
E.1.2 Movies-Chapter 4 . . . . .	xxv
E.1.3 Movies-Chapter 5 . . . . .	xxv
E.1.4 Movies-Chapter 6 . . . . .	xxvii
E.1.5 Movies-Chapter 7 . . . . .	xxvii

<b>Acknowledgments</b>	<b>xxviii</b>
<b>Publication and Conference</b>	<b>xxix</b>
<b>Bibliography</b>	<b>xxx</b>



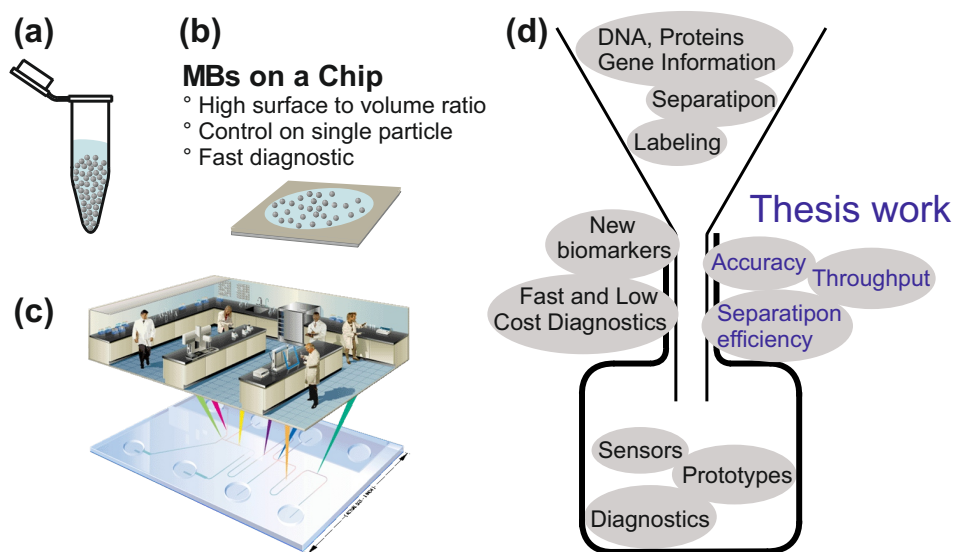


# Chapter 1

## Introduction and Fundamentals

### 1.1 Introduction

Since the emergence of superparamagnetic nanoparticles, the field of biotechnology dealing with the handling of biological entities has seen major developments. Remote control of localized magnetic forces brings magnetism and microfluidics together. Tagging of superparamagnetic-microbeads SPM-MBs with biological cells helps in their separation in a fluidic environment, for example in a reaction vessel (Fig. 1.1 a). With a high surface to volume ratio of magnetic microbeads on a chip (Fig. 1.1 b), a control on single cells and their populations can be achieved to integrate the laboratory procedures on a cm-sized portable device (Fig. 1.1 c).<sup>1-3</sup> However, handling magnetically labeled biological analytes on a magnetic surface has certain challenges. Particularly, the separation of MBs is considered a bottleneck to the adaption of magnetic chip based diagnostic tools (Fig. 1.1 d).<sup>4,5</sup>



**Figure 1.1:** Sketch of MBs in a reaction vessel (a) and on a chip (b). (c) Lab-on-chip concept. Image from Ref. 6. (d) The focus of this thesis is depicted.

Using micromagnetic thin-film structures, highly localized and strong magnetic forces can be created down to the sizes of single magnetic micro- and nanoparticles.<sup>5</sup> Conjugated with the magnetic particles, the biological analytes (e.g. protein, DNA, CTCs) can be transported, sorted and diagnosed on a chip surface. The controlled and selectable motion of magnetic particles on the surface of a magnetic chip is an emerging trend in fundamental research and lab-on-chip applications.<sup>4,5</sup>

This thesis presents the realization of new magnetic microchip concepts for the free transport and separation of magnetic microbeads on a chip surface. The basic principle of the MB motion on a magnetic surface is as follows: A balance between the Zeeman Energy (due to applied magnetic field  $H_{ext}$ ) and the demagnetizing field of a magnetic pattern ( $H_d$ , a function of shape) creates the magneto-static potential and stray field gradient around the magnetic pattern. Suspended in an aqueous medium a single magnetic MB attracts toward the highest field gradient. After the MB is positioned on the magnetic chip, it can be moved along the traveling and changing magnetic potential energy landscape with varying order of  $H_{ext}$ . Control parameters, strength, orientation and frequency of the moving  $H_{ext}$  and additionally the size of MBs and magnetic structures enable the motion and separation of MBs on magnetic patterns.

### 1.1.1 State-of-the-art

In the 1990s, parallel processing of genes for clinical diagnosis<sup>7</sup> and use of magnetic bead-based separation technologies were rising.<sup>8</sup> Meanwhile, miniaturized total chemical analysis system ( $\mu$ TAS) facilitated the integration of laboratory processes on a single device for the separation and fast processing.<sup>9</sup> Particularly, the size of micro-channels on a chip was realized for the detection of target analytes from complex  $\mu$ l samples.<sup>1</sup> Microbeads based immunosorbent assays reduced the processing time from a day to an hour and are presently a usual practice for labeling biological cells.<sup>2,3</sup> Manipulation of magnetically labeled blood cells with in-channel magnetic tracks was adapted for its higher sensitivity over flow cytometer.<sup>10</sup> These technological developments led to the commercialization of magnetic-activated cell sorting MACS.<sup>11</sup>

In the 2000s, the motion of magnetic<sup>12-14</sup> and non-magnetic microparticles<sup>15</sup> on magnetic and electromagnetic microchips<sup>16</sup> became an alternative to flow based MBs separation. Main motivation was achieving a control over the motion of single MBs<sup>14</sup> and their populations<sup>13</sup> by creating localized magnetic forces from on-chip micromagnets. Meanwhile, a trend of using circuit-less magnetic chips<sup>15</sup> (immunity of external magnetic fields)<sup>17</sup> against the electromagnets (adverse effects of electric currents)<sup>18</sup> was on its rise.

The last decade has seen an enormous development in magnetic labelled bio-analytes in flow-based devices. Living cells were separated in flowing suspension with external hard magnets.<sup>19</sup> Separation speed and efficiency of blood cells were improved with channeled ferromagnetic structures.<sup>20</sup> High throughput and multiple target separation were achieved.<sup>21</sup> On-chip magnetic structures based flow-less manipulation of

MBs also advanced greatly from labeling of bioanalytes to their separation and sensing.<sup>4,5</sup> The combination of flow with the magnetic surfaces facilitated the transport of sorted cells in a droplet<sup>22</sup> and improved the separation speed and efficiency.<sup>23</sup>

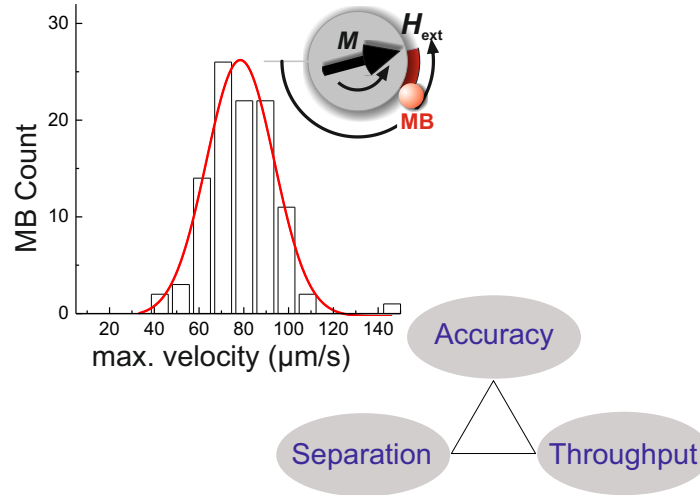
Recent works report on magnetic chip based high throughput<sup>24</sup> and detection<sup>25</sup> of labeled magnetic MBs. However, the MBs separation is still considered a hurdle to the implementation of magnetic chip based technology.<sup>5</sup> Magnetically labeled CTCs were quantitatively sorted.<sup>26</sup> Yet, the far lower efficiency than flow-based methods is likely related to the lack of control on single MBs. Moreover, the heterogeneity of magnetic nano-<sup>27</sup> and microparticles,<sup>28-30</sup> causes the reduced separation efficiency and limited reproducibility. With the quantification of heterogeneous response of single MBs,<sup>31</sup> a solution and/or compensation to the magnetic heterogeneity has been an open question. This clarifies why most of existing cell sorting techniques rely on ensemble averaging. With the ensemble averaged analysis, the information about the single entity is lost.<sup>5</sup> Different types of single MBs were simultaneously separated,<sup>32</sup> but the separation of MBs populations might be challenging on the same system, again, due to the magnetic heterogeneity. Therefore, an on-chip system providing the control on MBs population is highly desirable to avoid ensemble averaging.<sup>5</sup> This requires new ways of separating single beads along with a control over the beads' population, so that improved separation efficiency and thus, accurate diagnosis can be realized.

Accuracy to capture rare type cells is a primary criterion for the selection of cell sorting technologies.<sup>33</sup> Due to individual pros and cons of MACS and other sorting technologies, a combination of high purity, efficiency and throughput is challenging.<sup>34</sup> Nonetheless, MACS seems to bring a promising future for low cost devices, if the problems like cell purification at the population level along with selectivity and throughput are solved.<sup>11</sup>

On the application side, a point-of-care (PoC) device must meet all the requirements of ASSURED (affordable, sensitive, specific, user-friendly, rapid and robust, equipment-free and delivered) standard published by world health organization WHO, to realize easy and home-usable diagnosis of chronic diseases.<sup>35,36</sup> In general, the existing PoC platforms including the magnetic particles based devices, may fail to meet the ASSURED criteria. In the technological context, a magnetic surface based device can contribute to the improved specificity and speed of the device. Although, in their early stage of development, these few cm-sized LoC and PoC devices have great potential to deal with the challenges for the control of chronic diseases.<sup>35,36</sup>

Over the last decade, a gradual increase in citations on topic of human cell sorting and purification is reported.<sup>34</sup> Meanwhile, a minor research contribution related to the magnetic separation, comparing to an exponential growth of studies related to the use of magnetic particles, indicate that more research is required to develop the separation technologies.<sup>37</sup> Researchers and experts from various disciplines are working together to reach the multidimensional goals of magnetic particles based LoC techniques. The development in LoC systems is not necessarily to replace conventional laboratory systems. LoC technologies can solely contribute to the research in biotechnology, e.g. the identification and validation of new biomarkers.<sup>35,38</sup>

### 1.1.2 Research Goals



**Figure 1.2:** MBs manipulation triangle depicting three prerequisites of a magnetic surface based LoC device. Single MBs circulating around a magnetic structure show strongly varying velocity due to magnetic heterogeneity. This hinders the separation of multiple type beads. Together with the accurate response of MBs, the achievable separation and throughput define the overall functionality of a magnetic surface.

**1. Accuracy** Reproducibility of the motion trajectory of a microbead confirms its accurate response on a magnetic chip. However, another MB of same type moves  $\approx 1.5\times$  faster or slower, due to the magnetic heterogeneity.<sup>27–31</sup> To achieve the separation of different types of MBs becomes increasingly challenging. A unison motion of MBs' ensembles is one of the goals of this research.

**2. Separation** To obtain the reproducible separating motion of different MBs thorough knowledge of magnetic heterogeneity is essential. Understanding the degree of deviating motion among MBs individual populations can help in finding a solution to this problem. A suitable combination of control parameters (size and shape of magnetic structures, amplitude and sequence of external magnetic fields) can reveal the underlying separation possibilities on magnetic surfaces.

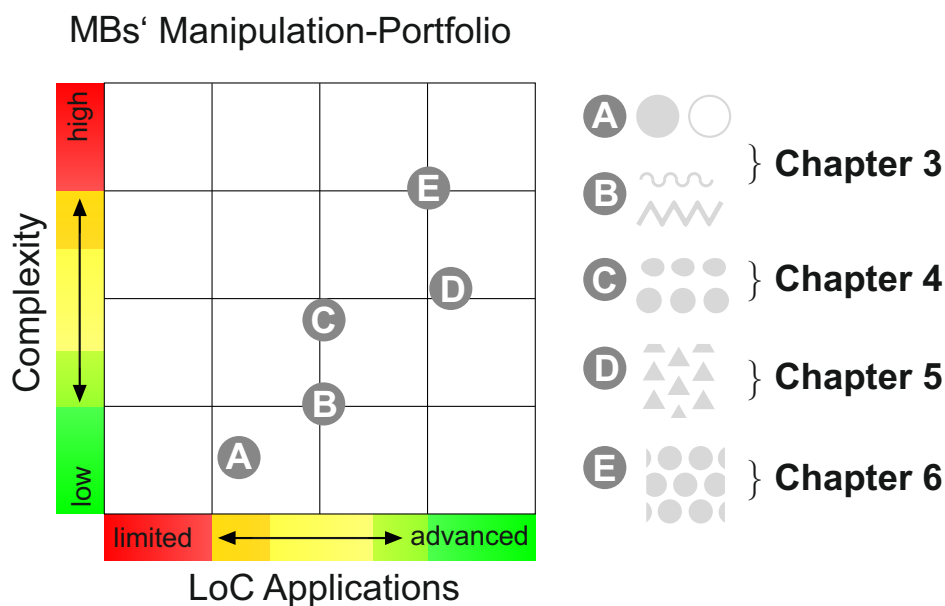
**3. Throughput** In continuous flow-based magnetic manipulation schemes, throughput is defined as the amount of fluid sample processed in time (e.g.  $\mu\text{L}/\text{min}$ ).<sup>39</sup> In a stagnant suspension, the high density of biological cells processed per area of a chip increases the performance of the manipulation scheme.<sup>24</sup> Yet, the continuous flow based devices are preferred due to their high processing speed.<sup>4</sup> The problem of a low processing speed in flow-less manipulation methods can be addressed with MSs distributed all over the chip.<sup>4</sup> Hexagonally arranged MSs offer the densely packed positioning sites for single MBs. However, the faster moving magnetic particles show higher degree of magnetic heterogeneity. The separation of different types particles together with high throughput is challenging on closely packed MSs on a chip.

The main goal of this research work is to enable the separation of mixed magnetic particles on magnetically patterned chip surfaces using various sequences of an

externally applied magnetic field. Originating from the heterogeneous magnetic response, the separation of different types of MBs becomes complicated on 2-D magnetic patterns. With the accurate and reproducible motion paths of different MBs, a compromise between the achievable separation efficiency and the high throughput is determined on various magnetic microchip platforms.

### 1.1.3 Thesis Contents

**Chapter 1** includes the introduction followed by the State-of-the-art covering developments in the magnetic MBs' manipulation from early works to recent time. Then, a short overview of the energies and forces present during the MB motion in the microfluidic cell is given. **Chapter 2** deals with the numerical and experimental procedures adapted to perform this research. Chapter 3-7 present the MBs motion on various magnetic structures, each with the specific focus on functionalities such as selectable directed motion and separation of mixed MB. The MBs' manipulation portfolio in Fig. 1.3 depicts achievable functionalities on these magnetic structures for increasing complexity in the MBs' manipulation from their motion on individual structures to the 2-D magnetic surfaces. **Chapter 3** covers the simple MB motion on circular patterns and guided MB motion on magnetic tracks with various geometries. **Chapter 4** deals with the MB directed motion on 1-D magnetic arrays. A simultaneous bidirectional motion at the single MB level and a high separation efficiency of MBs' populations on a trisymmetric 2-D magnetic surface is shown in **Chapter 5**. **Chapter 6** presents the simultaneous multilateral motion of multiple-sized MBs on a hexasymmetric 2-D magnetic surface. **Chapter 7** presents the proof of concept for a magnetic surface by the selectable transport of a *Dictyostelium* cell with a single magnetic MB inside it. Finally, **Chapter 8** concludes the report with suggestions for future works.



*Figure 1.3: MBs' manipulation portfolio defining the functionalities of various magnetic surfaces.*

## 1.2 Fundamentals

### 1.2.1 Magnetic Materials for Microchip Surfaces

Micro-lithographically patterned ferromagnetic structures are commonly used to manipulate magnetic micro- and nanoparticles. With controllable magnetization in thin films micromagnets, the magnetic forces can be generated at a single particle level on a chip. The basic difference among the conventionally used magnetic materials lies in the ease with which they are magnetized under an applied field. If the magnetic saturation of a material is achievable at a small applied magnetic field, then the material is *magnetically soft*. If the saturation of a magnetic material needs larger applied field, then the material is said to be *magnetically hard*.<sup>40</sup>

An advantage of the hard ferromagnet is that the magnetic particles can be manipulated with very low external field (4 kA/m) using the underlying magnetization of patterns.<sup>41</sup> After the field is removed, magnetic domains align themselves due to the shape of magnetic element and maintain their magnetization  $M$  due to high coercivity. With no external field present, the inhomogeneous  $M$  of domain walls in hard ferromagnetic element, e.g. in zigzag wires act as trapping sites for magnetic particles.<sup>41</sup> This enables the predefined positioning of particle on the chip surface. However, a high external field (800 kA/m) is required to change the initial magnetization.<sup>4,41</sup>

Soft magnetic materials can be magnetized and demagnetized at small amplitudes of an applied magnetic field. With the negligible uniaxial magnetic anisotropy, soft micromagnets allow a control on the magnetization configurations due to the element's shape. The magnetic domains in soft magnetic thin film patterns can be created, modified and removed, all in low external magnetic fields. The polarized edges in a soft magnetic disk-shaped pattern can confine and move the particle freely with the changing position of  $H_{ext}$ .<sup>42</sup>

In this work, the magnetic materials are chosen based on their high magnetic permeability and low coercivity. Soft ferromagnetic materials ( $\text{Ni}_{81}\text{Fe}_{19}$ ,  $\text{Fe}_{70.2}\text{Co}_{7.8}\text{Si}_{12}\text{B}_{10}$ ) with the film thickness of 30 nm and 50 nm were utilized for the manipulation of magnetic particles. Permalloy ( $\text{Ni}_{81}\text{Fe}_{19}$ ) is a conventional soft magnetic material with the saturation polarization  $J_s = 1$  T.  $\text{Fe}_{70.2}\text{Co}_{7.8}\text{Si}_{12}\text{B}_{10}$  has  $J_s = 1.6$  T. In the absence of external magnetic field magnetic microbeads are observed magnetically free on the soft magnetic NiFe and FeCoSiB patterns.

On a 2-D patterned magnetic surface, the motion is programmed with the changing sequences of  $H_{ext}$ .<sup>24,43</sup> However, utilizing the changing strength and orientation of a continuously moving  $H_{ext}$  to manipulate the magnetic features of 2-D periodic structures remains unexplored. At the working magnetic field,<sup>42</sup> the magnetic domain states of NiFe soft magnetic patterns can be completely engineered in space (changing polarization with the amplitude of  $H_{ext}$ ) and time (motion with the changing direction of  $H_{ext}$ ) for the MB manipulation on the chip surface. With appropriate size and geometry, 2-D ferromagnetic structures can move MB populations, independent of the spatial history of individual MBs on the chip.

## 1.2.2 Forces and Energies in Magnetic Microchips

### Magnetic Energy Terms

Magnetic domain structures in a ferromagnetic material result from the minimization of its total energy given by the competing contributions of the following energy terms.

### Exchange Energy

Exchange energy is the reason for the spontaneous ordering of adjacent atomic magnetic moments in a ferromagnet resulting in a net magnetization. Exchange energy is defined as an exchange interaction between two spins  $S_i$  and  $S_j$  of neighboring atoms.<sup>44</sup>

$$e_{ex} = -2J_{ij}S_i \cdot S_j \quad (1.1)$$

where  $J_{ij}$  is the exchange constant between two adjacent spins. In a continuum approximation, the exchange energy for the sum of all adjacent spins can be written as an integral over the volume ( $V$ ) of the material.<sup>44</sup>

$$E_{ex} = \int_V e_{ex} dV = A \int_V (\nabla M/M_s)^2 dV \quad (1.2)$$

$(\nabla M/M_s)^2 = (\nabla M_x/M_s)^2 + (\nabla M_y/M_s)^2 + (\nabla M_z/M_s)^2$  for an isotropic material.  $A = \frac{JS^2}{a}$  is the exchange stiffness and  $a$  is the lattice constant for a cubic structure. The exchange length  $l_{ex}$  defines the shortest scale on which the magnetization can be twisted.<sup>44</sup>

$$l_{ex} = \sqrt{\frac{A}{\mu_0 M_s^2}}. \quad (1.3)$$

The value of  $l_{ex}$  is 2.4 nm, 5.1 nm and 3.4 nm for Ni, Fe and NiFe.<sup>44</sup>

### Anisotropy Energy

The magnetic anisotropy energy of a ferromagnetic material is defined by the tendency to which the magnetization direction in a magnetic domain is restrained to lie along an easy axis<sup>44</sup>

$$E_a = K_1 \sin^2 \theta \quad (1.4)$$



where  $\theta$  is the angle between the magnetization and the anisotropy axis.  $K_1$  is the anisotropy constant and has units  $J m^{-3}$ . For soft magnetic materials near-zero anisotropy is required. The magnetic softness of NiFe is due to a low value of its hardness parameter  $\kappa$ .<sup>44</sup>

$$\kappa = \sqrt{\frac{|K_1|}{\mu_0 M_s^2}} \quad (1.5)$$

The parameter  $\kappa$  the ratio between the anisotropy energy and the dipolar energy. The value of  $\kappa$  for Ni, Fe and NiFe are 0.12, 0.13 and 0.01 respectively.<sup>44</sup>

### Demagnetizing Energy

In the absence of an applied magnetic field, a ferromagnetic structure tends to minimize its self energy by forming magnetic domains. For a magnetization distribution, there exists a demagnetization field  $H_d$  in the opposite direction due to the shape of the magnetic pattern. Demagnetizing energy resulting from the interaction of magnetization and demagnetization field  $H_d$  is written as

$$E_d = -\frac{1}{2} \int_V \mu_0 \vec{H}_d \cdot \vec{M} dV \quad (1.6)$$

With the expression  $\nabla \cdot H_d = -\nabla \cdot M$  it becomes clear how the stray magnetic field relates to the distribution of the local magnetization in the magnetic structure. The integration over all space leads to  $-(\vec{H}_d \cdot \vec{M}) = \vec{H}_d^2$

### Zeeman Energy

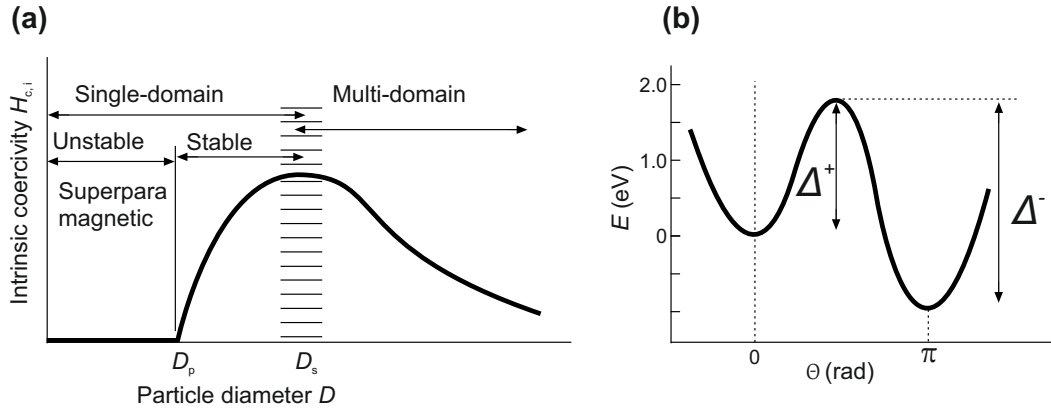
Zeeman energy results as an interaction between the externally applied magnetic field  $H_{ext}$  and the magnetization  $M$  of the material. The alignment of the magnetization along the field direction causes a reduction in the Zeeman energy  $E_{ze}$ .

$$E_{ze} = - \int_V \vec{H}_{ext} \cdot \vec{M} dV \quad (1.7)$$

## 1.2.3 Superparamagnetic Microbeads

### Superparamagnetism

A ferromagnetic body forms domains by reducing the stray field energy at the cost of increased exchange energy at the wall between domains. If the volume of the magnetic body is reduced to a critical limit, then the domain wall formation is not



**Figure 1.4:** (a) Schematic of varying intrinsic coercivity of a magnetic particle with its diameter. Adapted from Ref. 44. (b) A superparamagnetic particle has an energy barrier to its magnetic reversal in an applied magnetic field. Adapted from Ref. 40.

energetically favorable. In effect, the magnetic particle possesses a single domain state and its coercivity is maximum for the particle size  $D_s$ , as shown in Fig. 1.4 a.

Unlike the domain wall motion in a multi-domain state, the particle with the size  $\leq D_s$  changes its single domain magnetic state by spin rotation. The coercivity of a particle decreases by decreasing its diameter because of thermal fluctuations. For the particle size below a critical limit  $D_p$ , thermal fluctuations are strong enough to overcome the anisotropy forces and thus the particle does not have a fixed direction of its magnetic moment. This superparamagnetic response is shown in Fig. 1.4 a for the particle size below  $D_p$  showing zero intrinsic coercivity. The single domain particle has a constant magnetic moment, provided by its anisotropy energy.<sup>40,44</sup>

$$E_a = K_1 \sin^2 \theta \quad (1.8)$$

where  $E_a$  and  $K_u$  are uniaxial anisotropy energy and anisotropy constant and  $\theta$  is the angle between the magnetization direction and easy axis. For the particle size below  $D_p$ , the continuous thermal fluctuations happening on the microscopic scale dominate the energy barrier  $\Delta E = KV$ . However, for an increased Zeeman energy  $\Delta E$  becomes asymmetric, as shown in Fig. 1.4 b, where  $\theta$  is the angle between the magnetic moment and the anisotropy axis. The origin of the energy barrier  $\Delta E$  can be magnetocrystalline anisotropy, shape anisotropy or surface anisotropy.<sup>40</sup>

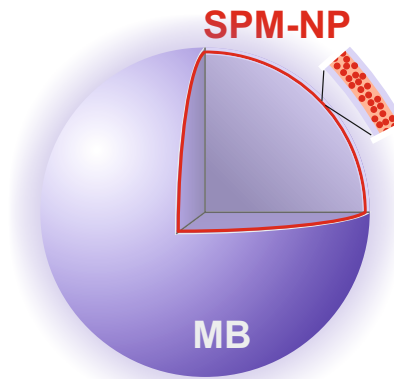
The time required by the magnetization to reverse its direction is determined by relaxation time which is a ratio of  $KV$  and thermal fluctuation  $k_B T$  through the following expression.<sup>44</sup>

$$\tau = \tau_0 \exp \left( \frac{KV}{k_B T} \right) \quad (1.9)$$

$\tau_0$  is the attempt frequency, a constant with the value between  $10^{-13} - 10^{-9}$  seconds. If the relaxation time of magnetization is faster than the measurement time ( $\tau \gg \tau_m$ ) then the magnetization will flip its orientation numerous times and averages to zero, provided that the particle size is within the superparamagnetic SPM limit. If  $\tau \ll \tau_m$ , then the magnetization will not flip during the measurement and its static orientation represents a blocked state. The blocking temperature  $T_b$  is the mid-point between two states, when  $\tau = \tau_m$ . Thus, both the temperature and measurement time determine the SPM response of a particle.<sup>45</sup> Moreover, the particle must behave like a paramagnet at  $T_b < T < T_c$ . Unlike ferromagnets, becoming paramagnetic above the Curie temperature, SPM particles only appear as paramagnetic below  $T_c$ , but with a giant magnetic moment. The magnetic moment per atom of a conventional paramagnetic material is a few Bohr magnetons, whereas a spherical iron particle with 5 nm diameter, containing 5560 atoms has a moment of  $5560 \times 2.5 = 12,000 \mu_B$ .<sup>40</sup> Due to almost zero magnetic coercivity and the superparamagnetic response, nanometer sized magnetic particles are utilized for the fabrication of superparamagnetic microbeads. The critical size of a particle for the SPM response is material dependent and is around a few tens of nanometers.<sup>44</sup>

### 1.2.4 Microbeads

Commercially available SPM-MBs are polymeric (typically polystyrene) sphere containing  $\text{Fe}_2\text{O}_3$  and  $\text{Fe}_3\text{O}_4$  nanoparticles dispersed in various geometries such as single core, multi-core, thoroughly dispersed in the polymeric sphere or at its periphery.



**Figure 1.5:** Schematic of a micromer<sup>®</sup>-M microbead doped with the superparamagnetic nanoparticles SPM-MP at the MB's outer shell.<sup>46</sup> Reproduced from Ref. 42 with permission © 2017 IOP Publishing.

Purchased from micromod Partikeltechnologie GmbH, micromer<sup>®</sup>-M MBs with 2-12  $\mu\text{m}$  diameter were employed in this research work. Chemically functionalized with PEG-COOH the aqueous micromer<sup>®</sup>-M medium contains  $1.2 \times 10^{10}$  to  $5.1 \times 10^7$  particles per ml for the 2  $\mu\text{m}$  and 12  $\mu\text{m}$ .<sup>46</sup> To observe the motion of single particles, a highly diluted suspension is prepared in distilled water ( $\approx 0.1 - 0.5\%$  of the original concentration). To avoid the nonspecific adhesion of MBs to the chip surface,  $\approx 0.1 - 0.3\%$  Triton X-100 was added to the aqueous suspension.

In response to an applied magnetic field, Micromer<sup>®</sup>-M MBs show fast magnetic attraction due to magnetic nanoparticles as sketched in Fig. 1.5. With almost no magnetic remanence or coercivity at room temperature, MBs were observed singular in the absence of applied magnetic field during the experiments. Since, the literature<sup>27-31</sup> reports on the heterogeneous magnetic properties of all commercially available MBs due to the technological limitation, this experimental research was focused on one type of MBs, i.e. micromer<sup>®</sup>-M. The MB size dependent magnetic characteristics are presented in Sec. 3.2.

### 1.2.5 Forces on a Microbead

Using the Basset-Boussinesq-Oseen equation for vanishing fluid velocity and negligible forces terms, the simple form of force balance results in:<sup>42</sup>

$$m_{\text{eff}} \cdot \frac{d^2 \mathbf{x}}{dt^2} = -\Gamma_{\text{hd}} \frac{d\mathbf{x}}{dt} + (-\nabla U) \quad (1.10)$$

The mass term, on the left side, is generally ignored because the inertial forces are dominated by the viscous damping in microfluids. This term relates to the time required for a bead to reach its terminal velocity ( $\mu s$ ) which is far from the timescale of interest ( $ms$ ). Now, the force balance of a moving bead is given by the hydrodynamic drag force and the magnetic force provided by the magnetic potential gradient (two terms on the right side of eq. 1.10).

$$\gamma \cdot \Gamma_{\text{hd}} \frac{d\mathbf{x}}{dt} = -\nabla U \quad \rightarrow \quad \gamma \cdot (6\pi\eta r_{\text{MB}}) \frac{d\mathbf{x}}{dt} = -\nabla U \quad (1.11)$$

On the left side, the linear hydrodynamic damping parameter  $\Gamma_{\text{hd}}$  includes the radius of a microbead  $r_{\text{MB}}$  and the viscosity of the aqueous medium  $\eta$ . The dynamic viscosity of  $\text{H}_2\text{O}$  is  $\eta \approx 0.0009 \text{ Pa}\cdot\text{s}$  at a temperature  $T = 25^\circ\text{C}$ .  $\frac{d\mathbf{x}}{dt}$  is the velocity of a moving MB and  $\gamma$  represents a correction factor considering the sliding motion of a particle near a wall (magnetic surface).<sup>29,47</sup> The friction force can be calculated by subtracting the viscous from the tangential component of the magnetic force for the bead motion at a phase locked angle.<sup>29</sup> Considering the physical properties such as size and density of the bead, nonmagnetic vertical forces such as buoyancy and gravitational can be ignored due to their far lower magnitudes.<sup>29</sup> The magnetic potential gradient  $-\nabla U$  is defined next.

### Magnetic Force on Microbead

The magnetic force on a magnetic dipole in the presence of a non-uniform magnetic field is given by:<sup>48,49</sup>

$$\vec{F}_{\text{mag}} = \int_V \nabla(\vec{m} \cdot \vec{B}) dV \quad (1.12)$$

Since there are no conduction currents in our manipulation system, a vector identity is used to rewrite the eq. 1.12 as follows:

$$\nabla(\vec{m} \cdot \vec{B}) = \vec{m} \times (\nabla \times \vec{B}) + \vec{B} \times (\nabla \times \vec{m}) + (\vec{B} \cdot \nabla)\vec{m} + (\vec{m} \cdot \nabla)\vec{B} \quad (1.13)$$

The 1<sup>st</sup> term on the right hand side vanishes as divergence of B is zero because no conduction currents or time varying electric field is present.<sup>44</sup> Assuming the magnetization of the bead constant, the 2<sup>nd</sup> and 3<sup>rd</sup> terms also vanish. The 4th term (last term on right hand side in eq.1.13) results in non-zero gradient of the applied field vector, which leads to an approximation of eq. 1.12:<sup>48,49</sup>

$$\vec{F}_{mag} = \int_V (\vec{m} \cdot \nabla)\vec{B} dV \quad (1.14)$$

Note that this expression holds true, if the magnetic moment of bead is not varying in space. The definition  $(\vec{m} \cdot \nabla) = m_x \frac{\partial}{\partial x}$  says that a bead with a constant magnetic moment experiences a force in x-direction, if there is a magnetic field gradient present. The quantity  $(\vec{m} \cdot \nabla)\vec{B}$  becomes a complicated function of the spatial coordinates, if the spatial dependence of both the magnetic field and magnetic moment is considered.<sup>48</sup> Thus, the effective magnetic moment for a homogeneous bead is approximated as:  $\vec{m}_{eff} = V\vec{M}$ , where  $V$  and  $\vec{M}$  are the volume and volume magnetization of the bead.

For an approximated linear volume magnetization of a magnetic bead, the relation  $\vec{M} = \chi_i \vec{H}_i$  can be used where  $\chi_i$  is the intrinsic susceptibility and  $\vec{H}_i$  is the local field inside the material. However, practically the susceptibility is measured under an applied magnetic field. With the consideration of the demagnetization field inside the bead ( $\vec{H}_i = \vec{H} - \vec{H}_{demag}$ ) for a spherical geometry  $\vec{H}_{demag} = N\vec{M} = \frac{\vec{M}}{3}$ , the volume magnetization of a bead is given as<sup>44</sup>

$$\vec{M} = \left(\frac{3\chi_i}{3 + \chi_i}\right)\vec{H} = \chi_{eff}\vec{H} \quad (1.15)$$

Now, the magnetic moment of the MB can be described in the form of its effective volume susceptibility under an applied magnetic field as:  $\vec{m}_{eff} = V\chi_{eff}\vec{H}$ . Using the relation  $\vec{B} = \mu_0\vec{H}$ , magnetic force eq. 1.14 can be written as:<sup>44</sup>

$$\vec{F}_{mag} = \frac{\chi_{eff}V}{\mu_0}(\vec{B} \cdot \nabla)\vec{B} \quad (1.16)$$

Using a vector identity  $\nabla(\vec{B} \cdot \vec{B}) = 2(\vec{B} \times \nabla)\vec{B} + 2\vec{B} \times (\nabla \cdot \vec{B})$ , where curl terms of the magnetic field vector vanish due to no electric currents in the system, eq. 1.16 is simplified as<sup>44,48,49</sup>

$$\vec{F}_{mag} = \frac{\chi_{eff}V}{2\mu_0}(\vec{B} \cdot \nabla)\vec{B} \quad (1.17)$$

The term  $\frac{1}{2\mu_0}(\vec{B} \cdot \vec{B}) = \frac{1}{2}(\vec{H} \cdot \vec{B}) = \frac{\mu_0}{2}(\vec{H} \cdot \vec{H}) = \frac{\mu_0}{2}|\vec{H}|^2$  is the magnetic field energy density. Magnetic force on the bead now takes the form:<sup>48</sup>

$$\vec{F}_{mag} = \frac{\mu_0\chi_{eff}V}{2}\nabla|\vec{H}|^2 \quad (1.18)$$

From this equation, it is understandable that a magnetic particle will follow the steepest gradient of magnetic field squared. For the static field condition and the approximated constant volume susceptibility of the bead  $\chi_{eff}$ , the magnetic potential energy is  $\vec{F}_{mag} = -\nabla U$ .

Equalizing eq. 1.11 and 1.18 leads to an expression for a balance between the magnetic force and hydrodynamic drag force (both in pN range) . This force balance defines the maximum achievable velocity of a moving MB provided by the magnetic field gradient in a flowless aqueous medium. The MB velocity  $\frac{dx}{dt}$  can be written as a balance term  $\zeta$ <sup>49</sup>

$$\zeta = \frac{\mu_0\chi_{eff}\nabla|\vec{H}|^2V}{\gamma \cdot 6\pi\eta r_{MB}} = \frac{2\mu_0\chi_{eff}\nabla|\vec{H}|^2r_{MB}^2}{\gamma \cdot 9\eta} \quad (1.19)$$

The balance term  $\zeta$  is also called as magnetophoretic mobility MPM.<sup>49</sup> For the linear motion of a MB, the magnetic term (numerator in eq. 1.19) must dominate, i.e.  $\zeta > 1$ .  $\zeta < 1$  describes that the MB velocity has crossed a critical limit, where the viscous force term (denominator in eq. 1.19) overcomes the magnetic force and consequently MB undergoes a nonlinear motion. Practically, the magnetophoretic mobility term  $\zeta$  is determined as the critical frequency  $f_{crit}$  of a bead during its motion on magnetic structures along the moving  $H_{ext}$ .

## Discussion and Summary

The magnetic force acting on a bead (approximated to a constant  $\chi_v$ ) is proportional to the applied field strength and the resultant field gradient. However, depending on the geometric and magnetic character of the bead moving structure the effective magnetic force on the bead may greatly vary. The magnetic force on a moving MB is a function of MB-volume, while the opposing hydrodynamic viscous force is a function of MB-radius, as indicated in eq. 1.19 for the achievable MPM of MB. Determining the  $f_{crit}$  for different types of MBs on a simple circular MS provides the basic knowledge about the MBs motion. This helps to employ the manipulation strategies such as altering the geometric properties of magnetic structures and choosing the appropriate sequence of  $H_{ext}$  for the separation of MBs.



# Chapter 2

## Numerical and Experimental Methods

### 2.1 Micromagnetic Calculations

In micromagnetics, the local magnetization vector  $M$  changing its direction (x, y, z) inside a ferromagnetic structure provides information about the magnetic domain state, resulting from the competing contributions of exchange energy, demagnetizing energy, anisotropy energy and Zeeman energy present in the system.<sup>40</sup> Micromagus<sup>®</sup> software<sup>50</sup> was employed to quasi-statically simulate the equilibrium domain state of NiFe micromagnets.

Assuming a homogeneous magnetization inside a discretization cell, the summation over the cells for the volume  $\Delta V$  is performed by an FFT algorithm to calculate the stray field energy.<sup>51</sup> In order to speed up the simulation time, calculations were done on structures scaled down by a factor 2. A cell size of  $24.4 \text{ nm} \times 25.4 \text{ nm} \times 8.33$  was used for the calculations on NiFe magnetic structures with a thickness of 30 nm and 50 nm. A saturation magnetization of  $M_s = 800 \text{ kA/m}$  and stiffness constant  $A = 1.3 \times 10^{-11} \text{ J/m}$  was used in the simulation.<sup>42</sup> Magnetocrystalline and uniaxial anisotropies were neglected.

#### 2.1.1 Magnetization and Stray Magnetic Field

In the absence of an external magnetic field, the magnetic domain state of a magnetic pattern is defined by its shape. The magnetization is forced to be in the film plane for thin film magnetic patterns. Initially defined by the pattern geometry, the magnetization at the edges of a soft ferromagnet can be tuned precisely with the changing amplitude of an in-plane external magnetic field  $H_{ext}$ . The isotropic (disk) and anisotropic (triangle) shapes of thin film magnetic structures are employed as model systems in this thesis for the manipulation of locally inhomogeneous magnetizations. Since the demagnetizing field ( $H_d$ ) is present in the magnetic structure (see eq. 1.6),  $H_d$

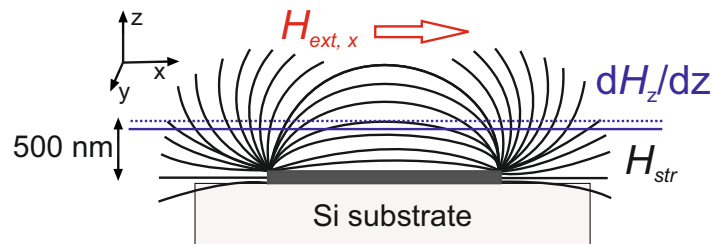


tends to reduce the net magnetic moment of the structure by a continuous rotation.<sup>44</sup> For an externally applied magnetic field  $H_{ext}$ , the laterally varying magnetizations in the magnetic pattern are given by the competition between the amplitude of  $H_{ext}$  (aligning  $M$  along  $H_{ext}$ ) and the demagnetization fields (aligning  $M$  along the boundary of the pattern). As a result,  $M$  is homogeneously aligned along  $H_{ext}$  in the middle region of the MS, while it has inhomogeneous orientation at the edges. This leads to a locally constrained stray magnetic field and the field gradient around the pattern, which can be manipulated to move the magnetic particles. The soft magnetic material such as Permalloy is a suitable choice to manipulate the magnetization domain states and through that, the stray field gradients at the boundary of magnetic patterns.

### 2.1.2 Absolute Stray Field Gradient in z-direction

For in-plane applied magnetic fields, the stray field components ( $H_{str,x}$ ,  $H_{str,y}$  and  $H_{str,z}$ ) are calculated at a height of 500 nm above the magnetic surface. The dotted lines in Fig. 2.1 indicate two other heights, equaling  $1.5\times$  size of the discretization cell from the reference height of 500 nm (see Sec. 2.1). With the numerical differentiation of stray field amplitudes at corresponding heights above the surface, the out-of-plane component of stray field gradient ( $dH_z/dz$ ) is calculated.

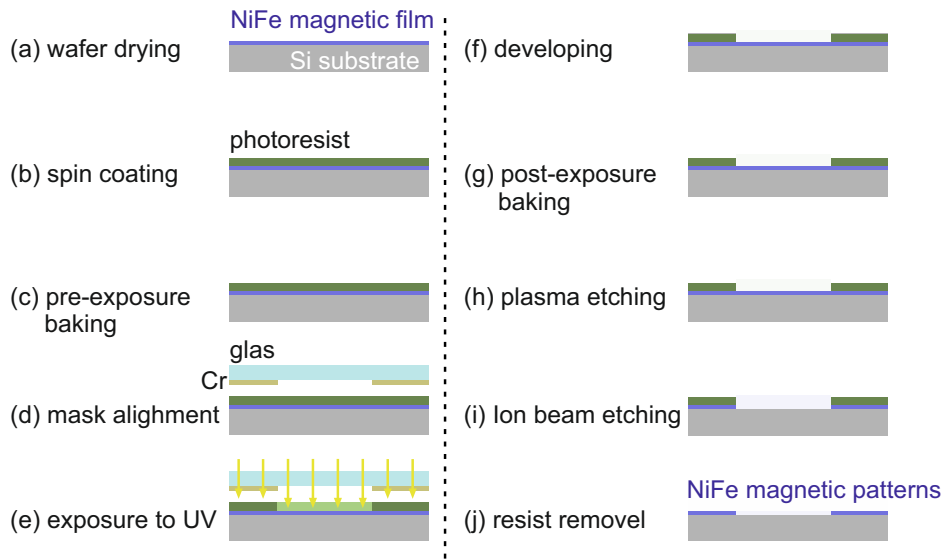
Due to the magnetic film thickness being within the range of Néel wall (in-plane), the larger effect of inhomogeneous  $M$  is determined for the out-of-plane component of stray magnetic field ( $H_{str,z}$ ). The simulation results on exemplary magnetic patterns with 30 nm and 50 nm thickness revealed that the value of magnetic field gradient (FG) in z-direction is very near to the total FG ( $dH_z/dz \approx 0.9 \times \nabla \cdot H_{eff}$ ). Therefore, depending on the amplitude of  $H_{ext}$ , the motion of magnetic particles is explained with the changing amplitude of  $dH_z/dz$ . This phenomenological approach was adapted for most of the research presented here. The signs of FG are omitted to emphasize the magnitude of  $dH_z/dz$  on the magnetic patterns, thus  $|\frac{dH_z}{dz}|$ . At the same height on the magnetic chip and same  $H_{ext}$  conditions, the corresponding stray fields are experimentally determined with magnetic force microscopy MFM. Note that the MFM maps reflect primarily the z-component of the stray field gradient acting on the magnetic tip (see Sec. 2.3.2).



**Figure 2.1:** Schematic of the stray fields  $H_{str}$  above a magnetic pattern. The field gradient ( $dH_z/dz$ ) is calculated from the numerical differentiation of  $H_{str}$ .

## 2.2 Fabrication of Magnetic Structures

Soft magnetic full films were prepared by sputter deposition on 4 inch diameter wafers at the IPHT Jena. The layer system Ta/Ni<sub>81</sub>Fe<sub>19</sub>/TaN was deposited on an oxidized Si substrate Si (500  $\mu\text{m}$ )/SiO<sub>2</sub>(1  $\mu\text{m}$ ). Magnetic films with two different thicknesses 30 nm and 50 nm were chosen for the formation of magnetic structures MSs. The seed layer of Ta (3 nm) and covering layer of TaN (5 nm) protect the MSs against oxidation and corrosion from the suspension of magnetic particles. Using the photo mask the patterning of micron sized MSs with various sizes and geometries was done with standard photolithography. Fig. 2.2 shows the sequence of the fabrication processes.



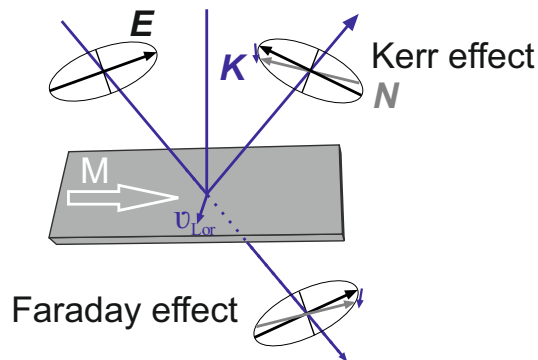
**Figure 2.2:** (a)-(j) Photolithography process for a positive photoresist

First of all, the wafers were dried at 120°C for 1 hour to remove moisture, if present. Before the spin coating, an adhesion promoter HMDS-100 was applied for better adhesion of the photo-resist to the wafer. The wafer was coated with photoresist AZ 4060 at a high spinning speed of 8000 rpm for 30 seconds. After a pre-exposure bake for 100 s at 100°C the wafer was placed under the pre-placed mask in the mask aligner and was exposed to UV light in a vacuum contact mode. Determined by the UV power measurements, the wafer was exposed for  $\approx 1$  s. The developing was performed in a AR 300-47 developer and distilled water (1:2) solution for 30 s. After the microscopic examination of the patterned MSs, the wafer was hard baked for 2 minutes at 110°C. Plasma etching helped in removing the resist along the edges of the thin film MSs. The uncovered magnetic film was removed with selective ion beam etching. The wafer with structures was diced to 10 mm  $\times$  10 mm chips. To remove the resist covering the magnetic patterns, single chips were treated in a hot ultrasonic bath (60°C) with a NMP (N-Methyl-2-pyrrolidone) prepared solution. Ferromagnetic structures from a 50 nm thin film of Fe<sub>70.2</sub>Co<sub>7.8</sub>Si<sub>12</sub>B<sub>10</sub> with a seed layer and protective coating of Ta (6 nm) were patterned with the same photolithography processes described above.

## 2.3 Experimental Methods

### 2.3.1 Magneto-optical Kerr Effect Microscopy

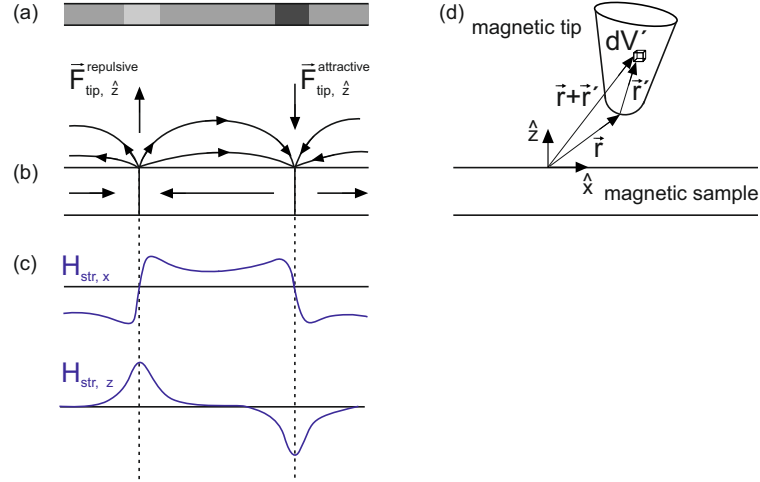
Magneto-optical Kerr effect microscopy is utilized to investigate the magnetic properties of materials through magnetic domain observation. Its working principle consists of measuring the rotation in the polarization axis of incident light after its reflection from a magnetic sample. This measured change in the polarization angle of the reflected light, representing the sample magnetization, is employed for the domain imaging of the magnetic sample. The magneto-optical effect originates from the exchange energy splitting together with the spin orbital coupling.<sup>52</sup> The interaction between the polarized electromagnetic light wave and the material magnetization is analogous to a Lorentz force on moving electrons by the electrical vector  $E$  of the wave.<sup>53</sup> After the incident and reflected light respectively passing through the polarizer and analyzer, the resultant change in the polarization named as Kerr effect, leads to a magnetic contribution (Kerr amplitude,  $K$ ) to the reflected light amplitude  $N$ .<sup>53</sup> The perpendicular polarization of  $K$  relative to the normally reflected light  $N$  and through its interference with  $N$  results in the rotation of the polarization of light. The longitudinal Kerr effect occurs when magnetization lies parallel to the plane of the incident light.<sup>53</sup> Using the longitudinal Kerr effect, the changing magnetization of NiFe patterns with different amplitudes of  $H_{ext}$  is determined. At the threshold applied  $H_{ext}$ , the saturated magnetic domain state of the magnetic elements is revealed. For equal  $H_{ext}$ , stray field gradients are determined by MFM imaging and micromagnetic calculations and the controlled movement of MBs is achieved.



**Figure 2.3:** Schematic of magneto-optical Kerr effect MOKE for the longitudinal configuration. Adapted from Ref. 53

### 2.3.2 Magnetic Force Microscopy Imaging

Based on the working principle of atomic force microscopy, magnetic force microscopy MFM relies on the deflection of a cantilever tip coated with ferromagnetic material. When scanned over a magnetic surface, a magnetic contrast (Fig. 2.4 a) is obtained through the attractive and repulsive forces (Fig. 2.4 b) experienced by the tip after its interaction with stray magnetic fields on the sample.



**Figure 2.4:** (a) Magnetic contrast formed on scanning over a longitudinal recording media (b). (c) Parallel and perpendicular field components determine the respective odd and even symmetry over the transition regions of head-to-head and tail-to-tail domains. (d) Geometry of magnetic tip for the calculation of force derivative. (Reproduced with permission from Ref. 54 © 1990 American Institute of Physics.)

The force acting on a volume element  $dV'$  at an internal coordinate  $r'$  of tip as shown in Fig. 2.4 d is given by:<sup>54 55</sup>

$$d\vec{F}'_{tip} = \mu_0 \nabla [\vec{M}_t(\vec{r}') \cdot \vec{H}_{str}(\vec{r} + \vec{r}')] dV' \quad (2.1)$$

where  $\vec{M}_t(\vec{r}')$  is the magnetization of the tip and  $\vec{H}_{str}(\vec{r} + \vec{r}')$  is the stray magnetic field on the sample. When the force component normal to the cantilever is  $d\vec{F}'_{tip} = \hat{n} \cdot d\vec{F}'_{tip}$  then the force gradient is given as:

$$d\vec{F}'_{tip, \hat{n}} = \mu_0 \hat{n} \cdot \nabla \{ \mu_0 \nabla [\vec{M}_t(\vec{r}') \cdot \vec{H}_{str}(\vec{r} + \vec{r}')] \} dV' \quad (2.2)$$

If the tip is approximated to a magnetic point dipole  $m$  and the cantilever is parallel to the sample surface, then  $\hat{n} = \hat{z}$  and the force gradient simplifies to:

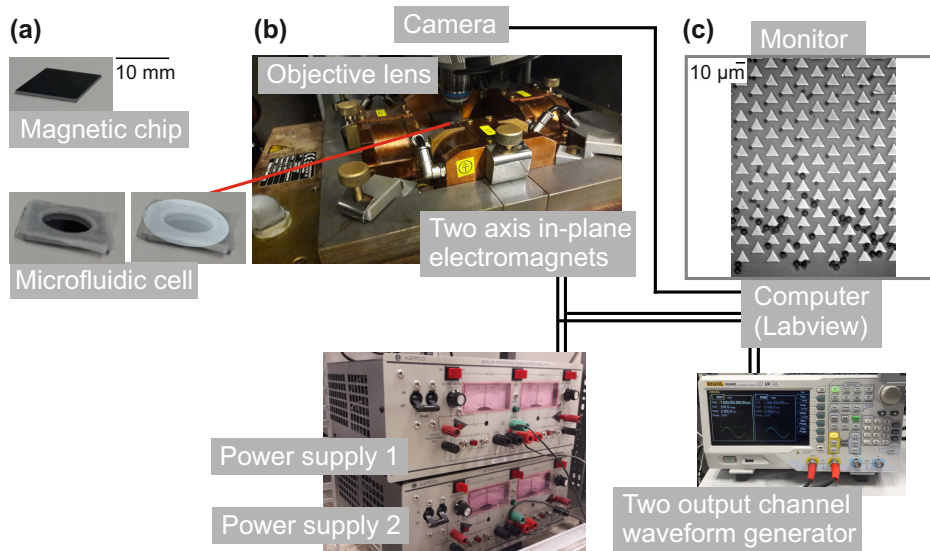
$$\vec{F}'_{tip, \hat{z}} = \mu_0 \left( m_{t,x} \frac{\partial^2 \mathbf{H}_{str,x}}{\partial z^2} + m_{t,y} \frac{\partial^2 \mathbf{H}_{str,y}}{\partial z^2} + m_{t,z} \frac{\partial^2 \mathbf{H}_{str,z}}{\partial z^2} \right) \quad (2.3)$$

where  $m_{t,x}$ ,  $m_{t,y}$  and  $m_{t,z}$  are magnetic moments components of the tip interacting with the dipolar stray fields at a certain height on the whole sample. Considering only the vertical magnetization component of the tip ( $m_x$  and  $m_y = 0$ ) the equation reduces for z-component,  $\vec{F}'_{tip, \hat{z}} = \mu_0 \left( m_{t,z} \frac{\partial^2 \mathbf{H}_{str,z}}{\partial z^2} \right)$ . Also in practice, vertical alignment of the tip magnetic moment is performed by initialization of the tip with a permanent magnet along the z-direction before the measurements.

First a scan in AFM mode is performed on sample surface to obtain topographical details resulting from van der Waals and magnetic forces with a hard magnetic tip. To map the stray field distributions a second scan (lift mode) is done at a constant height, which was determined by attaining highest possible magnitude of magnetic signal whilst avoiding generation of surface induced artifacts. The 30 and 50 nm thick  $\text{Ni}_{81}\text{Fe}_{19}$  and  $\text{Fe}_{70.2}\text{Co}_{7.8}\text{Si}_{12}\text{B}_{10}$  patterns were scanned at a height of 500 nm above the surface under varying in-plane external magnetic fields. A customized field setup is capable of applying  $H_{ext}$  in range of 2-24 kA/m, equal to the field range used for the MB manipulation. In the employed dynamic MFM imaging mode, the cantilever oscillates with a resonance frequency of 65-70 kHz.<sup>56</sup> On the interaction with the stray fields from the sample, a resultant force and thus a shift in the resonance frequency occurs. This phase difference is an indirect measure of the stray fields on the magnetic patterns. All the MFM maps shown in coming chapters were performed with the phase contrast mode.<sup>56</sup>

### 2.3.3 Experimental Setup

The microfluidic cells with cylindrical wells ( $d = 7 \mu\text{m}$ ,  $h = 500 \mu\text{m}$ ) were prepared on  $10 \text{ mm} \times 10 \text{ mm}$  magnetic chips. The cohesive nature of the plastic paraffin film (Parafilm M) enables its bonding with the chip surface. After pouring the microbeads suspension, the cell covered with glass slip is fixed on sample holder. Two-axis in-plane electromagnets can generate  $H_{ext}$  up to 80 kA/m with selectable field sequences. MBs' motion was recorded with a frame rate of 16 frames/s. The movement path of magnetic MB is tracked by determining its spatial position on the chip surface, with a manual tracking tool in the ImageJ image processing software.<sup>57</sup>



**Figure 2.5:** Measurement setup for the microbead manipulation. (a) Magnetic chip with a microfluidic cell and cover glass. (b) Electromagnets create  $H_x$  and  $H_y$  magnetic fields in the chip plane (c) Computer-controlled magnetic field sequences enable the bead motion.

# Chapter 3

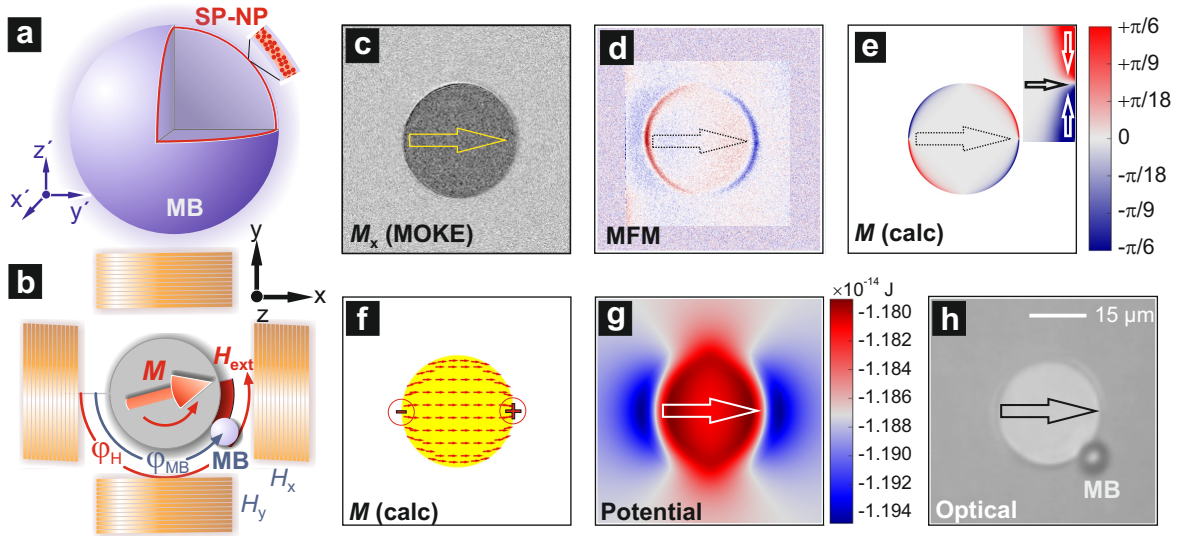
## Microbead Motion on Single Magnetic Structures

### 3.1 Magnetomechanics of a Microbead

The controlled motion of single superparamagnetic-microbeads SPM-MBs on thin film soft magnetic structures MSs make MBs useful for the handling of biological entities. A disk shaped MS is advantageous, to understand the linear and non-linear motion dynamics of a MB, using a homogeneously rotating external magnetic field  $H_{ext}$ . Experiments demonstrate the continuous and looping motion of a MB, coupled with the micromagnetic state at the perimeter of a disk. To quantitatively reproduce the features of MB motion via a numerical model, the exact micromagnetic configuration of the bead carrying structure and the approximate position of iron oxide nanoparticles inside the MB is taken into consideration. An excellent agreement between the simulations and the experiments is established. This ab initio modelling approach is also able to predict the behavior of SPM-MBs on arbitrary magnetic patterns and field excitations.

#### 3.1.1 Circular Pattern as a Model Structure

To examine the motion dynamics of a MB on the surface of a microfluidic chip, we chose an  $8\ \mu\text{m}$  MB *micromer*<sup>®</sup>-M and a 30 nm thin NiFe disk pattern with a diameter of  $30\ \mu\text{m}$  as the parent MS. A single MB with superparamagnetic nanoparticles embedded at the shell is sketched in Fig. 3.1 a. The experimental system sketched in Fig. 3.1 b shows the circulation of the MB around the MS. On applying an external magnetic field of 16 kA/m, a static magnetic state of NiFe disk with a constant lateral magnetization distribution is determined using MOKE imaging, as shown in Fig. 3.1 c. MFM measurements (Fig. 3.1 d) performed at a height of 400 nm above the surface of NiFe disk reveal a spatial distribution of magnetic stray fields at the disk perimeter in the field direction. MM simulations determine the magnetization distributions at



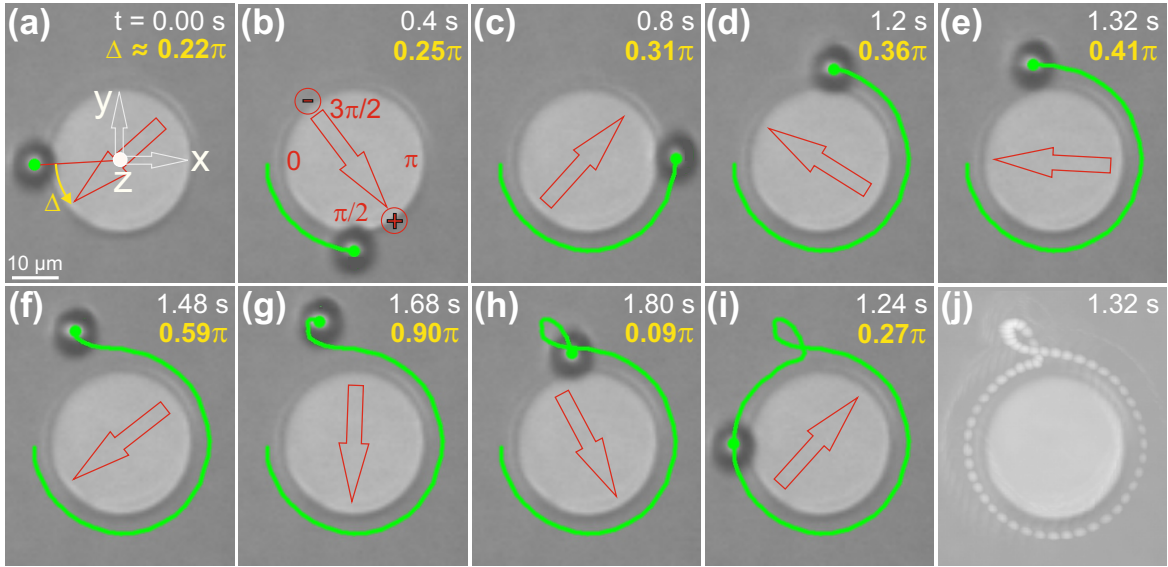
**Figure 3.1:** Schematic of a microbead embedded with superparamagnetic nanoparticles, (b) Sketch of the experimental system depicting the rotation of MB around a disk under the rotating  $H_{ext}$ . (c) Magneto-optical Kerr effect (MOKE) image showing the magnetization component  $M_x$  on a 30 nm thick NiFe disk. (d) Magnetic force microscopy (MFM) phase contrast image revealing the strongly polarized edges of the disk in the  $H_{ext}$  direction. (e) Magnetization angle determined using micromagnetic (MM) simulation. (f) Magnetization vectors distribution under the same field conditions as (c) and (d). (g) Potential energy distribution achieved on integrating the stray field of the NiFe disk over the magnetic volume of  $8 \mu\text{m}$  MB. (h) Optical image of the model system showing the moving bead following the  $H_{ext}$  rotation. Reproduced from Ref. 42 with permission © 2017 IOP Publishing.

the opposite edges as an onion domain state with a transverse-like domain wall structure (Fig. 3.1 e and f). A static configuration of magnetic potential energy in Fig. 3.1 g is calculated by integrating the numerical stray field distributions over the effective magnetic volume of an  $8 \mu\text{m}$  MB. An optical image of the magnetostatically coupled MB with the micromagnetic feature of the disk is shown Fig. 3.1 h, showing its spatial position during the circulating motion. The MB is lagging behind the rotating  $H_{ext}$ .

### 3.1.2 Microbead Looping

After the confinement of a magnetic MB at the stray magnetic field gradient of the disk, it can be moved clockwise or counterclockwise manner with the corresponding rotation of  $H_{ext}$ . For a continuous motion of the MB in a microfluidic environment, the magnetic force, which is a result of magnetostatic coupling of the MB with the onion domain state of the disk, must be high enough to overcome the hydrodynamic drag force. The MB follows the rotating micromagnetic feature of the disk with an angular lag  $\Delta$ . This natural phase lag of the moving MB is directly related to its velocity. Thus, an increased phase lag occurs, when the applied magnetic field is rotated faster. Meanwhile, the hydrodynamic drag force dominates the magnetic coupling strength of the particle momentarily and with the accompanying reduced field gradient and phase

lagged position they cause the detachment of particle from the disk.



**Figure 3.2:** (a)-(d) Exemplary motion of a MB following the ccw-rotating  $H_{ext}$ , with a continuously increasing phase lag  $\Delta$  between the angular positions of the bead and magnetic field. (e) The bead starts moving away from disk perimeter at a larger phase lag close to  $90^\circ$ . (f)-(h) Looping and reapprach of the bead towards the opposite magnetic potential. (i) Continuation of regular motion with a lower  $\Delta$  as in (a). (j) Record of the MB motion. Diameters of the bead and disk are  $8 \mu\text{m}$  and  $30 \mu\text{m}$ .  $H_{ext}$  has a strength of  $16 \text{ kA/m}$  and a rotational frequency  $f_{rot} 0.6 \text{ Hz}$ . Rotating net magnetization  $M$  of NiFe disk with the sign of magnetic charges as indicated by arrows.  $\Delta$  represents the lagged position of MB relative to the angular position of the axis of  $H_{ext}$ , i.e. head of  $M$  in (a)-(g) and tail of  $M$  in (h)-(i). Reproduced from Ref. 42 with permission © 2017 IOP Publishing.

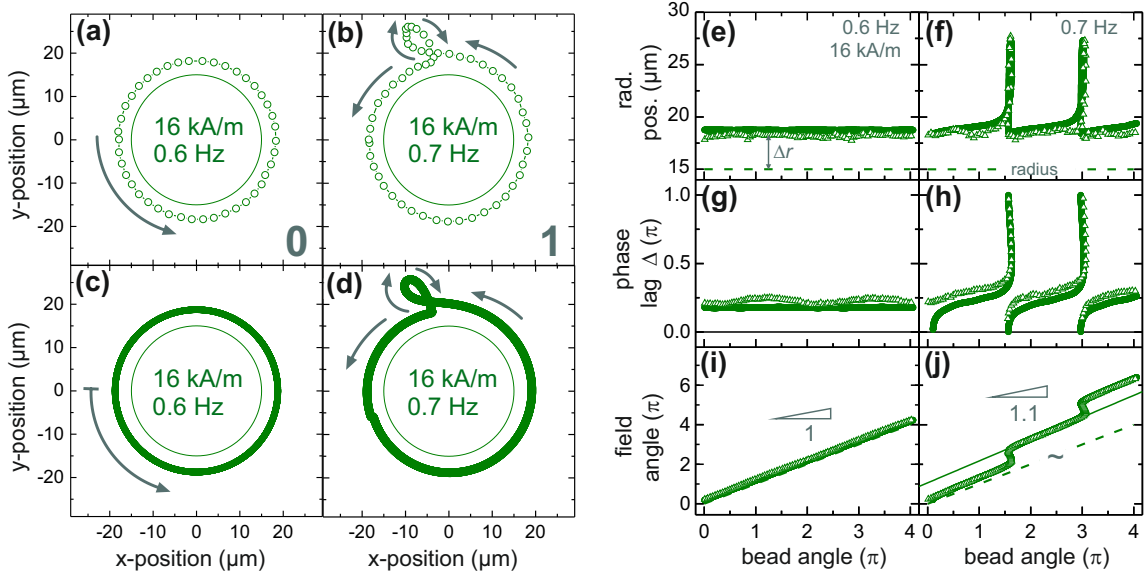
An illustration of such a nonlinear motion is displayed in Fig. 3.2. A MB is moved with a fixed rotational frequency  $f_{rot} = 0.7 \text{ Hz}$  and an amplitude of  $H_{ext} = 16 \text{ kA/m}$ . Initially, it follows the field with a continuously increasing phase lag ( $\Delta$ ), as shown in the experimentally captured events in Fig. 3.2 a-c. Meanwhile, the increased hydrodynamic damping causes the bead to deviate from the magnetic potential minima, where an increased difference in the angular positions of bead and rotating field occurs (Fig. 3.2 d-e). At a larger phase lag  $\Delta = \pi/4$ , the bead detaches from the disk (Fig. 3.2 f), drastically slows down (Fig. 3.2 g), loops and is ultimately recaptured by the oppositely sided magnetic potential (Fig. 3.2 h). After the looping, it moves continuous again with a small  $\Delta$ , as shown in Fig. 3.2 i just as in Fig. 3.2 a. A full track of the motion is revealed in Fig. 3.2 j, in which 1.5 revolution of  $H_{ext}$  produces 1 revolution of the bead, including one looping.

### 3.1.3 Numerical Modelling of Microbead Motion

To numerically model the experimentally observed MB motion, the complex spatial and time dependencies of the motion system were determined with discrete Fourier



expansion. To calculate the local potential energy distribution from the MB center-of-mass and time, a polynomial expansion was employed. Fitting the algorithms together provides the information for the reproduction of the MB's experimental response. The detail is given in our published work Ref. 42. This numerical model replicates the experimental motion in linear and nonlinear regime with high accuracy at various  $H_{ext}$ . The only adapted parameter in the modeling is the effective susceptibility of the MB. The susceptibility values of a single MB in the simulation are  $2 \pm 0.25$  of the values obtained from a M(H) curve (provided by the vendor of micromer-M) at an applied working field  $H_{ext}$  of 4, 8 and 16 kA/m.



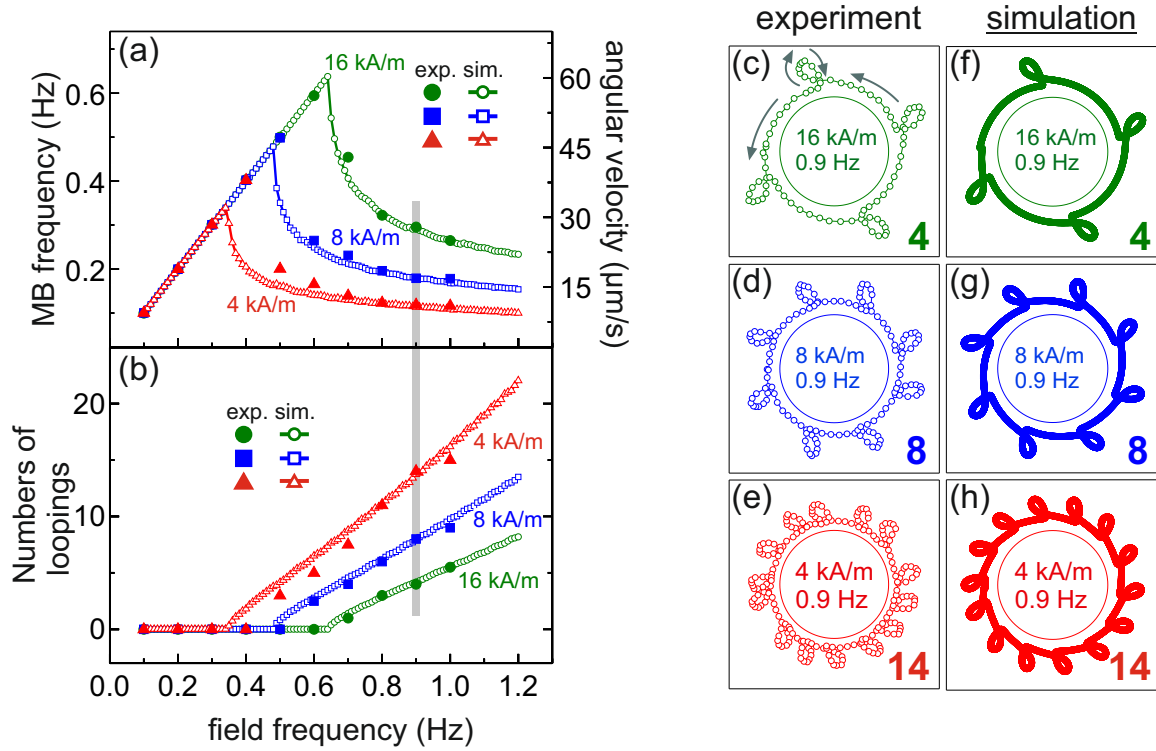
**Figure 3.3:** Experimental and simulated paths of motion for an 8  $\mu\text{m}$  diameter particle around 30  $\mu\text{m}$  diameter disk under a fixed amplitude  $H_{ext}$  with the varying field frequency  $f_{rot}$ . (a) A uniform circular motion with  $H_{ext} = 16 \text{ kA/m}$  and  $f_{rot} = 0.6 \text{ Hz}$  before the onset of critical regime of motion. (b) A slight increase in  $f_{rot}$ , resulting in a looping during the circular motion. (c)-(d) Simulated results at the corresponding field conditions. (e)-(j) Unwrapped trajectories, showing the features of lateral motion against two ccw rotations of the MB. Radial positions around the disk versus bead angle for the continuous (e) and looping motion (f). (g)-(h) Corresponding phase lags. (i)-(j) Field angle versus bead angle. Continuous and looping motion are highlighted with different slopes. Reproduced from Ref. 42 with permission © 2017 IOP Publishing.

The numerically calculated radial and azimuthal forces summed up to  $\approx 2 \text{ pN}$  and  $\approx 7 \text{ pN}$ , respectively. Both forces are responsible for the trapping and rotation of the MB around the magnetic disk. These forces are strong enough to overcome the already negligible non-magnetic forces, such as frictional, gravitational and basset force present during the MB motion at low Reynolds number.<sup>42</sup> The hydrodynamic drag force, which is velocity dependent, is the only effective force against the MB motion which causes its looping, if the field frequency  $f_{rot}$  of  $H_{ext}$  is over a critical limit.<sup>42</sup>

Experimental examples of the continuous and looping motion around a magnetic disk are presented in Fig. 3.3 a and b with the simulation results (Fig. 3.3 c and d) at

the same strength and rotational frequency  $f_{rot}$  of  $H_{ext}$ . From the unwrapped motion trajectories, which reveal the radial position, phase lag and field angle versus the bead angle in Fig. 3.3 e-j, the motion dynamics are well understood. For a lower  $f_{rot}$  of 0.6 Hz the particle continuously follows the field rotations, having its radial position with an offset of  $3 \mu m$  relative to the disk perimeter (Fig. 3.3 e). The distribution of magnetic stray fields at the disk perimeter determines the particle's radial position, which is in close agreement with the simulated results. With an increased  $f_{rot}$ , i.e. 0.7 Hz, the radial position of the particle initially increases slightly and then accelerates largely, until it comes to an angular stop, where it reverses back and reaches the disk, resulting in a path of its radial looping (Fig. 3.3 e). The radial extent and number of looping completely match on comparing simulation and experiment in Fig. 3.3 e and f. The experimentally determined phase lag is also reproduced by the simulations. A small uniaxial modulation in the phase lag (Fig. 3.3 g), which is likely due to uniaxial magnetic anisotropy of the ferromagnetic element, is not considered in the simulation. The particle moves continuous with a small lag at low  $f_{rot}$ , while a higher phase lag at the  $f_{rot}$  causes the occurrence of radial excursions. The particle detaches from the magnetic onion state at the disk perimeter and is recaptured by the following magnetic potential alternatively with a phase lag changing from 0 to  $\pi$ , as shown in Fig. 3.2 h. The continuous rotations of the bead around the disk are fully in relation with the field as determined by the bead angle versus field angle in Fig. 3.3 i. For increased  $f_{rot}$ , the bead angle  $\varphi_{MB}$  stops against rotating field  $\varphi_H$  during the radial looping. This causes an increased phase lag, which appears as an increased slope ( $\varphi_{MB}/\varphi_H > 1$ ) in-between the individual loopings, as indicated in Fig. 3.3 j. The modeled response of the MB completely describes the spatial and dynamic aspects responsible for its continuous and looping motion.

Average velocities  $v_{ave}$  of the MB circulation for its continuous and discontinuous looping motion over a parameter range are summarized in Fig. 3.4 a. Starting at low field frequencies, the MB's frequency and thus  $v_{ave}$  around the disk increases linearly until the critical frequency  $f_{crit}$  is reached. Afterwards, the excursive motion starts, resulting in a sudden decrease in the  $v_{ave}$ . With higher field frequencies, further reduction in the  $v_{ave}$  occurs due to a higher number of loopings per MB revolution. For higher amplitudes  $H_{ext}$  higher critical frequencies and higher values of  $v_{ave}$  are achieved. Simulated results are in an excellent agreement with the experimental  $v_{ave}$  and number of loopings with a slight mismatch at the regime of  $f_{crit}$ . Particularly, for the lowest amplitude  $H_{ext}$ , the experimental  $f_{crit}$  of the MB is delayed comparing to its modeled value. This discrepancy might be attributed to the variation in structure parameter and a minor uniaxial magnetic anisotropy in the magnetic disk which is not included in the simulation. The experimentally determined anisotropy field of NiFe disk patterns is max. 0.4 kA/m. An offset in the applied magnetic field might also be a reason to this discrepancy. The simulated response of the MB was fitted at a reference  $f_{rot}$  (0.9 Hz) of the  $H_{ext}$ . Fig. 3.4 c-h demonstrate the controllability of looping events with the changing amplitudes of  $H_{ext}$ . The number of looping events for the simulation and experiment match completely. See Movie 3.1-3.6 in Appendix-E.1.1



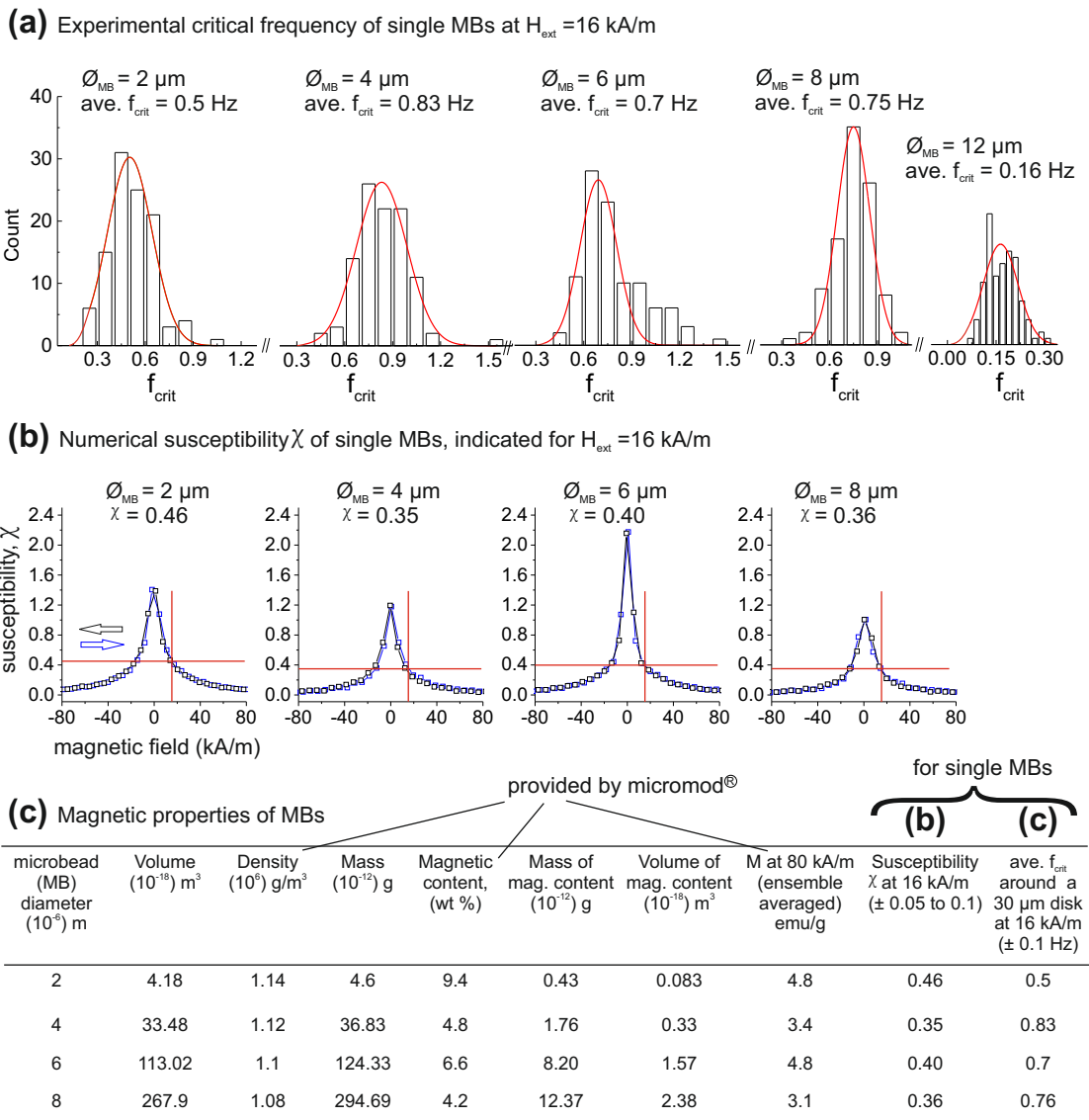
**Figure 3.4:** Overall response of an  $8\ \mu\text{m}$  bead exhibiting the control over regimes of continuous and looping motion with varying field frequency  $f_{\text{rot}}$  for three amplitudes of  $H_{\text{ext}}$ . (a) Frequencies of the MB circulation and the resulting average velocities over the rotating field frequencies  $f_{\text{rot}}$  are consistent with the looping events (b). (c)-(e) The controlled number of loopings with different amplitudes of  $H_{\text{ext}}$  at a fixed  $f_{\text{rot}}$ . (f)-(h) Reproducibility of the MB motion with simulations. Reproduced from Ref. 42 with permission © 2017 IOP Publishing.

## Summary

A simple model structure comprising of a superparamagnetic-microbead circulating around a NiFe disk describes the continuous and looping motion which are fully controllable by the rotational frequency and strength of  $H_{\text{ext}}$ . The numerical model reproduces the experimental response of the MB with a great accuracy. The features of motion such as phase lag and the extent of radial excursion provide information for the lateral motion of the MB on the periodic disk structures.

## 3.2 Characterization of Magnetic Microbeads

High throughput of bioanalytes is a basic requirement of a lab on chip device. To deal with it, certain studies exclusively focused on the high speed<sup>30</sup> and high throughput<sup>24</sup> of MBs. Individual moving MBs show a broadly varying response, as revealed by experiments on MBs populations.<sup>27–31</sup> Although, the heterogeneities among different types of moving MBs were accurately quantified as Gaussian distributions,<sup>29,31</sup> to overcome or compensate this magnetic heterogeneity for the reproducible motion and accurate separation is an open question. The situation becomes challenging, when the separation of multiple size MBs from mixed populations is desired.



**Figure 3.5:** (a) Average critical frequency  $f_{crit}$  for  $\varnothing_{MB}=2\ \mu\text{m}$ – $12\ \mu\text{m}$  is determined over a hundred of single circulating MBs around the 30  $\mu\text{m}$  diameter NiFe disk under  $H_{ext}=16$  kA/m. (b) Susceptibility  $\chi$  is normalized for single MBs at the equal  $H_{ext}$ . (c) Magnetic properties define the MB size dependent  $\chi$  and  $f_{crit}$ .

Confirmed by our model system, all the MBs ( $\varnothing_{MB}=2\ \mu\text{m}-12\ \mu\text{m}$ ) employed in this research work, show a heterogeneous magnetic response. At a fixed applied field  $H_{ext} = 16\ \text{kA/m}$ , individual populations are quantified through determining the critical frequency  $f_{crit}$  of single MBs circulating around the NiFe disk structures with the  $30\ \mu\text{m}$  diameter. For all sizes, experiments over a hundred single moving MB reveal the dependence of the average critical frequency on the size of the MB, as shown by their histograms in Fig. 3.5 a. Deviating values of  $f_{crit}$  from the fitting parameter, FWHM (full width at half maximum) are measures of higher or lower magnetic moments inside single MBs. For the MBs used for separation experiments ( $\varnothing_{MB}=2\ \mu\text{m}-8\ \mu\text{m}$ ), the difference in  $f_{crit}$  is within a range of  $\approx 1.1\times-1.6\times$ , resulting from competition between the magnetic and hydrodynamic drag force, depending on the particle size (see eq. 1.19).

Using the magnetic characterization approach,<sup>58</sup> the MB size dependent volume susceptibility  $\chi$  are determined from the volume magnetization, normalized to single MBs (see Fig. Appendix-A.2). For a fixed  $H_{ext} = 16\ \text{kA/m}$ , the  $\chi$  differs in a range of  $\approx 1.1\times-1.3\times$  for MBs with different diameters. Comparing the  $\chi$  and  $f_{crit}$  values depending on the diameter of MBs (last two columns in Fig. 3.5 c), it is understood that the  $\chi$  is a dominating function of iron density inside MBs, while the average  $f_{crit}$  results from an interplay between the volume ( $r^3$ ) and the radius ( $r$ ) of the magnetic MB, moving around a magnetic structure (eq. 1.19).

## Discussion and Summary

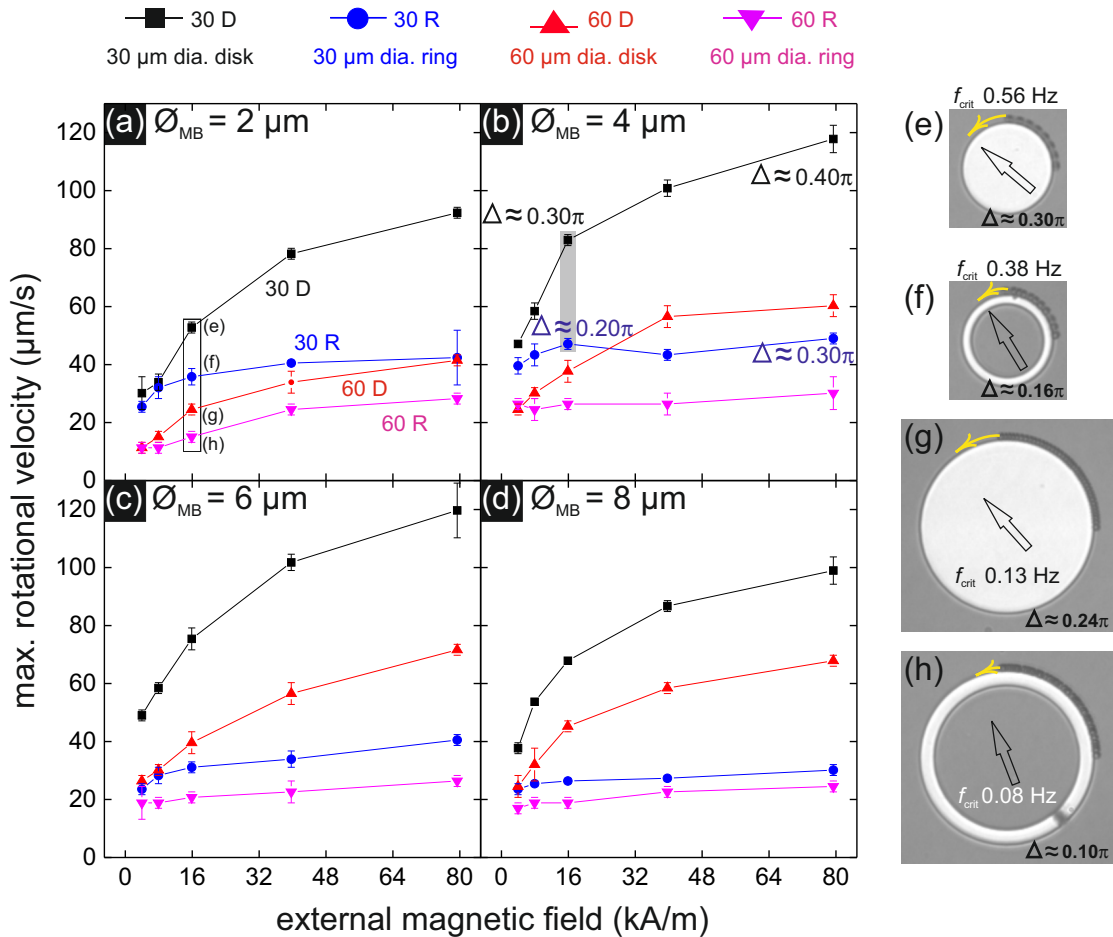
For the magnetic characterization the critical frequency of the moving beads is selected due to two reasons: Firstly, since the hydrodynamics drag force increases with the speed of the bead, the slow circulating bead stays closer to the moving  $H_{ext}$ , whereas the fast moving bead lags largely behind the  $H_{ext}$  (Appendix-A.1). Due to a large angular lag, the motion of the bead is greatly influenced by its magnetic content. This provides a clear understanding of the effect of magnetic heterogeneity on the motion of MBs populations. Secondly, as the maximum speed of a moving MB is attained around its  $f_{crit}$ , it is the regime of most interest for the high throughput LoC applications.

Despite the smallest  $2\ \mu\text{m}$  beads have the highest density of iron, they showed a lower  $f_{crit}$  and thus slower speed. This explains how the effective magnetic volume of a particle defines its achievable speed around a magnetic structure (eq. 1.19). The largest  $12\ \mu\text{m}$  beads showed the lowest  $f_{crit}$ , due to an increased hydrodynamic drag and a low weight percent magnetic content (not shown here). Largely dissimilar values of  $\chi_v$  at zero fields are related to the variation in iron doping among different sizes of MBs. With an average critical frequency  $f_{crit}$  of the different MBs the effect of size and form of MB moving magnetic structures for the maximum achievable velocity can be determined. The applied field dependent susceptibility of MBs<sup>42,59</sup> is discussed in the coming section.

### 3.3 MB Circulating Motion Dependence on Magnetic Structures

The magnetic force on a magnetic MB depends directly on the stray field generating micromagnetic feature of the magnetic structure MS. The proper size and type of the MS, providing the higher magnetic field gradient, enables the higher speed of a MB's motion. Analyzing the movement of a single magnetic particle along a transverse like domain wall configuration at a Permalloy disk<sup>42</sup> versus its motion along a vortex domain wall in a ring element<sup>30</sup> helps in the selection of the MSs.

Experiments show that a MB has different velocities for its motion around disk and ring MSs. To quantify the change in the velocity, we determine the motion of different size micromer-M microbeads, individually around various disk and ring NiFe MSs. For different amplitudes of  $H_{ext}$  the maximum velocities of single moving MBs, as a function of their critical frequency ( $f_{crit}$ ), are summarized in Fig. 3.6.



**Figure 3.6:** Dependence of the microbead average velocity ( $v_{ave}$ ) on the type and size of circular NiFe magnetic structures and the improved  $v_{ave}$  for increasing amplitudes of  $H_{ext}$ . Single MBs with a diameter of 2  $\mu\text{m}$  (a), 4  $\mu\text{m}$  (b), 6  $\mu\text{m}$  (c) and 8  $\mu\text{m}$  (d) showing different  $v_{ave}$  on the disk and ring MSs. (e)-(h) Phase lag of a 2  $\mu\text{m}$  diameter bead, defined by its critical frequency.

### MBs Velocity around a Disk

The model structure NiFe disk with  $30\ \mu\text{m}$  diameter shows the most substantial improvement in the average velocity  $v_{ave}$  for all MBs with increasing the  $H_{ext}$  strength (black symbols in Fig. 3.6 a-d). A quasi linear increase in the circulating velocity  $v_{ave}$  is observed for low and medium strength magnetic field  $H_{ext}$ . Afterwards, a nonlinear growth and flattening of velocity curves towards the high strength magnetic field is attributed to the saturation of the superparamagnetic particles and the influence of magnetic structure.<sup>5,42,60</sup> All size MBs determine an increment from  $\approx 2.5\times$  to  $\approx 3\times$  in their  $v_{ave}$  at highest applied  $H_{ext}$  of 80 kA/m against the lowest  $H_{ext}$  of 4 kA/m.

### MBs Velocity around a Ring

For lower strength  $H_{ext}$ ,  $2\ \mu\text{m}$  and  $4\ \mu\text{m}$  diameter MBs move slightly slower around the ring structure with an external diameter of  $30\ \mu\text{m}$  in comparison to their velocity  $v_{ave}$  around the disk (blue vs black symbols in Fig. 3.6 a and b). The difference in  $v_{ave}$  increased gradually for increasing strength  $H_{ext}$  and reached to enormously different values at the high values of  $H_{ext}$ . Large size  $6\ \mu\text{m}$  and  $8\ \mu\text{m}$  diameter beads (Fig. 3.6 c vs d) already exhibit far lower  $v_{ave}$  at lower field strength. In a similar system,<sup>60</sup> the magnetic force is determined to be constant for a particle above the critical size. Since, the local demagnetizing field and field gradient is different at the outer and inner perimeter of ring patterns, as shown by a study,<sup>61</sup> the overall effective gradient on the MB is expected to be different than on disk patterns. Also, the radial force which binds the bead with the magnetic structure, falls off rapidly, when the bead size is larger than the critical limit.<sup>5</sup> In the presence of lower magnetic forces from NiFe ring elements, the increased hydrodynamic drag force causes the low circulating velocity  $v_{ave}$  of large magnetic beads (see eq. 1.19).

### MBs Velocity around a Disk and Ring with Larger Diameter

When the low circulating velocities on a  $60\ \mu\text{m}$  disk are compared to the high velocities from a  $30\ \mu\text{m}$  disk (red vs black symbols in Fig. 3.6 a-d), a similar increment in the velocity  $v_{ave}$  is noticed for all applied values of  $H_{ext}$ . These results reasonably match with the finding<sup>5</sup> and suggest that the velocity of the magnetic particles decreases, when the ratio of particle to disk size is above or below a critical limit. Therefore, a disk with twice a large diameter causes a reduction in the velocity of magnetic MBs. Nonetheless, large disks, showing the increased speed of large particles at a high amplitude field  $H_{ext} = 80\ \text{kA/m}$  explain the effect of structure geometry. At equal magnetic fields ring structures showed an ignorable increment in the beads' velocity. Compare the  $v_{ave}$  values in Fig. 3.6 c and d (red against blue and pink symbols). Therefore, the velocity maximization at high strength  $H_{ext}$  is not related to the saturation effects of magnetic particles at the first place. Instead, it is the non-favorable field gradient on the magnetic particle which limits its achievable velocity. Overall, the lowest average velocity is determined on ring structures with  $60\ \mu\text{m}$  outer diameter (pink symbols in

Fig. 3.6 a-d).

### 3.3.1 Angular Phase Lag of Moving Microbeads

The phase lag of moving beads in relation to the rotating  $H_{ext}$  is a useful property, which can be utilized for the sorting of different beads on periodic magnetic structures. Following factors define the character of a bead, moving with an angular lag around a circular structure: Firstly, since the critical frequency  $f_{crit}$  of a circulating bead is related to its angular position, a large phase lag occurs due to the high  $f_{crit}$  around the disk, whereas a small lag occurs for the low  $f_{crit}$  around the ring (Fig. 3.6 e vs f). Secondly, the phase lag increases with the increased speed of the bead for higher strength magnetic fields. For example, a  $4 \mu m$  diameter particle moving around the  $30 \mu m$  disk shows a different amplitude of phase lag for  $H_{ext} = 16$  and  $80$  kA/m (labeled in Fig. 3.6 b).

#### Summary

Single magnetic MBs with diameter varying from  $2 \mu m$  to  $8 \mu m$  show different speeds depending on the size and type of circular magnetic structures. At the higher amplitude magnetic field the increment in the velocity of microbeads is achievable largely on disk elements. Depending on the application and required size and speed of the particles, small ring elements might still be a choice for the small  $2 \mu m$  and  $4 \mu m$  diameter particles moving at lower fields with speeds comparable to the disk element. In contrast, moving large particles with high speeds on ring magnetic elements is impractical. The results are adverse for large size ring structures.



### 3.4 Microbead Transport on Magnetic Tracks

Due to the elongated shape of magnetic tracks MTs, they can be employed to transport magnetic MBs. MTs with rounded and pointed magnetic features were investigated to move the magnetically labeled biological analytes.<sup>4,5,62</sup> The size of plane magnetic arrays was optimized to increase the speed of MBs.<sup>63</sup> However, the geometry of the MB moving magnetic feature together with the type of MB has not been shown for the maximization of transport speed on a MT. The separation of different MBs on magnetic tracks did not receive much attention in the past. This requires a systematic characterization of MBs on MTs with appropriate size and geometry, so that the underlying fast and separating movements of MBs can be realized.

In this section, various thin film NiFe MTs with different lateral dimensions and shapes are investigated for directed movements and speeds of micromer-M MBs with 2, 4, 6 and 8  $\mu m$  diameters. Using an external rotating in-plane magnetic field, the linear and nonlinear motions of MBs are revealed. MTs move single MBs with different speeds due to their size dependent critical frequency  $f_{crit}$ . An understanding of spatial and dynamic response of moving MBs, defined by the MT geometry is obtained. To explain the MBs movement patterns, static images of MBs motion trajectories for specific field orientations are extracted and analyzed using the stray magnetic field gradient FG mapped by MFM and calculated by MM. Motion paths of moving MBs below and above their critical frequency  $f_{crit}$  are plotted as cumulative distance traveled along a MT ( $\mu m$ ) vs  $H_{ext}$  rotations ( $\pi$ ). MBs' size dependent average velocities during continuous and looping motions are determined. Finally, the effect of the MT size and the amplitude of  $H_{ext}$  on the transport speed of MBs is discussed.

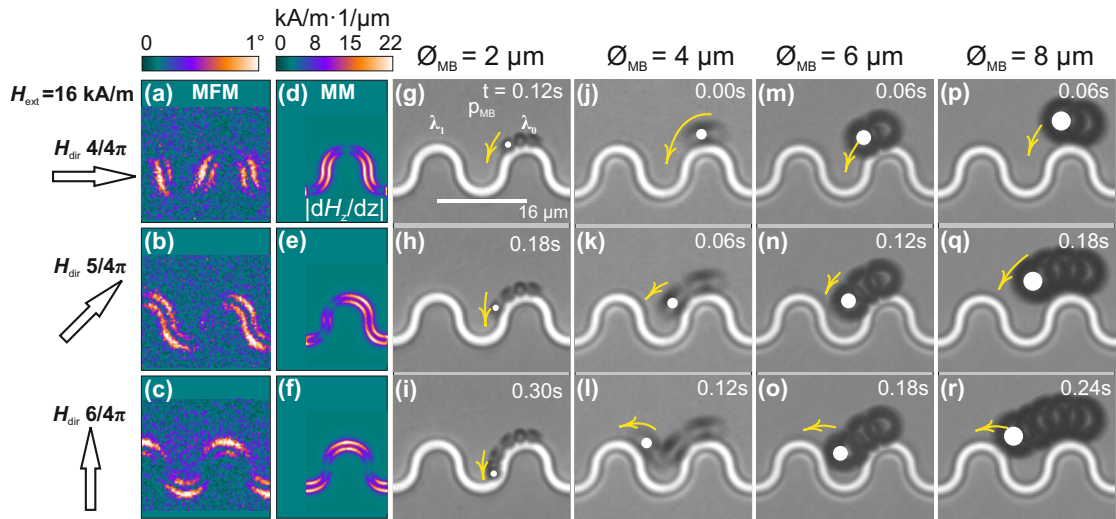
Experiments and simulations showed that  $H_{ext} = 16$  kA/m is sufficient to magnetize the 30 nm thick NiFe patterns for the controlled transport of MBs. Hence, the amplitude of  $H_{ext}$  is fixed for the shown results. Depending on the initial position of the MB and the sense of field rotation, the directed motion occurs along either side of MTs and generally it continues, until the end of tracks. Here, we define the upper side of tracks as a starting position of a MB, moving along a characteristic segment of tracks  $\lambda$  (from the initial position  $\lambda_0$  to a position  $\lambda_3$  for three periodic movement steps) under a rotating  $H_{ext}$ .

### 3.4.1 Directed Transport on a Curvilinear Track

The design of a symmetric curvilinear track is an extension of the ring elements, which are half segmented and horizontally shifted by their diameter to form an elongated pathway. A  $2\ \mu\text{m}$  wide MT with an apex-to-apex distance of  $16\ \mu\text{m}$  is employed. Alternative concave and convex magnetic features over the track enable various movement patterns of MBs depending on their size with an applied magnetic field  $H_{ext}$  homogeneously rotating in the chip plane.

#### Movement Patterns on a Curvilinear Track

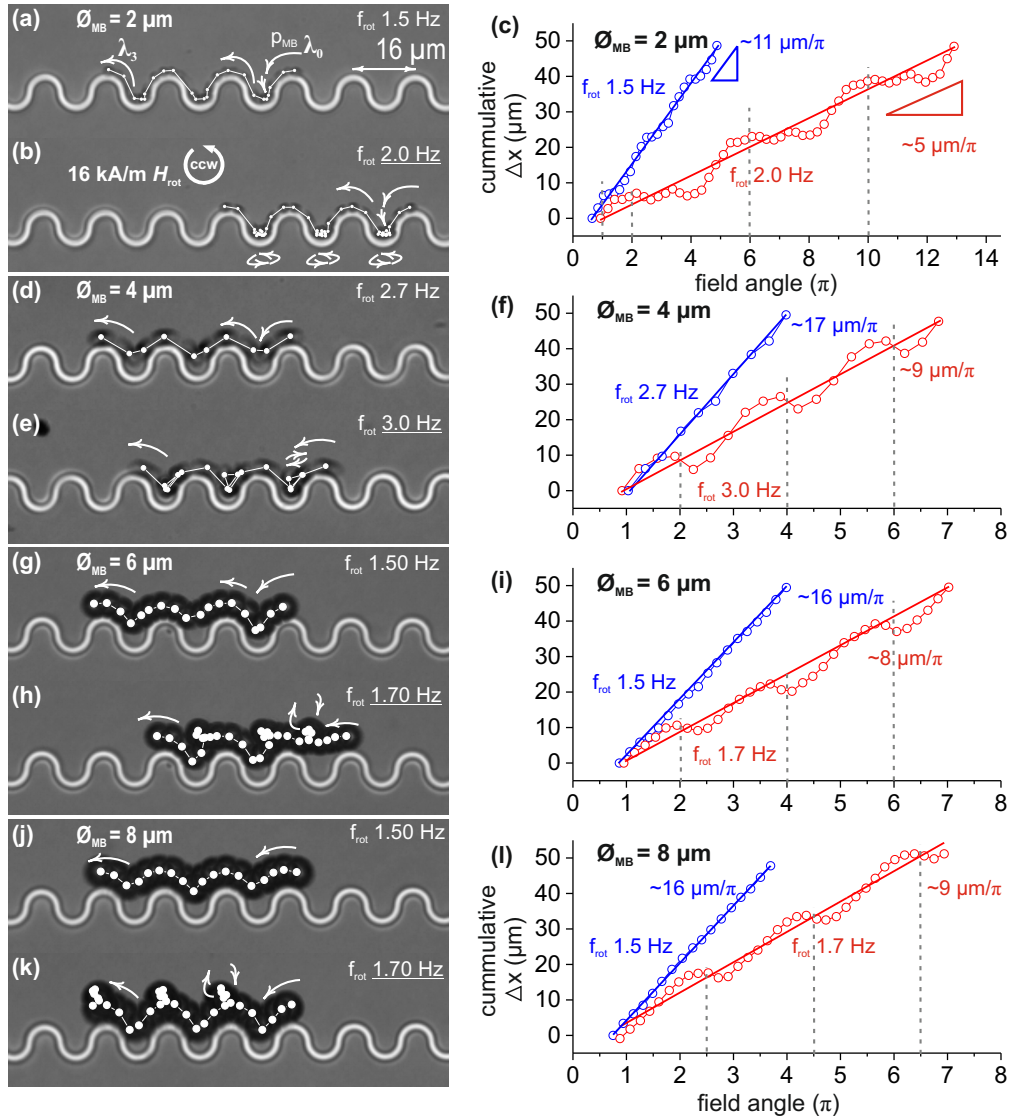
At a static in-plane applied magnetic field of  $16\ \text{kA/m}$ , the MFM signals (Fig. 3.7 a-c) and the distribution of stray magnetic field gradients for horizontal, oblique and vertical in-plane field orientations (Fig. 3.7 d-f) explain the MBs directed movement. Shown in Fig. 3.7 g, a  $2\ \mu\text{m}$  bead starting its motion at an apex  $\lambda_0$ , lags behind the maximum field gradient FG for the horizontal orientation of rotating  $H_{ext}$ . Its motion trajectories, obtained for the oblique and vertical orientation of  $H_{ext}$  (Fig. 3.7 h-i) signify its resting at the local minima. This is followed by no MB motion through the weaker FG at the concave region. In comparison, the  $4\ \mu\text{m}$  diameter bead, due to its high magnetic volume, directly reaches the next concave segment (MT position =  $\lambda_1$ ) as shown in Fig. 3.7 l. Identically,  $6\ \mu\text{m}$  (Fig. 3.7 m-o) and  $8\ \mu\text{m}$  (Fig. 3.7 p-r) beads travel from one apex to the next over the track, following the changing angular position of FG maxima.



**Figure 3.7:** Stray field gradients (MFM, a-c) and out-of-plane component of stray field gradients (MM, d-f), obtained at a height of  $500\ \text{nm}$  above the track, for selected  $H_{ext}$  orientations. Experimental images at the corresponding orientations of  $H_{ext}$ , show the motion trajectories of a  $2\ \mu\text{m}$  (g-i),  $4\ \mu\text{m}$  (j-l),  $6\ \mu\text{m}$  (m-o) and  $8\ \mu\text{m}$  bead (p-r). From the track position  $\lambda_0$ , the  $2\ \mu\text{m}$  bead stopped at the concave segment, while  $4$ ,  $6$  and  $8\ \mu\text{m}$  beads reached  $\lambda_1$ , following the moving field gradient. White dots and yellow arrows show the positions and direction of moving MBs.

### Continuous and Looping Transport on the Curvilinear Track

A  $2\ \mu\text{m}$  bead moves from right to left direction over the track under a counter clockwise rotating field  $H_{ext}$  with a constant frequency  $f_{rot} = 1.5\ \text{Hz}$  (Fig. 3.8 a). For a higher  $f_{rot}$  (2 Hz), the bead loops at the concave segments, with alternating forward steps on the track. The motion path for the looping accompanied transport is shown in Fig. 3.8 b. Plotting the motion trajectories as cumulative distance  $\Delta x$  against the magnetic field rotations (Fig. 3.8 c) describes a high slope for the continuous motion, whereas the lower slope for the looping motion.

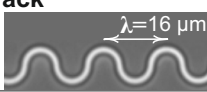


**Figure 3.8:** Recorded motion of a  $2\ \mu\text{m}$  bead from  $\lambda_0$  to  $\lambda_3$  under a ccw-rotating  $H_{ext}$  with the different  $f_{rot}$  for the continuous (a) and looping motion (b). (c) Plotted  $\Delta x$  positions of the moving bead against field rotations are superimposed with slopes ( $\mu\text{m}/\pi$ ). High and low slopes represent the continuous and looping motion. (d)-(f)  $4\ \mu\text{m}$  bead, (g)-(i)  $6\ \mu\text{m}$  bead and (j)-(l)  $8\ \mu\text{m}$  beads with their continuous and looping movements and plotted traveled paths. Reduced slopes correlate to the looping events.

Due to its small magnetic volume, the  $2\ \mu\text{m}$  bead does not follow the field gradient at the concave region initially, even for its non-looping motion. An additional  $\pi$  field rotation is required for a period travel of  $16\ \mu\text{m}$  over the track (Fig. 3.8 c). The  $4\ \mu\text{m}$  bead, due to a higher magnetic volume susceptibility  $\chi_v$ , takes larger movement steps during the continuous motion (Fig. 3.8 d) and the loopings appear as fast backward steps (Fig. 3.8 e). The regular high slope, comprising the traveled distance  $3\cdot\lambda$  under field rotations of  $3\cdot\pi$  in Fig. 3.8 f, depicts a linear motion compared to the looping response with the low slope. The regular occurrence of the looping is identified as a  $2\pi$  periodicity in the plot. Stronger falls in the red curve at field positions  $2\pi$ ,  $4\pi$  and  $6\pi$  correspond the backward motion of the particle during its looping.  $6\ \mu\text{m}$  and  $8\ \mu\text{m}$  diameter beads with their interactive size close to the element size, exhibit lower critical frequency  $f_{crit}$ . The broad distribution of stray field gradient FG at the round magnetic feature, effective on the large moving particle also from the backward, causes their lower  $f_{crit}$ . Nevertheless,  $6\ \mu\text{m}$  and  $8\ \mu\text{m}$  particles move continuous, following the FG maxima at the convex segments (Fig. 3.8 g and j). The looping periodicity is producible at a higher rotational frequency of the field (Fig. 3.8 h and k). Slight falls in the cumulative  $\Delta x$  curves in Fig. 3.8 i and l indicate the stops in the directional motion and the  $2\pi$  periodicity of the looping motion. See Appendix-E.1.1 Movie 3.7-3.10.

### Microbead Velocities on a Curvilinear Track

The average velocity  $v_{ave}$  of different magnetic particles, just below their critical frequency  $f_{crit}$  are determined on the curvilinear tracks. Above  $f_{crit}$ , the reduction in  $v_{ave}$  directly relates to the number of periodic loopings. For example, the directed motion of a particle, including one looping per  $\lambda$ , causes a half reduced  $v_{ave}$ . Microbead velocities below and above their  $f_{crit}$  are summarized in Tab. 3.1.

Microbead velocities on a curvilinear track 	$\varnothing_{MB} = 2\ \mu\text{m}$		$\varnothing_{MB} = 4\ \mu\text{m}$		$\varnothing_{MB} = 6\ \mu\text{m}$		$\varnothing_{MB} = 8\ \mu\text{m}$	
	( $\mu\text{m/s}$ )	(Hz)	( $\mu\text{m/s}$ )	(Hz)	( $\mu\text{m/s}$ )	(Hz)	( $\mu\text{m/s}$ )	(Hz)
$v_{ave, x-dir}$ <b>below</b> $f_{crit}$ (continuous)	~34	1.5	~90	2.7	~48	1.50	~48	1.50
$v_{ave, x-dir}$ <b>above</b> $f_{crit}$ (looping)	~18	2.0	~54	3.0	~25	1.70	~24	1.70

**Table 3.1:** Average velocities from the continuous and looping motion of MBs. MBs'  $v_{ave}$  reduces  $\approx 2x$  above their  $f_{crit}$ . The MB size for highest  $v_{ave}$  is highlighted green.

## Summary

Magnetic particles exhibit size dependent distinct critical frequencies  $f_{crit}$  for their continuous motion over a curvilinear magnetic track.  $2\ \mu m$  diameter particles with their too small interactive volume relative to the period length of track  $\lambda$ , cannot follow the fast changing magnetic field gradient FG. As a result, they have low  $f_{crit}$  and thus reduced velocity  $v_{ave}$ .  $4\ \mu m$  particles, with a proper size matching with the  $\lambda$  of track, move the fastest. The fast forward motion of larger particles ( $6\ \mu m$  and  $8\ \mu m$ ) is hindered from the backward FG, due to their high interactive volume. The broader distribution of magnetic FG at the round magnetic features, together with the increased drag force, causes the low  $v_{ave}$  of large particles. Nonetheless, at higher  $f_{rot}$  of  $H_{ext}$  the periodic looping motion enables a twofold reduction in the average transport velocity of all particles. Zigzag shaped tracks with the highly localized FG at the magnetic corners move particles differently, than curvilinear tracks, as shown next.

### 3.4.2 Directed Transport on a Zigzag Track

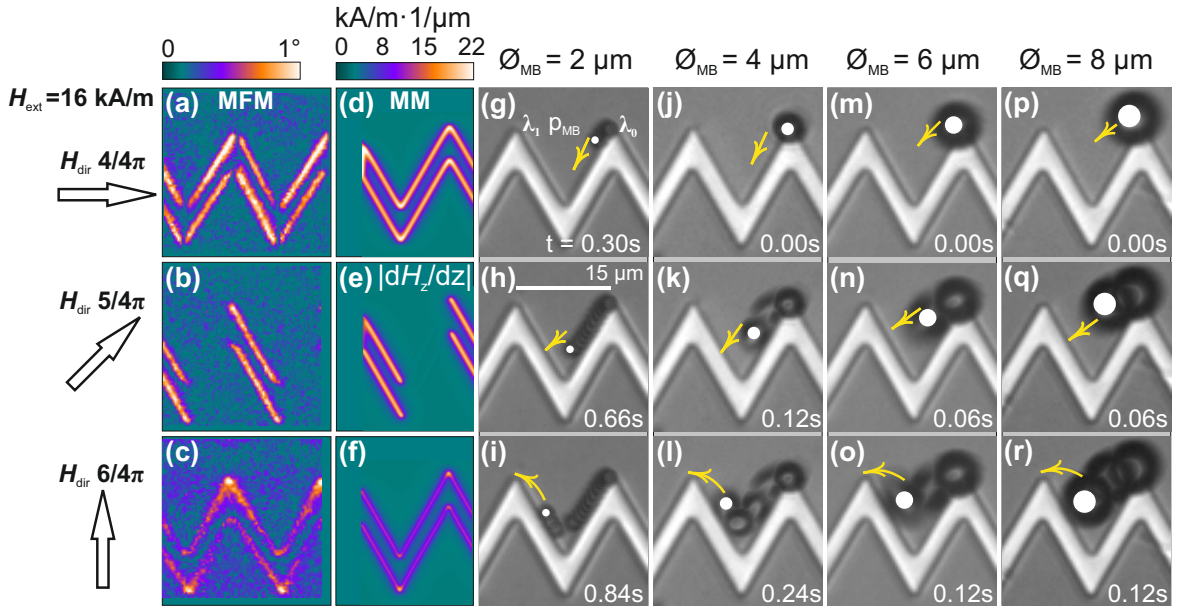
A magnetic track having a zigzag configuration with  $\beta = \pi/3$  can transport the magnetic microbeads. The NiFe element with a width of  $3.5\ \mu m$  and an apex-to-apex distance of  $15\ \mu m$  enables the movement of MBs through the straight edge and tip magnetic features.

#### Movement Patterns on a Zigzag Track

Varying magnetic stray field gradient at the apex and edge regions for three selected orientations of  $H_{ext}$  are determined using MFM imaging (Fig. 3.9 a-c) and MM calculations (Fig. 3.9 d-f). Fig. 3.9 g shows the motion of a  $2\ \mu m$  bead for the horizontal orientation of rotating  $H_{ext}$ , started from an apex  $\lambda_0$ . When  $H_{ext}$  orients more perpendicular to the edge, then the particle moves towards this edge, as a result of the shifted position of the FG (Fig. 3.9 h). The trace of particle motion at the vertical component of  $H_{ext}$  in Fig. 3.9 i describes its movement towards the next apex  $\lambda_1$ . Magnetic FG maxima at the tip in Fig. 3.9 c and Fig. 3.9 f depicts the magnetic attraction for the particle. Similarly, a  $4\ \mu m$  bead follows the moving point of FG maximum, as shown by its motion pattern in Fig. 3.9 j-l. The motion traces of  $6\ \mu m$  (Fig. 3.9 m-o) and  $8\ \mu m$  (Fig. 3.9 p-r) particles depict their direct attraction to the opposite edge.

#### Continuous and Looping Transport on a Zigzag Track

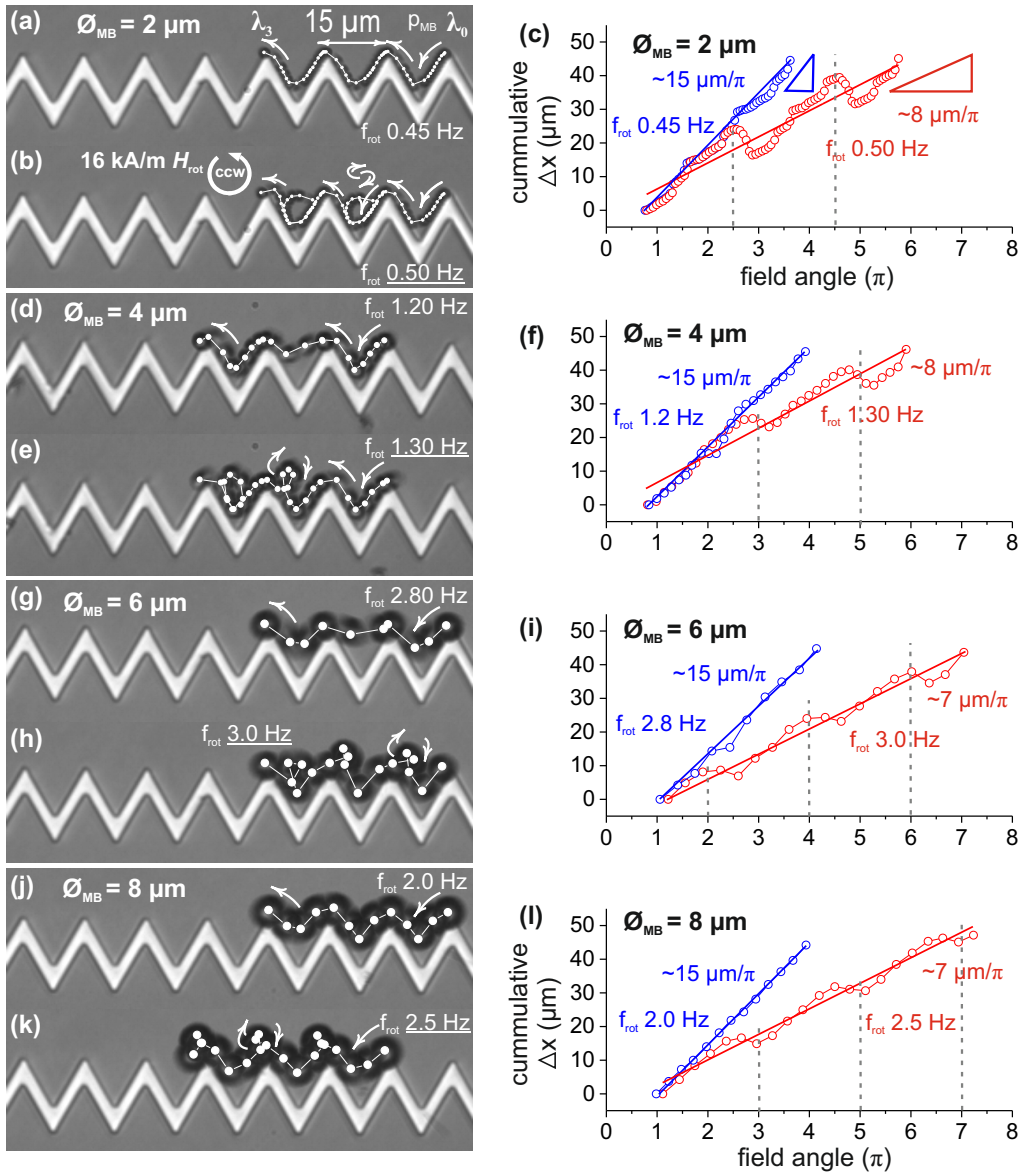
Transport of a  $2\ \mu m$  bead from one apex to the next over a zigzag track occurs via small movement steps through the flat edges under a ccw-rotating  $H_{ext}$  (Fig. 3.10 a). At higher field frequencies the  $2\ \mu m$  bead is unable to follow the passing FG at the



**Figure 3.9:** Stray field gradients (MFM, a-c) and out-of-plane component of stray field gradients (MM, d-f), obtained at a height of 500 nm above the track, for selected  $H_{ext}$  orientations. Experimental images at the corresponding orientations of  $H_{ext}$ , show the motion trajectories of a 2  $\mu\text{m}$  (g-i), 4  $\mu\text{m}$  (j-l), 6  $\mu\text{m}$  (m-o) and 8  $\mu\text{m}$  bead (p-r). From the track position  $\lambda_0$ , 2  $\mu\text{m}$  and 4  $\mu\text{m}$  beads moved along the edges, whereas 6  $\mu\text{m}$  and 8  $\mu\text{m}$  beads directly moved to the next tip, at the track position  $\lambda_1$ , following the moving field gradient.

tip, due to its small magnetic volume. Consequently, it falls behind via attraction to the nearest FG at the backward edge, which leads to a big looping between two edges of the track. An exemplary response is shown in Fig. 3.10 b.

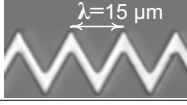
Traveled paths as cumulative  $\Delta x$  vs field rotations for the continuous and looping motion are plotted in Fig. 3.10 c. Strong falls in the curve of tracked  $\Delta x$  at field angles  $2.5\pi$  and  $4.5\pi$  translate the  $2\pi$  periodicity and the extent of backward looping. The 4  $\mu\text{m}$  bead with a higher critical frequency takes relatively bigger movement steps. Accordingly, the spatial extent of looping is shorter in Fig. 3.10 e and f. An irregularity in the looping periodicity for 2  $\mu\text{m}$  and 4  $\mu\text{m}$  MB, is likely because of a uniform distribution of FG along the flat edges and much higher FG at apexes and their abrupt changing positions on the zigzag pathway. Observations revealed that the small particles either skipped the looping or took multiple looping between the long edges of a zigzag track during their nonlinear movement. Large beads with larger interactive volume and thus higher critical frequencies are transported along fast moving FG, which are predominantly stronger at the sharp tips. Therefore, 6  $\mu\text{m}$  and 8  $\mu\text{m}$  beads take long movement steps for the linear (Fig. 3.10 g and Fig. 3.10 j) and nonlinear (Fig. 3.10 h and Fig. 3.10 k) response. At higher  $f_{rot}$  of  $H_{ext}$  typical reduced slopes for large particles in Fig. 3.10 i and Fig. 3.10 l correspond to a regular  $2\pi$  periodicity of the looping motion. See Appendix-E.1.1 Movie 3.11-3.14.



**Figure 3.10:** Recorded motion of a  $2 \mu\text{m}$  bead from  $\lambda_0$  to  $\lambda_3$  under a ccw-rotating  $H_{ext}$  with the different  $f_{rot}$  for the continuous (a) and looping motion (b). (c) Plotted  $\Delta x$  positions of the moving bead against field rotations are superimposed with slopes ( $\mu\text{m}/\pi$ ). High and low slopes represent the continuous and looping motion. (d)-(f)  $4 \mu\text{m}$  bead, (g)-(i)  $6 \mu\text{m}$  bead and (j)-(l)  $8 \mu\text{m}$  beads with their continuous and looping movements and plotted traveled paths. Reduced slopes correlate to the looping events.

### Microbead Velocities on a Zigzag Track

$6 \mu\text{m}$  and  $8 \mu\text{m}$  diameter MBs show higher average velocity  $v_{ave}$  over the zigzag magnetic track than  $4 \mu\text{m}$  beads. The  $4 \mu\text{m}$  beads exhibits higher  $v_{ave}$  than the  $2 \mu\text{m}$  bead. Microbead transport velocities below and above their  $f_{crit}$  are summarized in Tab. 3.2.

Microbead velocities on a zigzag track 	$\varnothing_{MB} = 2 \mu\text{m}$		$\varnothing_{MB} = 4 \mu\text{m}$		$\varnothing_{MB} = 6 \mu\text{m}$		$\varnothing_{MB} = 8 \mu\text{m}$	
	( $\mu\text{m/s}$ )	(Hz)	( $\mu\text{m/s}$ )	(Hz)	( $\mu\text{m/s}$ )	(Hz)	( $\mu\text{m/s}$ )	(Hz)
$v_{\text{ave, x-dir}}$ <b>below</b> $f_{\text{crit}}$ (continuous)	~13	0.45	~37	1.20	<b>~87</b>	<b>2.80</b>	~60	2.0
$v_{\text{ave, x-dir}}$ <b>above</b> $f_{\text{crit}}$ (looping)	~8	0.5	~21	1.30	~43	3.0	~30	2.5

**Table 3.2:** Average velocities from the continuous and looping motion of MBs. MBs'  $v_{\text{ave}}$  reduces  $\approx 2x$  above their  $f_{\text{crit}}$ . The MB size for highest  $v_{\text{ave}}$  is highlighted green.

## Summary

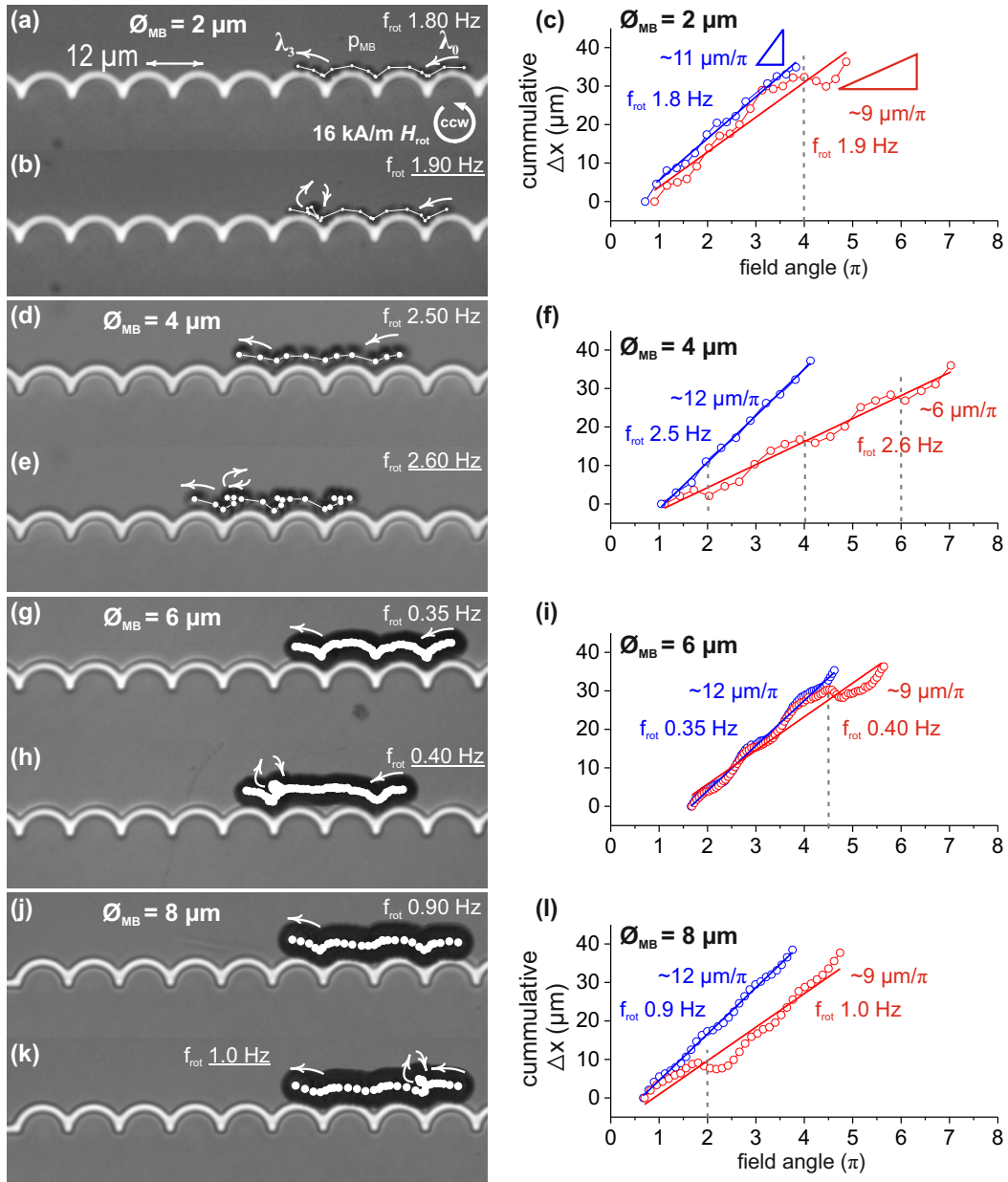
The NiFe zigzag pathway, providing uniform field gradient FG along straight edges and much higher FG at apexes, determine the particle size dependent diverse critical frequencies. Because of a too small interactive volume relative to the period length of track  $\lambda$ ,  $2 \mu\text{m}$  particles move slower than  $4 \mu\text{m}$  particles. Large particles with  $6 \mu\text{m}$  and  $8 \mu\text{m}$  diameter with higher effective volume are readily attracted by the fast changing FG at edges and tips over the zigzag magnetic pathway, resulting in faster MB speeds. Hence, pointed features of soft magnetic elements, with a proper match between the particle size and period length of a track, improved the velocity of large particles. In contrast, the round magnetic features on curvilinear track moved the  $4 \mu\text{m}$  particle faster than  $6 \mu\text{m}$  and  $8 \mu\text{m}$  particles in Sec. 3.4.1. Next, we study the effect of track geometry on the speed, by analyzing the movement of the same single particles, first on convex shaped tracks and then on concave magnetic tracks.

### 3.4.3 Directed Transport on a Convex Track

Since the distribution and strength of stray magnetic field gradient directly effect the MB motion and speed, the shape of a magnetic structure, being in close physical contact with a moving MB, is a deciding factor. In contrast to the alternating concave and convex segments (Sec. 3.4.1), which cause an intermittent transport of small beads, a straight joining of half ring elements forming a convex magnetic pathway might affect the movement patterns of small and large MBs differently. Now, we reveal the MB movements over a convex shaped  $2 \mu\text{m}$  wide NiFe track with an apex-to-apex distance of  $12 \mu\text{m}$ .







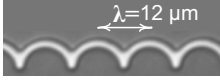
**Figure 3.12:** Recorded motion of a  $2 \mu\text{m}$  bead from  $\lambda_0$  to  $\lambda_3$  under a ccw-rotating  $H_{ext}$  with the different  $f_{rot}$  for the continuous (a) and looping motion (b). (c) Plotted  $\Delta x$  positions of the moving bead against field rotations are superimposed with slopes ( $\mu\text{m}/\pi$ ). High and low slopes represent the continuous and looping motion. (d)-(f)  $4 \mu\text{m}$  bead, (g)-(i)  $6 \mu\text{m}$  bead and (j)-(l)  $8 \mu\text{m}$  beads with their continuous and looping movements and plotted traveled paths. Reduced slopes correlate to the looping events.

The widely distributed field gradient FG with a varying amplitude causes a lower  $f_{crit}$  for large moving beads. The alternating higher and lower amplitude of the FG causes the respective motion and resting of the particles between apexes on the track. As an effect, the motion patterns appear as oscillations in the cumulative distance  $\Delta x$  curves (Fig. 3.12i and Fig. 3.12l). The looping motion of  $6 \mu\text{m}$  and  $8 \mu\text{m}$  beads is also non-periodic, which is likely related to the irregular interaction of the FG with large

beads. An increased hydrodynamic drag for larger diameter beads also contributes to their lower  $f_{crit}$  (see Eq. 1.19). Particularly, the  $6 \mu m$  beads show a far lower  $f_{crit}$ . Divergent values of  $f_{crit}$  for  $6 \mu m$  and  $8 \mu m$  particles are due to the magnetic heterogeneity among single particles (see Sec.3.2).

### Microbead Velocities on a Convex Track

Small size MBs with  $2 \mu m$  and  $4 \mu m$  diameter with higher critical frequency on the convex track, offer higher averaged velocity than the large beads. Microbead velocities below and above their  $f_{crit}$  are summarized in Tab. 3.3.

Microbead velocities on a convex track 	$\emptyset_{MB} = 2 \mu m$		$\emptyset_{MB} = 4 \mu m$		$\emptyset_{MB} = 6 \mu m$		$\emptyset_{MB} = 8 \mu m$	
	( $\mu m/s$ )	(Hz)	( $\mu m/s$ )	(Hz)	( $\mu m/s$ )	(Hz)	( $\mu m/s$ )	(Hz)
$v_{ave, x-dir}$ <b>below</b> $f_{crit}$ (continuous)	~39	1.8	~60	2.5	~8	0.35	~22	0.90
$v_{ave, x-dir}$ <b>above</b> $f_{crit}$ (looping)	~34	1.9	~31	2.6	~7	0.40	~17	1.0

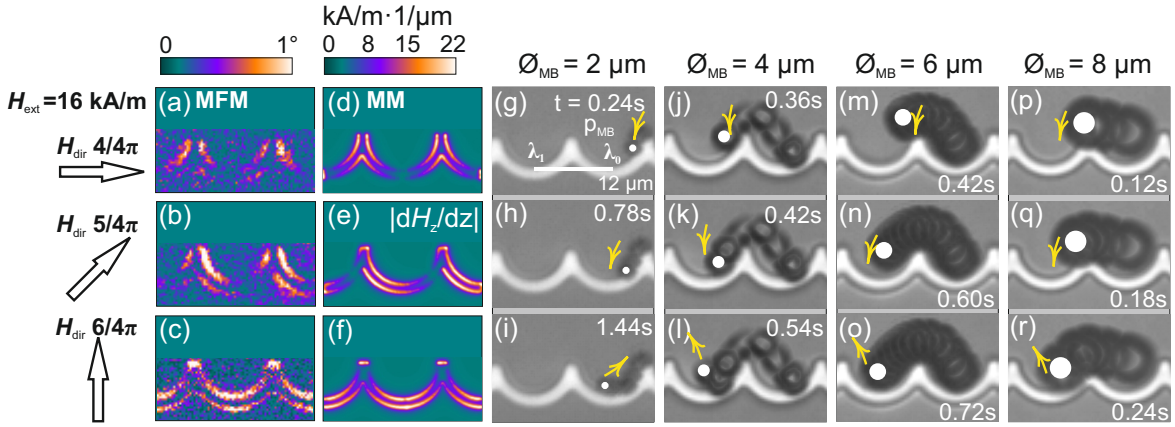
**Table 3.3:** Average velocities from the continuous and looping motion of MBs. MBs'  $v_{ave}$  reduces above their  $f_{crit}$ . The MB for highest  $v_{ave}$  is highlighted green.

### Summary

The convex shaped NiFe elongated magnetic tracks determine clearly different critical frequency  $f_{crit}$  of MBs, depending on their size. The  $2 \mu m$  bead, due to its small interactive volume and so being less affected by the backward field gradient FG, can be moved faster along the forward moving FG. Therefore, it shows a higher  $f_{crit}$  on the convex track. The  $4 \mu m$  bead, with even higher  $f_{crit}$ , shows the highest transport velocity. Because of the higher interactive volume, the motion of  $6 \mu m$  and  $8 \mu m$  beads is disturbed by the backward moving FG. The wide distribution of the FG on the round magnetic features of the convex track complicates the motion of large magnetic particles, resulting in their lower  $v_{ave}$ . However, the motion of small particles is eased. To confirm the influence of differently shaped magnetic features on the particle speed, we analyze the motion response of same single particles, now on the concave-pointed magnetic track in the next section.

### 3.4.4 Directed Transport on a Concave-pointed Track

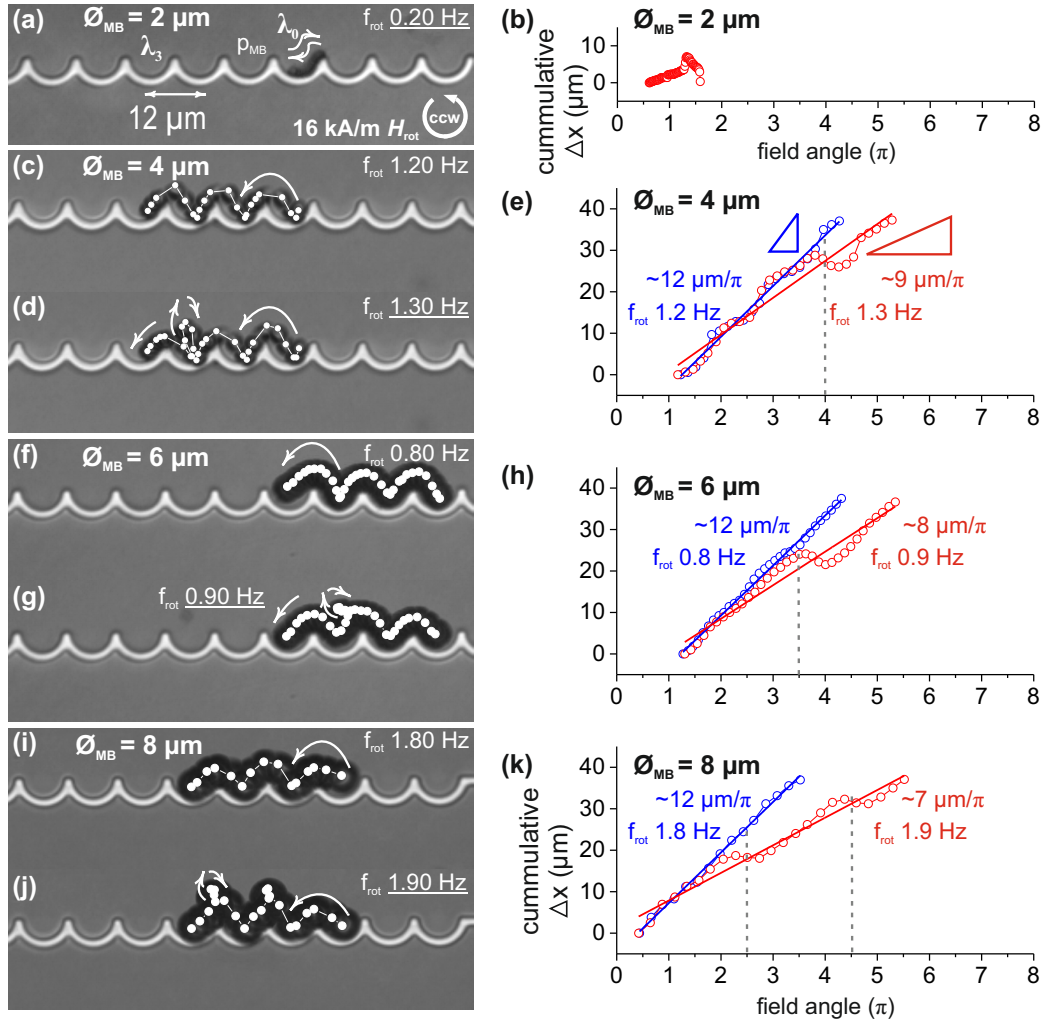
To characterize the effect of magnetic field gradient FG generating feature of the magnetic track MT, the behavior of same MBs is determined on the concave-pointed MT. Alternating pointed-tip and concave segments of this track, offering distinct movement patterns, can transport the MBs differently, depending on the size of particles. The track width and periodic distance are  $2 \mu\text{m}$  and  $12 \mu\text{m}$ .



**Figure 3.13:** Stray field gradients (MFM, a-c) and out-of-plane component of stray field gradients (MM, d-f), obtained at a height of 500 nm above the track, for selected  $H_{ext}$  orientations. Experimental images at the corresponding orientations of  $H_{ext}$ , show the motion trajectories of a  $2 \mu\text{m}$  (g-i),  $4 \mu\text{m}$  (j-l),  $6 \mu\text{m}$  (m-o) and  $8 \mu\text{m}$  bead (p-r). From the track position  $\lambda_0$ ,  $2 \mu\text{m}$  bead stopped at the concave segment while  $4 \mu\text{m}$ ,  $6 \mu\text{m}$  and  $8 \mu\text{m}$  beads reached the track position  $\lambda_1$ , following the moving field gradient.

### Movement Patterns on a Concave-pointed Track

MFM signals (Fig. 3.13 a-c) and out-of-plane component of stray magnetic field gradient FG (Fig. 3.13 d-f) on the convex-pointed track reveal the varying amplitudes of the FG at pointed and concave features needed for the actuation of a magnetic bead. Because of its small interactive volume, the  $2 \mu\text{m}$  is unable to follow the moving FG at the concave path, when the field changes from its horizontal to oblique orientation (Fig. 3.13 g-h). In effect, it moves back at the pointed region for the vertical field as shown in the Fig. 3.13 i. Likewise, the  $4 \mu\text{m}$  bead lags the FG maxima with the oblique orientation of the field (Fig. 3.13 k). It starts moving towards the next pointed segment, as soon as the vertical component of the rotating  $H_{ext}$  generates the stronger FG. The large  $6 \mu\text{m}$  particle completes its step motion, as shown in Fig. 3.13 m-o. Exemplary movement pattern of an  $8 \mu\text{m}$  bead demonstrates the start and end of a transport step as off-centered spatial positions, very similar to the  $4 \mu\text{m}$  particle, which is related to the much stronger stray magnetic field gradient across the track width (see the field gradient in Fig. 3.13 f). This is evident by the particles shifted positions on the track (Fig. 3.13 l and Fig. 3.13 r).



**Figure 3.14:** Recorded immobile response of a  $2 \mu\text{m}$  bead under ccw-rotating  $H_{ext}$  at a low  $f_{rot}$  (0.2 Hz). (a) A small cumulative  $\Delta x$  traveled and reaching back (b). (c)-(e)  $4 \mu\text{m}$  bead, (f)-(h)  $6 \mu\text{m}$  bead and (i)-(k)  $8 \mu\text{m}$  beads with their continuous and looping movements and plotted traveled paths. Plotted  $\Delta x$  position of moving MBs against field rotations are superimposed with slopes ( $\mu\text{m}/\pi$ ). High and low slopes represent the continuous and looping motion.

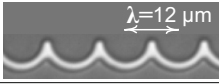
### Continuous and Looping Transport on a Concave-pointed Track

A  $2 \mu\text{m}$  particle having small magnetic volume is not movable through the concave region of the track and so it comes back around the tip following ccw-rotating  $H_{ext}$ . Exemplary motion trajectories of the  $4 \mu\text{m}$  in Fig. 3.14 c-d reveal its alternating hoping movement and resting on the track. These movement patterns are apparent as oscillations in the  $\Delta x$  curve in Fig. 3.14 e. Despite the remarkably different critical frequency  $f_{crit}$  of  $6 \mu\text{m}$  and  $8 \mu\text{m}$  beads, both show similar movement patterns for their continuous and looping motion (Fig. 3.14 f-g and Fig. 3.14 i-j). Noticeable differences in their response are as follows: The  $6 \mu\text{m}$  bead with a lower  $f_{crit}$  on the track takes rests at convex regions during its motion, which translates as slight oscillations in the cumulative  $\Delta x$  curves (Fig. 3.14 h). In comparison,  $8 \mu\text{m}$  bead with a higher  $f_{crit}$  skips

the resting position, evident with no oscillations in the  $\Delta x$  curves (Fig. 3.14 k). Moreover, fast loopings of  $8 \mu m$  bead appear as slight falls at field angles  $2.5\pi$  and  $4.5\pi$  in the  $\Delta x$  curve (Fig. 3.14 k), as compared to a deep dip for slow speed looping of the  $6 \mu m$  bead (Fig. 3.14 h).

### Microbead Velocities on a Concave-pointed Track

The small  $2 \mu m$  bead is not transportable, whereas large beads with different critical frequencies on the convex-pointed magnetic track show contrasting velocities. Microbead velocities below and above their  $f_{crit}$  are summarized in Tab. 3.4.

Microbead velocities on a concave-pointed track 	$\emptyset_{MB} = 2 \mu m$		$\emptyset_{MB} = 4 \mu m$		$\emptyset_{MB} = 6 \mu m$		$\emptyset_{MB} = 8 \mu m$	
	( $\mu m/s$ )	(Hz)	( $\mu m/s$ )	(Hz)	( $\mu m/s$ )	(Hz)	( $\mu m/s$ )	(Hz)
$v_{ave, x-dir}$ below $f_{crit}$ (continuous)	~0	0.2	~30	1.20	~19	0.80	~44	1.80
$v_{ave, x-dir}$ above $f_{crit}$ (looping)	-	-	~23	1.30	~14	0.90	~25	1.90

**Table 3.4:** Average velocities from the continuous and looping motion of MBs. MBs'  $v_{ave}$  reduces above their  $f_{crit}$ . The MB for highest  $v_{ave}$  is highlighted green.

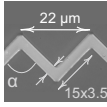
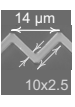
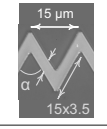

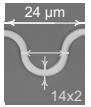
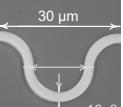
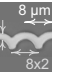
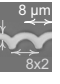

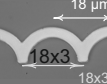




### Summary

Alternating concave and pointed magnetic features of a NiFe thin film magnetic track MT move the different size MBs differently. Distinct critical frequencies  $f_{crit}$  of MBs are determined as a result of their effective magnetic volume interacting with the moving stray field gradient FG. Small  $2 \mu m$  beads are not movable through the concave magnetic feature.  $4 \mu m$  beads move along the FG around pointed features, while they rest at concave segments of the MT. Large  $8 \mu m$  diameter bead moves with higher speeds, than  $4 \mu m$  and  $6 \mu m$  beads.

A  $4 \mu m$  diameter bead shows an almost twofold reduction in its  $f_{crit}$  on the concave-pointed track, against its  $f_{crit}$  on the convex track. Interestingly, the change in the  $f_{crit}$  for  $6 \mu m$  and  $8 \mu m$  beads is opposite, but with the similar factor. Compare in Tab. 3.3 and Tab. 3.4. We learn that the small (large) magnetic particles can be transported faster on round (pointed) magnetic features. A twofold increase or decrease in the speed of various magnetic particles is achievable with an optimized geometry of the track. Increased speed of large particles, resulting from the pointed magnetic features, have also been confirmed earlier over zigzag tracks (Sec. 3.4.2), compared to their low speeds on curvilinear tracks (Sec. 3.4.1).

### 3.4.5 MB Velocity Dependence on $H_{ext}$ Amplitude and Track Size

For a suitable combination of a magnetic MB with a magnetic track MT, the velocity  $v_{ave}$  of the MB is controllable by simply changing the rotational frequency of  $H_{ext}$ . Yet,  $v_{ave}$  can be improved by increasing the  $f_{crit}$  of the moving MB with a higher amplitude (80 kA/m) of  $H_{ext}$ , as shown in Tab. 3.5. However, the increased  $v_{ave}$  results only from a proper size combination of MB and MT. As an example, a  $2\ \mu\text{m}$  bead with small volume showed a twofold increased  $v_{ave}$  on small sized zigzag MTs, compared to almost no increment on large zigzag MTs. Overall, the enhancement in the transport velocity  $v_{ave}$  varies between approx.  $1.2\times$ - $2\times$  for the shown results.

Track type	Track size, l x w ( $\mu\text{m}$ )	Bead size $\varnothing_{MB}$ ( $\mu\text{m}$ )	$f_{rot}$ (Hz)	Ave. Vel. at 16 kA/m ( $\mu\text{m/s}$ )	Velocity increment at 80 kA/m	Track size, l x w ( $\mu\text{m}$ )	Bead size $\varnothing_{MB}$ ( $\mu\text{m}$ )	$f_{rot}$ (Hz)	Ave. Vel. at 16 kA/m ( $\mu\text{m/s}$ )	Velocity increment at 80 kA/m	
Zigzag $\alpha = \pi/2$		2	0.35	~14	~1x		2	0.55	~15	~2.1x	
		4	0.8	~29	~1.6x		4	1.6	~53	~1.6x	
		6	0.9	~33	~1.5x		6	1.5	~42	~1.5x	
		8	0.9	~33	~1.3x		8	1.3	~35	~1.4x	
	Zigzag $\alpha = \pi/3$		2	0.45	~12	~1.1x		2	1.8	~34	~1.8x
			4	1.2	~37	~1.2x		4	3.2	~68	~1.3x
			6	2.8	~80	~1.5x		6	5.2	~102	~1.08x
			8	2.0	~60	~1.5x		8	0.8	~16	~2.3x
Curvilinear track		2	0.2	~0	~0x		2	0.2	~0	~0x	
		4	0.6	~15	~2.4x		4	0.2	~0	~0x	
		6	0.4	~19	~1.4x		6	0.35	~13	~2x	
		8	0.9	~42	~1x		8	0.7	~27	~1.3x	
	Convex track		2	1.5	~24	~1.4x		2	1.5	~24	~1.4x
			4	2.7	~88	~1.1x		4	2.0	~30	~1.3x
			6	1.5	~48	~1.1x		6	0.6	~15	~1x
			8	1.5	~48	~1.4x		8	0.2	~3	~1x
Concave-pointed track		2	1.8	~42	~2x		2	3.9	~60	~1.5x	
		4	2.5	~60	~1.2x		4	6.0	~90	~1.2x	
		6	0.35	~8	~1.2x		6	2.2	~24	~1.3x	
		8	0.9	~22	~1.5x		8	0.7	~11	~1.5x	
		2	0.2	~0	~0x		2	1.7	~56	~1.6x	
		4	1.2	~28	~1.5x		4	1.2	~41	~1.2x	
		6	0.9	~21	~1.7x		6	0.4	~19	~1.6x	
		8	1.8	~44	~1.6x		8	0.6	~19	~1.3x	
	2	0.2	~0	~0x		2	0.2	~0	~0x		
	4	0.2	~7	~1.1x		4	0.2	~7	~1.1x		
	6	0.55	~13	~2x		6	0.55	~13	~2x		
	8	0.7	~21	~2x		8	0.7	~21	~2x		

**Table 3.5:** Increased  $v_{ave}$  of individual MBs at the higher strength  $H_{ext}$  on various NiFe tracks. The MB sizes for highest  $v_{ave}$  are highlighted green. The movement was executed at the upper side of tracks.

## Discussion

Using the geometry of micromagnetic features on soft ferromagnetic tracks, magnetic particles can be moved along the homogeneously moving in-plane external magnetic field. The varying magnetic field gradients at round, flat and pointed features of Permalloy tracks enable a controlled directed motion of particles for a continuously rotating  $H_{ext}$ . Based on a simple externally rotating field, this MB manipulation scheme facilitates the different speeds of the particles depending on their size and type of magnetic tracks, without the programmed external field sequences.

**Zigzag Tracks:** Since microbeads move along the changing positions of maximum field gradient (e.g. tips in zigzag tracks), the MBs with large magnetic volume move faster due to high magnetophoretic mobility MPM (see eq. 1.19). The beads, being too small relative to the periodic length  $\lambda$  of the track, move slower due to small magnetic volume. Using the size relation between the magnetic bead (diameter  $\varnothing_{MB}$ ) and the magnetic track (periodic length  $\lambda$ ), a threshold limit of MPM is determined. On the zigzag tracks, MPM is maximum, when the bead diameter is around half the size of the periodic length of the track ( $\varnothing_{MB} = 0.5 \pm 0.1 \times \lambda$ ). As an example, the  $6 \mu m$  bead shows higher velocity  $v_{ave}$  along zigzag tracks, as highlighted green in Tab. 3.5. The lower  $v_{ave}$  of other beads reflects their lower MPM, because of either too small ( $\varnothing_{MB} \ll 0.5 \times \lambda$  for  $\varnothing_{MB} = 2 \mu m$  and  $4 \mu m$ ) or too large ( $\varnothing_{MB} \gg 0.5 \times \lambda$  for  $\varnothing_{MB} = 8 \mu m$ ) size of the magnetic bead.

**Convex and Concave Tracks:** Excessively large magnetic particles, together with the widely distributed magnetic field gradient (FG) maxima on round magnetic tracks, will move slower. For the directed motion, the particle must be small enough to follow just the forward moving FG maxima. The particle size equaling to the periodic length of the track causes an intermittent motion due to the effect of backward FG maxima. This results in a reduced MPM. For the high MPM, the optimum size of the magnetic particle with the convex and concave tracks is confirmed by the fast moving  $2 \mu m$  and  $4 \mu m$  particles ( $\varnothing_{MB} \approx 0.25 \times \lambda$  and  $\approx 0.50 \times \lambda$ ), highlighted green in Tab. 3.5. In contrast, large  $6 \mu m$  and  $8 \mu m$  particles move slow ( $\varnothing_{MB} \approx 0.75 \times \lambda$  and  $\approx 1.0 \times \lambda$ ). Note the effect of track shape for a favorable match with the particle size.

The same magnetic particle, showing  $\approx 2 \times$  increase (decrease) in its speed during its motion on the concave (convex) track, indicates the mutual contribution of the FG generating magnetic feature of the MT and the size of particle. The  $2 \mu m$  diameter bead moved  $\approx 2 \times$  faster on the convex track, whereas the  $4 \mu m$  bead moved  $\approx 2 \times$  faster on the concave MT for the applied field  $H_{ext} = 16$  kA/m, as highlighted blue in Tab. 3.5. On the high magnetic field  $H_{ext} = 80$  kA/m, the larger improvement in the velocity of both beads occurred on the concave tracks (indicated blue in Tab. 3.5), which confirms the deciding role of structure geometry once again.

**Curvilinear Tracks:** Magnetic tracks with a large period length  $\lambda$  have the wide distanced positions of field gradient maxima on the track. Consequently, the magnetic bead has to travel longer distance along the in-plane rotating  $H_{ext}$  to follow the next FG maxima. This causes a larger phase lag and thus a decreased magnetic force



on the moving bead. Meanwhile, the hydrodynamic drag force prevails, resulting in the decreased magnetophoretic mobility MPM of the beads (see eq. 1.19). The reduced magnetic field gradient due to an inappropriate shape (e.g. concave side of the curvilinear track) is another factor to the diminishing MPM. Therefore, small magnetic particles cannot be transported ( $v_{ave} \approx 0$ , shown in Tab. 3.5) on large size curvilinear tracks, despite the higher amplitude of  $H_{ext}$ . Even, the large particles move considerably slower which indicates the size restraint of magnetic structure.

To conclude, the following contributions define the transport velocity  $v_{ave}$  of microbeads MBs: Firstly, at a medium strength  $H_{ext}$  (16 kA/m), the  $v_{ave}$  of a moving bead is primarily given by the size and shape of the magnetic track. Secondly, if the bead is already moving fast enough and signifies a negligible increase in its  $v_{ave}$  at the higher strength  $H_{ext}$  (80 kA/m), then that means the magnetization of the MB is close to its saturation. This response is mostly true for various magnetic particles and magnetic tracks, shown in Tab. 3.5. A proper design of the magnetic structure enables the directed transport, even at lower strength (Appendix-A.4 - Appendix-A.7). The transport speed can be improved with the increased magnetic field gradient up to the saturation limit of the volume magnetization of the particle in motion. However, if the geometry of the track does not allow the particle movement, then the high strength  $H_{ext}$  does not help either. See the particle response on the simple disk and ring structure in Sec. 3.3.

We learn that, at the first place, it is not the higher strength of  $H_{ext}$  or higher field gradient which facilitates the maximum achievable velocity  $v_{ave}$ , but it is the proper matching between the geometry of the magnetic track and the size of the magnetic particle. Unlike the sudden drop in the particle velocity at the critical frequency due to a large difference in the sizes of particle and the particle moving structure (Sec. 3.4), an optimum size combination enables a quasi linear decrease in MB  $v_{ave}$ , indicating the sorting opportunities for mixed particle distributions (see Appendix-A.3).

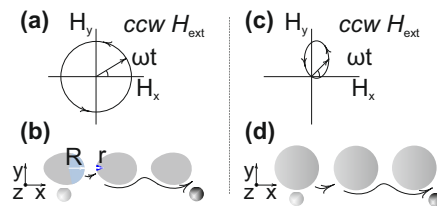
**Summary** Superparamagnetic microbeads are transported along the moving inhomogeneous stray field gradient FG at the magnetic features of NiFe magnetic tracks using a homogeneously rotating in-plane magnetic field  $H_{ext}$ . Transport speeds of single MBs are controllable by choosing between the continuous and looping movements with a change in the rotational frequency  $f_{rot}$  of  $H_{ext}$ . At a fixed amplitude of the rotating  $H_{ext}$ , mixed MBs exhibit various speeds due to their size dependent distinct critical frequency  $f_{crit}$  over a track. One type of magnetic beads can be moved regular, while the other type can be trapped, e.g. in the concave segments of the track, at a constant  $f_{rot}$  of  $H_{ext}$ . The appropriate size and shape of the magnetic track is determined for the ultimate speed of different size particles. Achieving a  $2\times$  different average velocity  $v_{ave}$  of different size particles during their continuous motion and a  $2\times$  reduction in  $v_{ave}$  through the periodic looping motion, makes this manipulation scheme applicable for particle filtering. Depending on the application, the choice of a magnetic pathway for the fast transport of single particles and the filtering of mixed populations of particles, is simplified on a magnetic microchip.

# Chapter 4

## Microbead Motion on 1-D Magnetic Arrays

With the circulating motion of a single magnetic microbead MB around an individual magnetic structure MS, the directed motion of the MB can be achieved by reproducing its movement patterns over the periodic MSs. These flexible movement patterns of the MB on periodic MS provide the base for a selectable lateral motion along the magnetic arrays MAs, in contrast to the MB moving along a fixed path of a magnetic track. However, to transport of the MB on a MA, it must be movable onto the next MS. For a directional bias in the MB movement, a spatial and/or dynamic asymmetry is required in the manipulation system.

This chapter deals with the controlled directional motion of single MBs based on MS-shape given spatial asymmetry (internal and fixed) and applied magnetic field given dynamic asymmetry (external and tuneable). In the first approach, egg-shaped MS are positioned with their opposite radii of curvature facing each other. With the different curvatures at the structures' interface, the asymmetric stray fields gradients form, which guide the moving MB in the preferred direction under a rotating  $H_{ext}$  (Fig. 4.1 a-b). A network of MAs can transport the MBs population towards a target location on the chip in a parallel manner. The second transport strategy involves the MB motion on a disk array using off-centered elliptical rotating  $H_{ext}$  (Fig. 4.1 c-d). The asymmetrically changing stray field gradient at the disks interface interrupts the MB circulation and causes its hopping motion to the next disk. Disk arrays in a 2-D distribution can move the MB in multiple directions and sort multiple size MBs.

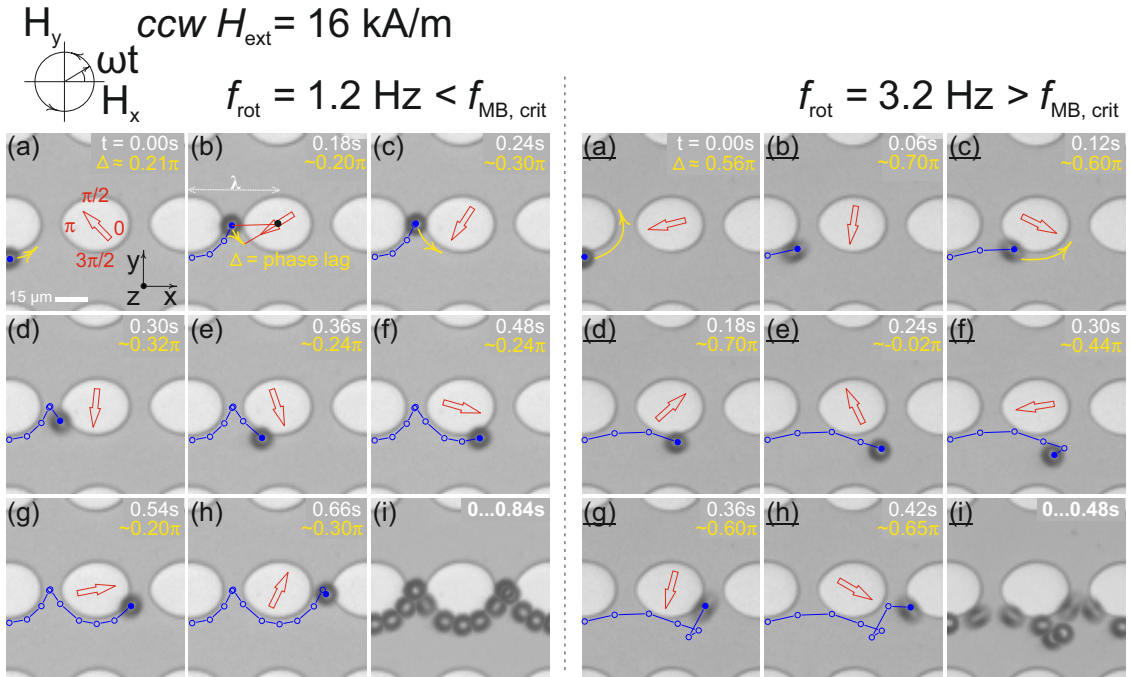


**Figure 4.1:** (a) Homogenous  $H_{ext}$  moving a MB on an asymmetric magnetic array MA. (b) Asymmetric  $H_{ext}$  moving a MB on a symmetric MA.

## 4.1 1-D Motion based on Structures' Asymmetry

The idea to employ FeCoSiB egg-shaped structure is inspired by the microbead's circulating motion on disks with different radii. The moving bead exhibits higher critical frequency  $f_{crit}$  on the disk with small radius than with the large radius (see Sec. 3.3). Experiments on egg-arrays confirm the directed movement of single MBs from the large radius of curvature of one element to the small radius of curvature of the next element under the homogeneously rotating  $H_{ext}$  with a fixed rotational frequency  $f_{rot}$ . The alternating rotational and hopping motion of the bead around the egg-shaped structures translate to a controlled transport on a magnetic array. The time averaged velocity  $v_{ave}$  of the bead can be directly increased with the increasing  $f_{rot}$  of  $H_{ext}$ , up to the  $f_{crit}$  of the bead in motion. At a higher  $f_{rot}$  looping motion occurs.

### 4.1.1 1-D Motion on an Array of Asymmetric Structures



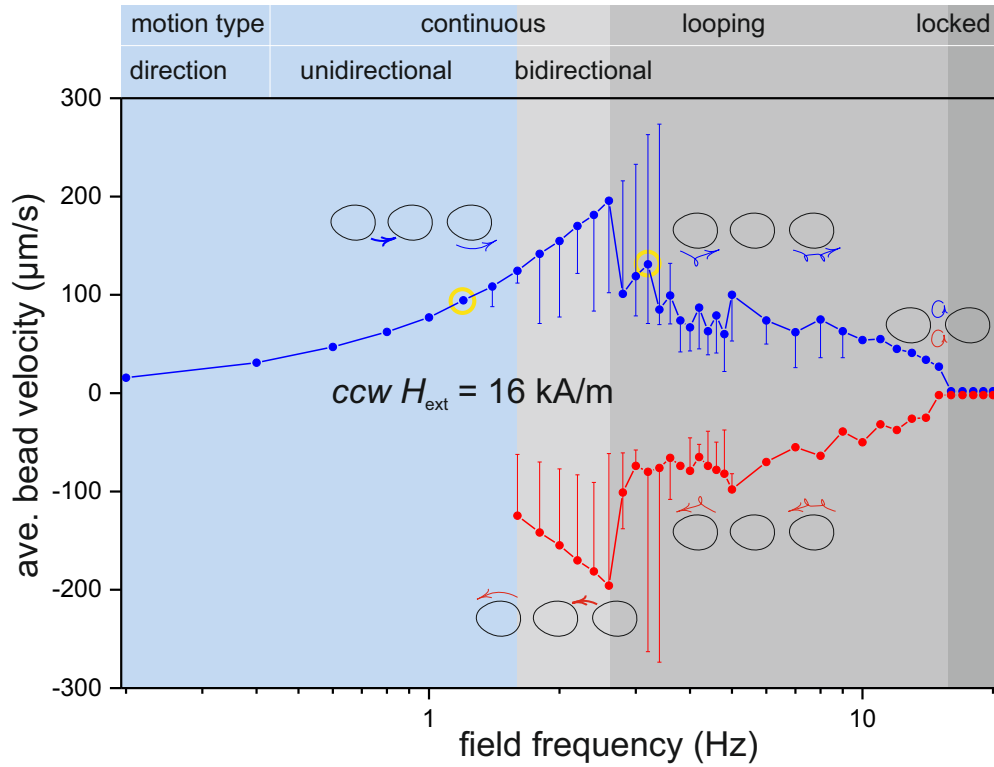
**Figure 4.2:** Transport of an  $8 \mu\text{m}$  bead on  $50 \text{ nm}$  thick FeCoSiB magnetic structures MSs below ( $f_{rot} = 1.2 \text{ Hz}$ ) and above ( $f_{rot} = 3.2 \text{ Hz}$ ) the  $f_{crit}$  of the bead moving along the ccw-rotating  $H_{ext}$  with a fixed amplitude of  $16 \text{ kA/m}$ . (a) Small phase lag  $\Delta$  during the bead rotation. (b)-(c)  $\Delta$  increases due to the competing stray field gradient at the structure's interface. (d) The bead moves to the next MS for  $H_{ext}$  orientation being perpendicular to the long axis of the egg.  $\Delta$  decreases and increases for the respective rotational motion (e)-(g) and the MB stays (h). (i) Full trajectory of the motion. (a)-(c) Direct hopping due to a large  $\Delta$  for high  $f_{rot} = 3.2 \text{ Hz}$ . (d) Detachment of the bead at the larger  $\Delta$ , followed by a looping in motion (e)-(g) and the MB hopping to the next MS (h). (i) Record of the looping motion.

To unveil the features of the bead transport, the exemplary response of a single  $8\ \mu\text{m}$  diameter bead is analyzed for its continuous and looping motion. The bead starting its rotation at the short-axis of an egg, following the ccw-rotating field (fixed amplitude  $H_{ext} = 16\ \text{kA/m}$  and  $f_{rot} = 1.2\ \text{Hz}$ ), initially exhibits a small phase lag ( $\Delta$ ) until it reaches the structures' interface (Fig. 4.2 a-b). Since the bead is moved with a low  $f_{rot}$ , it does not directly hop to the next MS but rests at the interface, which causes an increased  $\Delta$  as shown in Fig. 4.2 c. Now, with its stable position already at the small radius of curvature, the bead starts moving around the next MS (Fig. 4.2 d) to catch the moving stray field gradient, having its orientation perpendicular to the long axis of the MS (see MFM images on  $50\ \text{nm}$  thick FeCoSiB patterns in Appendix-B.1). The bead continues the circulating motion around the MS with relatively lower  $\Delta$  (Fig. 4.2 e-g), until it reaches the next interface where it hops again to recover the increased angular position of a rotating  $H_{ext}$  (Fig. 4.2 h). The full history of its travel in Fig. 4.2 i shows its controlled transport, mainly composed of the circulating motion. One full rotation of  $H_{ext}$  ( $0 - 2\pi$ ) results in an equal bead circulation, i.e. two periods of distance traveled along the array. See appendix-E.1.2 Movie 4.1.

For the bead motion above its critical frequency  $f_{crit}$ , a looping accompanied transport is observed. Yet, the bead is able to follow the fast changing rotations of  $H_{ext}$ , but with a large phase lag  $\Delta$  as shown in Fig. 4.2 a-c. Now, the bead hops directly to the next structure. With increased  $\Delta$  and being far behind the field angular position (Fig. 4.2 d), it detaches from the structure (Fig. 4.2 e) and it loops (Fig. 4.2 f). Despite the bead has reached the structure perimeter after a looping, it still lags largely behind the field position (Fig. 4.2 g-h) for a high  $f_{rot} = 3.2\ \text{Hz}$ . The record of this high speed looping transport is presented in Fig. 4.2 i. See appendix-E.1.2 Movie 4.2. A biased motion of differently positioned MBs is shown in appendix-E.1.2 Movie 4.3.

### 4.1.2 MB Velocity on an Array of Asymmetric Structures

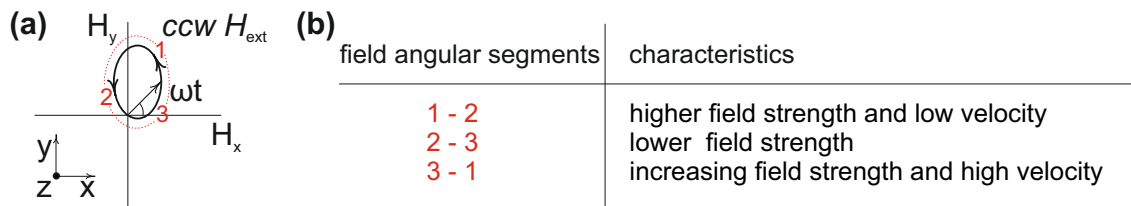
An overall behavior of  $8\ \mu\text{m}$  beads ensemble, plotted in Fig. 4.3 as bead velocity  $v_{ave}$  vs. field frequency  $f_{rot}$  reveals various regimes of motion. MBs  $v_{ave}$  increases linearly with the increment in  $f_{rot}$  until the offset of  $f_{rot}$  for the unidirectional motion. On increasing the  $f_{rot}$  of  $H_{ext}$ , single MBs were observed to move also in the opposite direction, due to their starting position at other side of the array. At higher  $f_{rot}$ , the directed motion occurs around the shorter axes of egg structures, due to the fast changing  $H_{ext}$ . In other words, the MB motion is not decided by the dissimilar radius of curvature at structures' interface which might cause the MB motion also in reverse direction, depending on its initial position, as indicated by the negative MB's  $v_{ave}$  in Fig. 4.3. With further increment in  $f_{rot}$ , the MB continuous motion changes to looping, causing a sudden drop in  $v_{ave}$ . Numerous loopings cause a further reduction in MB's  $v_{ave}$ . Finally, for the high  $f_{rot}$  of  $H_{ext}$ , the MB is not movable around the structures and thus exhibit self-orbital or locked motion at the structure's interface. Experiments performed over a  $f_{rot}$  range differentiate the MB's dynamic response from a controlled linear 1-D transport at low  $f_{rot}$  to a locked motion at high  $f_{rot}$  of  $H_{ext}$ . Error bars represent the different  $v_{ave}$  of single MBs due to their different susceptibilities.



**Figure 4.3:** Average transport velocity  $v_{ave}$  of single moving  $8 \mu\text{m}$  MBs for a rotational field frequency  $f_{rot}$  range under a ccw-rotating  $H_{ext}$  with a fixed amplitude of  $16 \text{ kA/m}$ . A linear increase in  $v_{ave}$  for the lower  $f_{rot}$  and locked motion for the high  $f_{rot}$  are determined. Various regimes of motion are indicated. Red color designates the motion in opposite direction. Error bars represent the variation in the magnetic content within single MBs.

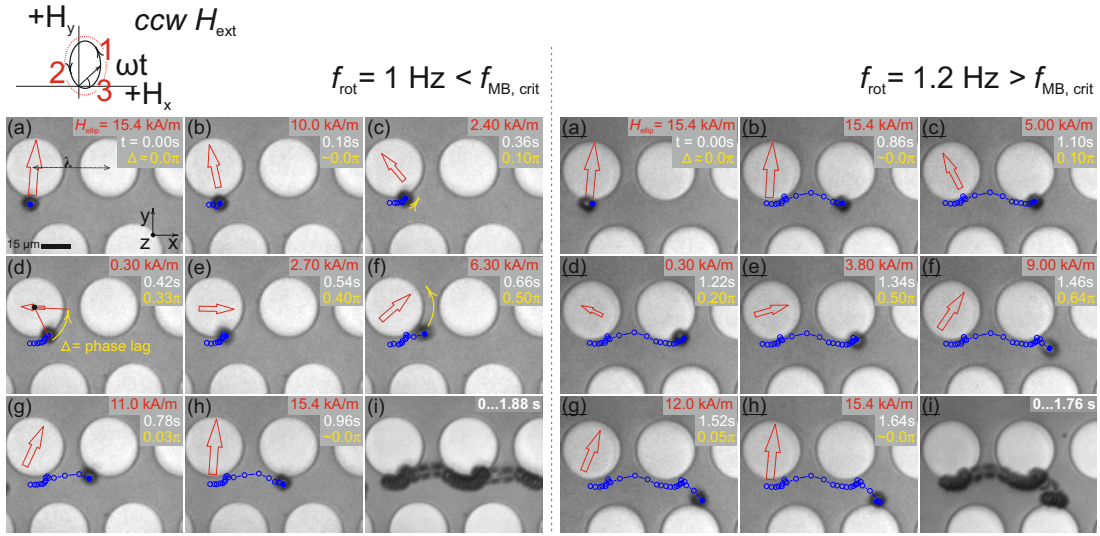
## 4.2 Directed Motion based on Applied Field's Asymmetry

In contrast to the predetermined directed motion by the shape asymmetry of magnetic structures, the transport of individual MBs on symmetric MSs is enabled by the asymmetry of an off-centred elliptically rotating magnetic field ( $H_{ext}$ ). An exemplary rotation of the field is sketched in Fig. 4.4. By dividing into angular segments, the characteristics of in-plane rotating  $H_{ext}$  are specified for the MB motion along a disk array.



**Figure 4.4:** (a) The rotation of an elliptical field divided into angular segments. (b) Corresponding field characteristics.

## 4.2.1 Directed Motion on an Array of Symmetric Structures



**Figure 4.5:** Directed motion of an  $8\ \mu\text{m}$  bead along a  $50\ \text{nm}$  thick  $\text{FeCoSiB}$  disk array with  $H_{\text{ext}}$  ccw-rotating below ( $f_{\text{rot}} = 1\ \text{Hz}$ ) and above the critical frequency ( $f_{\text{rot}} = 1.2\ \text{Hz}$ ) of the bead. (a)-(c) Rotational motion of the particle (d) Reducing strength of  $H_{\text{ext}}$  causes an angular stop in the bead motion. (e) Still no motion and the bead is lagging largely behind the field position. (f) With a larger phase lag  $\Delta$ , the bead is attracted towards the closely moving re-magnetized state of next disk. The bead reaches the next disk after its hopping motion (g) and continues its slow circulating motion (h). (i) Full record of the particle transport. At a slightly higher  $f_{\text{rot}}$  of  $H_{\text{ext}}$ , a regular transport step (a)-(b) occurs, followed by the slow circulating motion (c) and a stop in motion before hopping (d). Detachment from the disk at increased  $\Delta$  (f) and attraction of the bead towards the neighboring disk is shown (g). (h) Rotational motion in opposite direction. (i) Full trajectory of motion.

The experimental results of an  $8\ \mu\text{m}$  bead moving below and above its critical frequency  $f_{\text{crit}}$  with an elliptically rotating field are presented in Fig. 4.5. The bead starts its rotation around the element following the high field and low velocity segment of the elliptical  $H_{\text{ext}}$  as shown in Fig. 4.5 a-c. With no further rotational motion of the bead at low strength  $H_{\text{ext}}$  (Fig. 4.5 d), a large  $\Delta$  between the angular positions of the bead and field occurs. The resulting angular stop in bead motion exists throughout the low field segment of the rotating  $H_{\text{ext}}$  (Fig. 4.5 e). The bead experiencing an already increased  $\Delta$  fails to follow the moving  $H_{\text{ext}}$  and hence it detaches from the disk perimeter (Fig. 4.5 f). Meanwhile,  $H_{\text{ext}}$  segment with the increasing strength re-magnetizes the magnetic disks. The polarized edge of the next disk, moving towards the bead resting position, attracts the bead and hence hopping occurs (Fig. 4.5 g). After the hopping, the bead undergoes rotational motion again at its initial position on the next disk (Fig. 4.5 h). The alternating slow speed circulating and fast hopping motion of the single MB lead to an effective 1-D transport on the disk array.

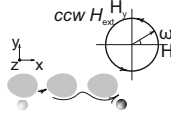
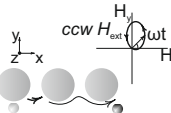
When the rotational frequency of the elliptical  $H_{\text{ext}}$  is slightly increased above the critical frequency of the bead in motion, the hopping motion of the particle occasionally

fails. Exemplary results at  $f_{rot} = 1.2$  Hz in Fig. 4.5 a-b show the bead regular movement over the first period, followed by the slow rotation (Fig. 4.5 c-d) and the angular stop (Fig. 4.5 e) during its travel over the second period. Because the hopping motion happens at a short time frame of the fast rotating  $H_{ext}$ , this time frame becomes even shorter for an increased  $f_{rot}$ . Unable to hop onto the next disk (Fig. 4.5 f), the bead is instead attracted by the stray fields from a disk on the adjacent array (Fig. 4.5 g). Afterwards, the bead continues its nonlinear motion in the opposite direction (not shown in Fig. 4.5)

## Discussion and Summary

Individual microbeads can be moved along the in-plane rotating  $H_{ext}$  on the periodic magnetic structures MSs. Driven with a fixed rotational frequency  $f_{rot}$  and amplitude of  $H_{ext}$ , the control in directed motion is also directly dependent on the size and distance among MSs. The presented results represent the optimum geometric parameters. Larger egg-shaped MSs cause a reduced critical frequency and thus the lower speed, while on small MSs, MBs are not transportable due to the reduced effect of dissimilar radii at the structures' interface. Periodic MSs with the distance equal to the MB's size create a directional bias in MB motion, but for lower  $f_{rot}$ . At higher  $f_{rot}$ , a spontaneous reverse motion of MBs occurs, disrupting the inherent directionality of MB motion. To maintain the directed motion at high frequency of  $H_{ext}$ , improvements in the shape and distance of asymmetric MSs are needed. Disk arrays offer a bigger room for MB manipulation due to the symmetry of disk-shaped MSs together with the applied  $H_{ext}$  as a flexible control parameter. Size and distance between MSs likely define the sorting potential of different MBs.

In short, the directed motion of single beads is possible on magnetic arrays, either by exploiting the shape of MSs with a homogeneous in-plane rotating  $H_{ext}$ , or by using an off-centred elliptical rotating  $H_{ext}$  on symmetric MSs. The pros and cons of both approaches are summarized in Tab. 4.1.

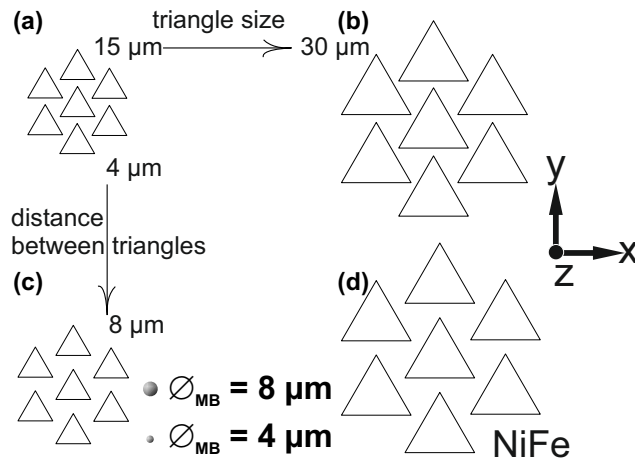
Transport of 8 $\mu\text{m}$ MB on arrays of sym. and asym. magnetic patterns	Flexibility in manipulation	Achievable ave. velocity for continuous motion ( $\mu\text{m/s}$ )	Direction of motion	Advantages	Limitations	Improvement possibilities
	low, due to the fixed asymmetry of magnetic patterns	high, >100 $\mu\text{m/s}$ , due to a continuous path of circulating motion	unidirectional	simple scheme for 1-D transport, no dynamic tuning of applied field required, higher transport velocities	spontaneous reverse motion occurs at high frequencies, MB motion and sorting on 2-D patterns is difficult	structures' shape and interstructure gap optimization to avoid the reverse motion
	high, due to the tunable asymmetry of magnetic field	low, < 50 $\mu\text{m/s}$ , due to a certain time required for the controlled hopping on the next structure	bidirectional	possibilities of multidirectional motion and microbeads sorting	low transport velocities, complex magnetic fields	optimization of applied field and structure for better speed and sorting of multiple MB on 2-D structures

**Table 4.1:** 1-D transport of single 8  $\mu\text{m}$  MBs along egg-shaped and disk arrays under an in-plane rotating  $H_{ext}$  with the respective symmetric and asymmetric order.

# Chapter 5

## 2-D Movement of Microbeads on a Trisymmetric Magnetic Surface

Periodic magnetic structures open paths for the lateral motion of magnetic microbeads on the surface of a microchip. In contrast to the MB motion, limited along magnetic tracks and 1-dimensional arrays, the trisymmetric arrangement of discrete MSs, permits the MB transport to an arbitrary location on the chip. The manipulation is achieved with precise movement steps by switching the position of stray magnetic field gradient on soft MSs with alternative sequences of an in-plane external magnetic field. The exemplary results of the MBs' two-way directed motion are shown in our published work (Ref. 64). With different sizes single MBs can be moved selectively due to their differently confined positions on the MSs. However, the controlled separation of MBs is challenging, because of the closely spaced FG on a hexagonal magnetic surface. Therefore, a thorough understanding of motion at a single bead and population level, is required for MSs with different sizes and interstructure distances. Manipulating the magnetic FG with varying order and amplitude of  $H_{ext}$  can reveal the underlying paths of motion and separation for the MBs with different diameters on a 2-D patterned magnetic surface.

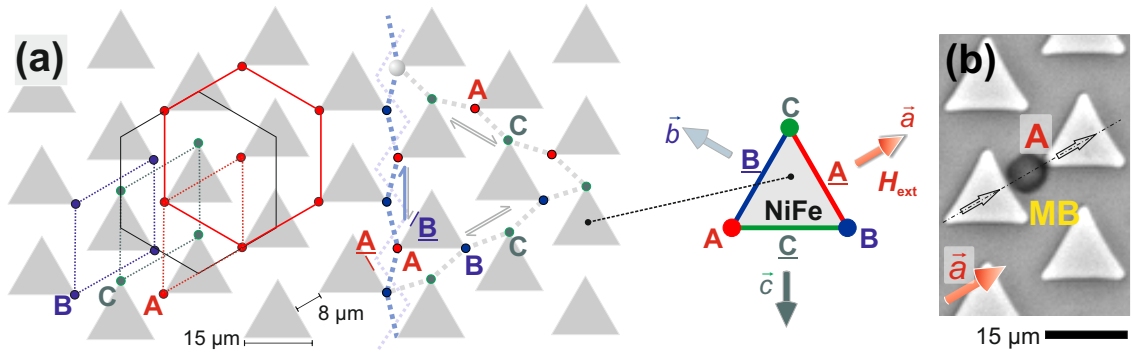


**Figure 5.1:** Geometric configurations of magnetic structures and microbeads.



## 5.1 Trisymmetric Magnetic Patterns

The hexagonal arrangement of triangular patterns with an interface between them provides trilateral paths for the transport of microbeads on a chip. A schematic of the magnetically patterned surface is shown in Fig. 5.2, where point lattices highlight the symmetrically spaced corners of triangles for the microbead positioning at A, B and C under the principle directions ( $\vec{a}$ ,  $\vec{b}$  and  $\vec{c}$ ) of an in-plane magnetic field. The edges opposite to the corresponding corners in the field direction are indicated as A, B and C. A micrograph in Fig. 5.2b shows an  $8\ \mu\text{m}$  MB positioned at the vertex A of a  $50\ \text{nm}$  thin NiFe pattern for the  $\vec{a}$  direction of the externally applied magnetic field with an amplitude of  $16\ \text{kA/m}$ .



**Figure 5.2:** (a) Schematic of  $50\ \text{nm}$  thin discrete NiFe triangle patterns in a hexagonal arrangement. Linking left A, right B and top C vertices of triangles with a four point lattice illustrates the trilateral symmetric sites for the microbead positioning near the opposite edges A, B and C. Applied magnetic field along principle directions  $\vec{a}$ ,  $\vec{b}$  and  $\vec{c}$  activates the corresponding vertex and edge. (b) An optical image showing an  $8\ \mu\text{m}$  MB positioned at the vertex A for the  $\vec{a}$  direction of  $H_{ext}$  with an amplitude of  $16\ \text{kA/m}$ . Reproduced from Ref. 64 with permission © 2018 Wiley-VCH.

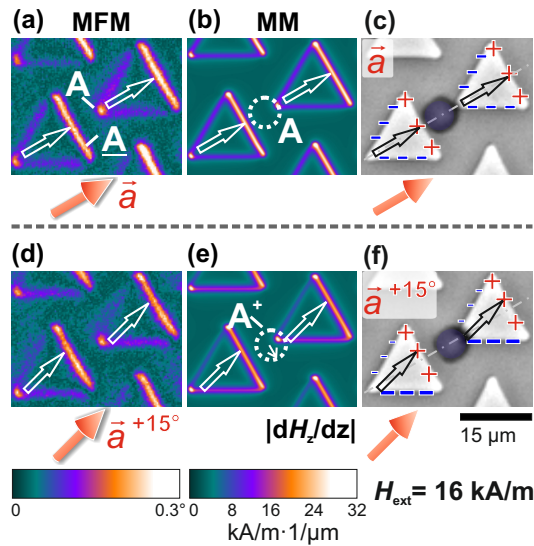
### 5.1.1 Stray Magnetic Fields on Triangular Patterns

To transport the microbeads, a single step movement response of a single bead, defined by its stable position at the structures interface, is crucial to understand. A field amplitude  $H_{ext} = 16\ \text{kA/m}$  magnetizes the NiFe structure and generates the stray magnetic field gradient to confine the bead for its subsequent motion. An asymmetry in the direction of  $H_{ext}$  with respect to an array of magnetic elements changes the spatial distribution of FG around magnetic elements. This results in a slightly shifted position of the bead, which ultimately decides its direction of translational motion. Exemplary confined positions of a bead under the symmetric ( $\vec{a}$ ) and asymmetric ( $\vec{a}^{+15^\circ}$ ) orientation of  $H_{ext}$  are shown in Fig. 5.3.

On applying a symmetric field  $\vec{a}$ , the symmetric stray field gradients around triangles are determined using MFM (Fig. 5.3 a). The out-of-plane component of stray field gradient  $\left| \frac{dH_{s,z}}{dz} \right|$  calculated by MM simulations reveals the higher field gradient FG at

the tip and edge of triangles, while the lower FG along the edges, adjacent to the tip as shown in (Fig. 5.3 b). An experimental image in Fig. 5.3 c shows the resultant confinement of an  $8\ \mu\text{m}$  particle on the field gradient landscape along the principle direction  $\vec{a}$  of  $H_{\text{ext}}$ .

For an asymmetric field orientation ( $\vec{a}^{+15^\circ}$ ), the distribution of stray field gradient (FG) is shifted across the magnetic structures as shown in Fig. 5.3 d and Fig. 5.3 e. Now, the stronger FG at the base of triangles and the weaker FG at the other adjacent edge is attained. The effect of the asymmetric field is also noticeable as the reduced FG along opposite edge  $\underline{A}$ . This spatial adjustment of the magnetic FG directly affects the bead equilibrium position as shown in Fig. 5.3 f. Now, the bead is slightly shifted onto a triangle due to an asymmetric field  $\vec{a}^{+15^\circ}$ . Overall, no change occurs at the vertex A of the magnetic elements, which explains why the bead shifts its position just around the vertex. The dependence of bead position on the changing amplitude of  $H_{\text{ext}}$  is discussed in Appendix-C.1.



**Figure 5.3:** (a) MFM measurements performed on NiFe patterns under a symmetric applied field  $\vec{a}$ . (b) Out-of-plane component of symmetric field gradient FG, with a higher magnitude at the tip A and opposite edge  $\underline{A}$  and lower at the adjacent edges, calculated by MM simulations at equal field conditions. (c) Experimental image of an  $8\ \mu\text{m}$  bead having its equilibrium position between A and  $\underline{A}$ . (d) Shifted stray field distribution for the asymmetric applied field  $\vec{a}^{+15^\circ}$ . (e) Shifted FG with an increased magnitude at the base and a decreased magnitude at the  $\underline{A}$  edge. (f) The resultant shift in the microbead position. The stray field gradient are determined at  $500\ \text{nm}$  above the magnetic surface for  $H_{\text{ext}}\ 16\ \text{kA/m}$ . Reproduced from Ref. 64 with permission © 2018 Wiley-VCH.

### 5.1.2 Bidirectional Motion of Microbeads

A magnetic bead can be moved from one to the next element by inverting the stray field gradient landscape on switching the direction of magnetic field. After a

lateral movement step, the bead attains the equilibrium position again. Following the inverting FG over magnetic patterns, the bead movement results in a directed transport on the chip. Fig. 5.4 demonstrates the movement patterns of single beads with  $\varnothing_{MB} = 8 \mu m$  and  $4 \mu m$  under the symmetrically and asymmetrically changing  $H_{ext}$  with a fixed strength (16 kA/m) and switching frequency (5 Hz).

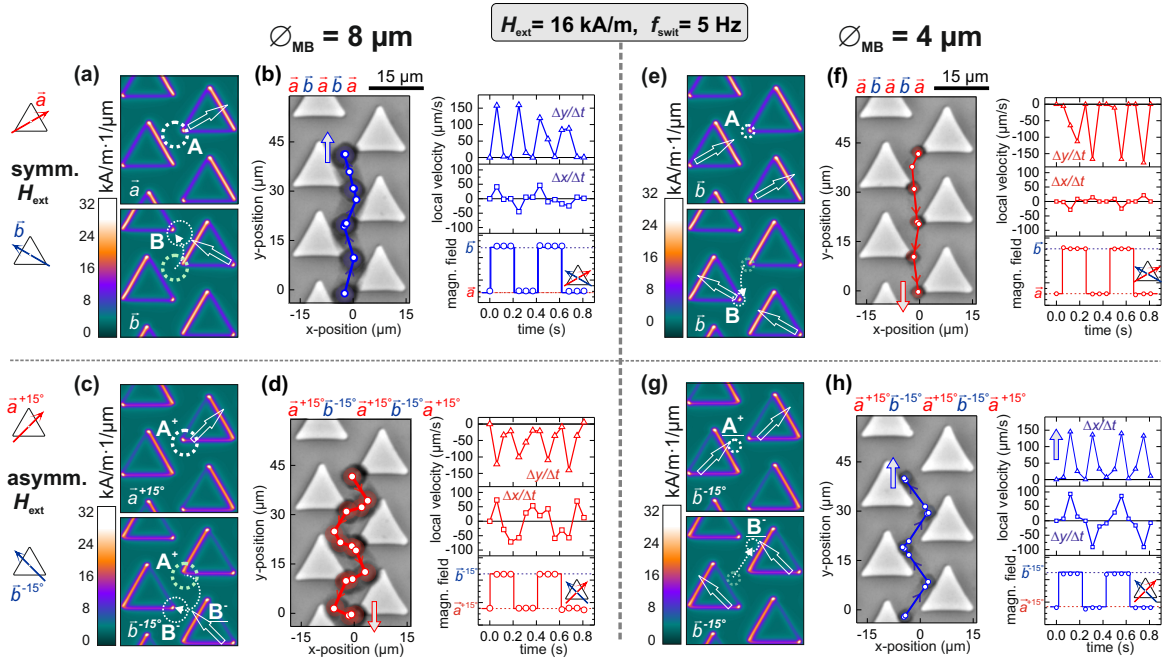
With a large magnetic volume, the  $8 \mu m$  bead finds its equilibrium position between the vertex A and edge A of two elements for the initial field condition  $\vec{a}$ . After the field is switched to  $\vec{b}$  as shown in Fig. 5.4 a, the inverted magnetic field gradient along the edge B moves the bead forward from its initial position at vertex A to its successive position at vertex B. For the field condition  $\vec{b}$ , the calculated FG at the edge A now has a decreased magnitude, which clarifies why the particle did not move backward. Fig. 5.4 b shows the forward movement steps of the  $8 \mu m$  bead resulting from the alternative inverting FG with  $H_{ext}$  changing between  $\vec{a}$  and  $\vec{b}$ . The continuous distribution of the FG along the edges A and B serves as a trail for the rectilinear motion, whereas the vertexes A and B are stable sites for the moving particle. The attraction of the magnetic particle towards the next vertex occurs only through inverted FG after a change in the field direction. Starting points of forward movement steps are indicated as long spikes on the plot for its vertical velocity at square wave magnetic field  $H_{ext}$  switching between  $\vec{a}$  and  $\vec{b}$ , as shown in Fig. 5.4 b.

For the initial state of the asymmetric field  $\vec{a}^{+15^\circ}$ , the already shifted position of the  $8 \mu m$  bead onto the vertex  $A^+$  now lies close to the magnetic field gradient FG at the edge B for the switched field state  $\vec{b}^{-15^\circ}$  as illustrated on the asymmetric FG maps in Fig. 5.4 c. Thus, the particle initially attracts towards the edge B, followed by its movement towards the vertex  $B^-$ , which results in a curling path of motion. After the field is switched to  $\vec{b}^{-15^\circ}$ , the increased FG at the base together with the FG at edge B of the triangle below attracts the bead backward from its initial shifted position  $A^+$  to its next shifted position  $B^-$ . The experimental image in Fig. 5.4 d shows the resulting curling movement patterns and velocity peaks in both vertical and horizontal direction which exemplifies the influential FG from the edge B of the neighboring structure for the initiation of backward curling motion.  $H_{ext}$  changing between  $\vec{a}^{+15^\circ}$  and  $\vec{b}^{-15^\circ}$  moves the  $8 \mu m$  bead backward in an indirect manner, involving three structures, in contrast to its direct forward movement through two structures with  $H_{ext}$  changing between  $\vec{a}$  and  $\vec{b}$ .

To find out the dependence of directional motion on the size of a particle, the response of small magnetic particles is determined. Due to a low interactive volume, a magnetic particle with  $4 \mu m$  diameter lies at the vertex A for the field initial state  $\vec{a}$ , as illustrated in Fig. 5.4 e. After switching the field to  $\vec{b}$ , the bead is first actuated by the magnetic field gradient from the adjacent edge of below neighboring triangle, followed by its attraction towards the vertex B. Fig. 5.4 f shows this tip-to-tip backward motion of a  $4 \mu m$  bead. Long spikes in the local velocity plots describe the straight backward movement patterns at the symmetric field switching.

At the asymmetrically applied field  $H_{ext}$ , the preferential position of a  $4 \mu m$  bead is changed again due to the small interaction volume. As expected, the bead is positioned

at the edge A of an element for the initial field state  $\vec{a}^{+15^\circ}$  as illustrated on the calculated magnetic field gradient maps in Fig. 5.4 g. After the field is switched to  $\vec{b}^{-15^\circ}$ , the bead moves naturally upwards due to its previous position now being near to the FG at the upper edge B. Experimental demonstration of this edge-to-edge forward motion is given in Fig. 5.4 h. Velocity curves spiking in both vertical and horizontal directions display an edge-to-edge actuation of a  $4\ \mu\text{m}$  bead under  $H_{ext}$  changing between  $\vec{a}^{+15^\circ}$  and  $\vec{b}^{-15^\circ}$ .

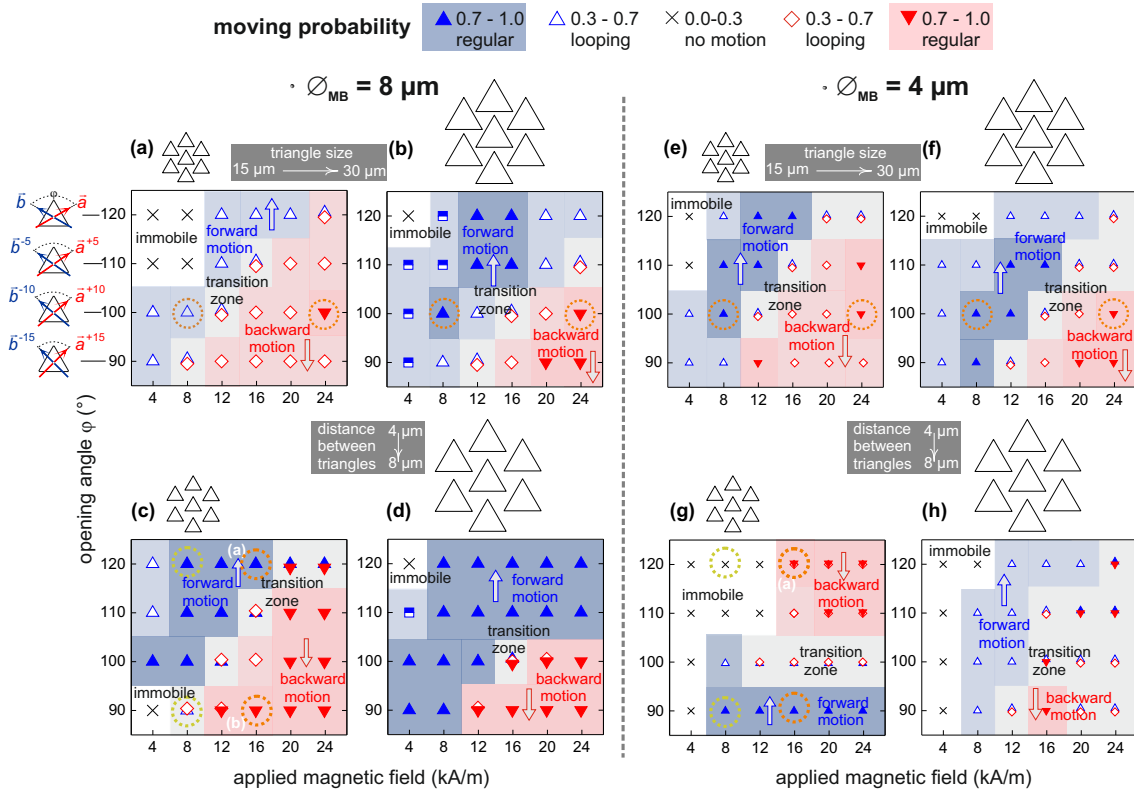


**Figure 5.4:** Simulated magnetic field gradient maps with the positions of an  $8\ \mu\text{m}$  bead, before and after its movement on the field switching from  $\vec{a}$  to  $\vec{b}$ . (b) Optical image shows the forward motion. The net movement is vertical as illustrated by spikes in velocity plots. (c) Shifted positions of the bead for an asymmetric field sequence is shown. (d) Curling backward motion occurs, due to a shifted starting position, resulting from the asymmetric FG. Velocity plots illustrate the sideways and vertical movement. (e) A  $4\ \mu\text{m}$  bead moves downward from tip A to B on the field changing from  $\vec{a}$  to  $\vec{b}$ . (f) Tip-to-tip backward movements are shown by spikes in velocity curves. (g) For an asymmetric field changing from  $\vec{a}^{+15^\circ}$  to  $\vec{b}^{-15^\circ}$ , the bead positioning at the edges A and B before and after its motion are indicated. (h) Path of edge-to-edge motion and corresponding velocity curves show zigzag movement patterns in the forward direction. Reproduced from Ref. 64 with permission © 2018 Wiley-VCH.

The varying stray magnetic field gradient generates the magnetic force on a particle based on its physical properties (size and volume magnetization). Magnetic particles with different sizes attain different magnetic potentials on the periodic magnetic patterns, which leads to their motion in the opposite direction. Such a manipulation can be difficult, if the size and interface spacing of magnetic patterns is not carefully considered. The required  $H_{ext}$  amplitude and its degree of asymmetry, can also be determined to generate the particles size dependent distinct magnetic potentials for their simultaneous motion and separation.

## 5.2 Motion Dependence on Geometric and Magnetic Configurations

The effective magnitude of stray magnetic field gradient on the volume of a magnetic particle, directly depends on the size and inter-structure spacing of the magnetic structures. The strength of applied field and the opening angle of the switching applied field  $H_{ext}$  collectively define the type and direction of motion. Therefore, an understanding of the MB response resulting from the changed geometric and magnetic parameters of magnetic structures is required to ensure a controlled motion.



**Figure 5.5:** Phase diagrams summarizing the motion response of  $8\ \mu\text{m}$  and  $4\ \mu\text{m}$  MBs at varying  $H_{ext}$  configurations on MSs with different sizes and inter-structure spacing. (a)-(b) Different response of  $8\ \mu\text{m}$  beads on small and large MSs with an inter-structure distance of  $4\ \mu\text{m}$ . (c)-(d) Facilitated bidirectional motion of  $8\ \mu\text{m}$  beads for an increased inter-pattern spacing of  $8\ \mu\text{m}$ . (e)-(f) Identical behavior of  $4\ \mu\text{m}$  beads on small and large MSs. (g) Flipped regimes of bidirectional motion for an increased inter-pattern spacing. (h) Reduced motion possibilities for the  $4\ \mu\text{m}$  beads on large MSs with a wide spacing. Regimes for the bidirectional motion with the transition and immobile zones are indicated. Movement probabilities are assigned with various symbols. MBs are moved with switching frequencies of  $2\ \text{Hz}$  and  $4\ \text{Hz}$  on patterns with an inter-pattern spacing of  $4\ \mu\text{m}$  and  $8\ \mu\text{m}$ , respectively. Reproduced from Ref. 64 with permission © 2018 Wiley-VCH.

Experimental motion behaviors of MBs with  $\varnothing_{MB} = 8\ \mu\text{m}$  and  $4\ \mu\text{m}$  on MSs with the edge length of  $15\ \mu\text{m}$  and  $30\ \mu\text{m}$  and inter-pattern spacing of  $4\ \mu\text{m}$  and  $8\ \mu\text{m}$  are

summarized as phase diagrams in Fig. 5.5. The directional movement of large  $8 \mu m$  beads is largely hindered on closely spaced small size MSs (edge length =  $15 \mu m$ ), as shown by its overall response in the phase diagram in Fig. 5.5 a. Upon its inversion, the closely spaced magnetic field gradient landscape becomes effective on the large volume MB, from both forward and backward edges, which hinders its directional transport. The bead might move a few steps, but primarily, it loops back and forth among adjacent elements as indicated by the symbols for the motion probability in Fig. 5.5.

Large magnetic structures, forming the widely positioned magnetic field gradients, facilitates the directed motion, depending on the field configuration. A regular forward and backward movement of  $8 \mu m$  beads exhibiting motion probabilities of 0.7-1.0 on structures with an edge length of  $30 \mu m$  and inter-structure spacing of  $4 \mu m$  is highlighted in Fig. 5.5 b. The directed transport of  $8 \mu m$  beads is further improved on increasing the inter-structure spacing to  $8 \mu m$  (Fig. 5.5 c and Fig. 5.5 d). Overall, a common trend of forward and backward motion for respective large and small opening angle ( $\varphi_{sw}$ ) of switching  $H_{ext}$  is determined. At a fixed  $\varphi_{sw}$ , the forward and backward movements are attainable for respective lower and higher amplitudes of  $H_{ext}$ . At the transition zone, an unpredictable response is observed. Microbeads remain immobile at low amplitude  $H_{ext}$ .

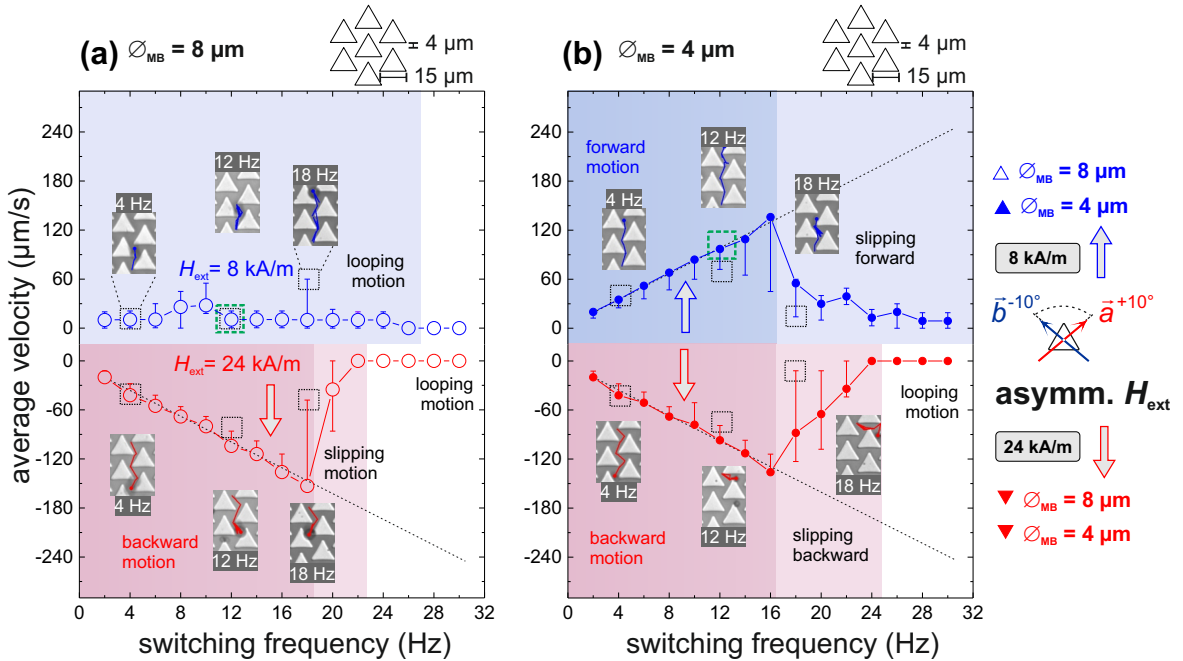
Small MBs with a diameter equal to the inter-structure spacing  $4 \mu m$  exhibit the regular bidirectional motion on small sized magnetic structures as shown in Fig. 5.5 e. An identical behavior is determined on large MSs (Fig. 5.5 f). An altogether opposite directed motion is realized for  $4 \mu m$  beads on structures with the inter-structure distance twice the bead diameter, which is indicated as the flipped regimes of forward and backward motion in Fig. 5.5 g. This inverted motion of  $4 \mu m$  beads together with the regular motion of  $8 \mu m$  beads on the same magnetic surface and  $H_{ext}$  conditions (Fig. 5.5 g vs Fig. 5.5 c) allows the simultaneous two-way transport.

The motion of small beads becomes difficult on large magnetic structures, if the inter-structure distance is also large. Fig. 5.5 h depicts the exemplary response of  $4 \mu m$  beads on MSs with an edge length of  $30 \mu m$  and inter-structure distance of  $8 \mu m$ . The widely spaced vertex field gradient FG remains mostly non-effective on the low magnetic volume of the particle for its movement to the next MS. Similar to the hindered motion of the large MBs (Fig. 5.5 a), due to their excessive interaction with closely spaced magnetic field gradient (FG) on small triangles, small MBs are not transportable through widely spaced FG on large triangles. Yet, the limited or no motion of one type of beads and a regular transport of the other type permits the selective sorting under equal  $H_{ext}$  conditions.

### 5.2.1 Transport Velocity of Microbeads

To ensure the efficient transport and separation of MBs, the attainable average velocity at constant magnetic field configurations are determined. Depending on the bead size, the directed motion of different type MBs may differ on changing the switch-

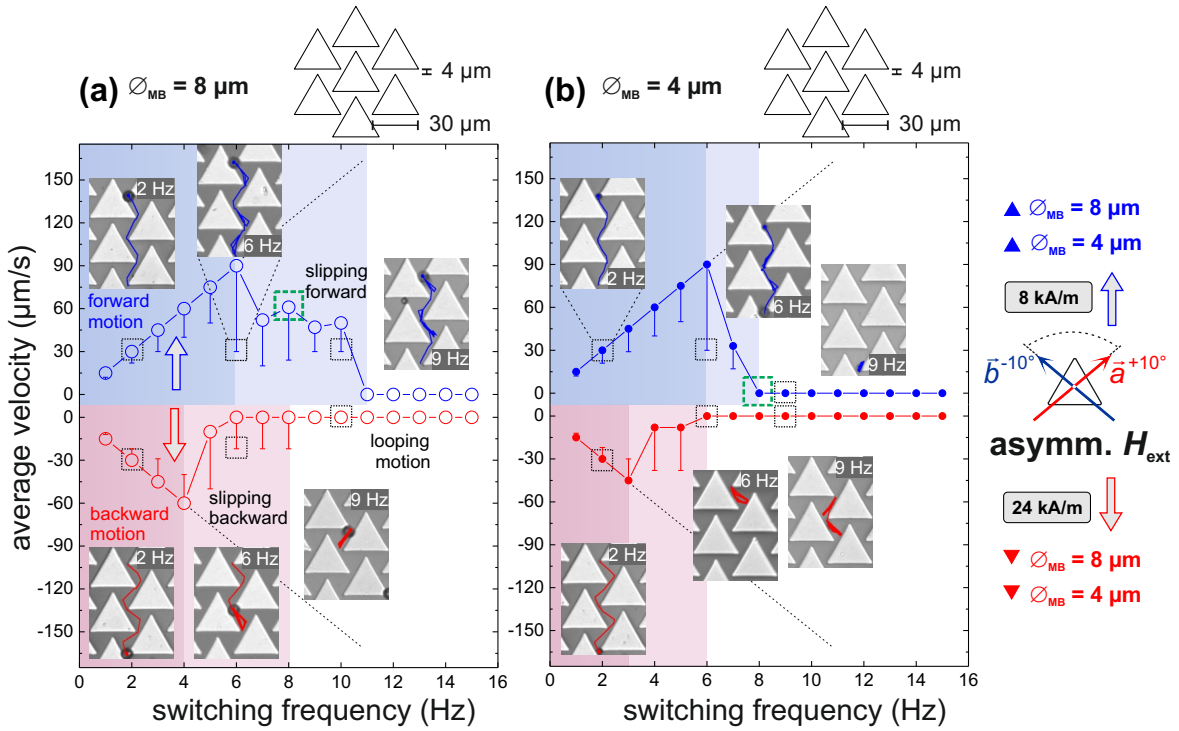
ing rate of applied magnetic field  $H_{ext}$ . Here, the dynamics of MBs are determined for increasing switching frequencies of  $H_{ext}$ , which reveals various frequency dependent regimes of motion. The exemplary bidirectional motion behavior of MBs for an  $H_{ext}$  with two different amplitudes at a constant opening angle  $\varphi_{sw}$  is presented in Fig. 5.6 as average velocity  $v_{ave}$  vs switching frequency  $f_{swit}$  plots. The chosen amplitudes of  $H_{ext}$  represent the general bidirectional response in the phase diagram of Fig. 5.5 a. At magnetic switching with the lower amplitude (8 kA/m),  $8\ \mu\text{m}$  beads maintain their looping (locked) motion on small patterns throughout the increasing frequency of switching magnetic field as shown by the flat curve of average velocity around zero (blue shaded) in Fig. 5.6 a. Insets show the recorded motion of beads at various  $f_{swit}$ .



**Figure 5.6:** Average velocity  $v_{ave}$  vs switching frequency  $f_{swit}$  plots for  $8\ \mu\text{m}$  and  $4\ \mu\text{m}$  MBs under an asymmetrically changing  $H_{ext}$  with amplitudes of  $8\ \text{kA/m}$  and  $24\ \text{kA/m}$  for the bidirectional motion on small MSs. (a)  $8\ \mu\text{m}$  beads exhibit looping and backward motion at respective lower and higher amplitude of  $H_{ext}$ . (b)  $4\ \mu\text{m}$  beads move identical in the forward and backward direction. Regimes of MB motion are labeled. Insets show exemplary paths of motion. Error bars represent the secondary response of MB motion.

On the increased amplitude of applied field  $H_{ext} = 24\ \text{kA/m}$  MBs exhibit the regular downward motion (red shaded), indicated as negative velocity values. Initially, a linear transport behavior is determined up to a critical switching frequency  $f_{swit}$  of  $18\ \text{Hz}$ . Above  $f_{swit}$ , beads occasionally slip through fast inverting field gradient FG and thus, nonlinear transport occurs. Average velocity  $v_{ave}$  reduces thereby drastically. A further increase in  $f_{swit}$  causes the looping of  $8\ \mu\text{m}$  MBs around adjacent elements, as indicated with a zero average velocity in Fig. 5.6 a. By simply increasing the strength of applied field  $H_{ext}$  ( $8\ \text{kA/m}$  vs  $24\ \text{kA/m}$ ), the dynamics of MBs are controlled from their hindered motion to the regular backward motion. Generating the higher FG at

the edge of the lower neighboring element at higher strength fields moves the large beads backward on these small structures.



**Figure 5.7:** Average velocity  $v_{ave}$  vs switching frequency  $f_{swit}$  plots for  $8 \mu\text{m}$  and  $4 \mu\text{m}$  MBs under an asymmetrically changing  $H_{ext}$  with amplitudes of  $8 \text{ kA/m}$  and  $24 \text{ kA/m}$  for the bidirectional motion on large MSs. (a)  $8 \mu\text{m}$  beads exhibit bidirectional regimes of motion at the lower and higher amplitude of  $H_{ext}$ . (b)  $4 \mu\text{m}$  beads show a shorter regime of slipping motion. Regimes of MB motion are labeled. Insets show exemplary paths of motion. Error bars represent the secondary response of MB motion.

On equivalent applied field conditions  $4 \mu\text{m}$  MBs with small interactive volume exhibit a regular bidirectional motion behavior on these small size patterns up to switching frequency ( $f_{swit}$ ) of  $16 \text{ Hz}$ , followed by the regimes of slipping and looping motion at higher  $f_{swit}$ , as labeled in Fig. 5.6 b. The size of the bead, equaling the inter-structure distance ( $4 \mu\text{m}$ ) facilitates its forward motion from its initial position at the tip (see insets). Compare the position of the  $8 \mu\text{m}$  bead onto two magnetic structures MSs. On inverting the field gradient FG, the starting positions cause small beads to move along the edge of the upper MS, while large beads loop along the edge of the lower MS. Hence, at fixed field conditions,  $8 \mu\text{m}$  and  $4 \mu\text{m}$  beads can be separated using the respective looping and regular forward motion.

Changing the size of MSs affects MB motion considerably. Particularly, the backward curling motion, occurring through three adjacent MSs is impaired on large MSs. The indirect movement path through the magnetic field gradient at longer edges of these large size structures, causes the decreased critical frequency  $f_{crit}$  of MBs and thus, a shorter regime (indicated by red shading) of linear motion occurs. Exemplary results as average velocity vs switching frequency plot in Fig. 5.7 a demonstrate the



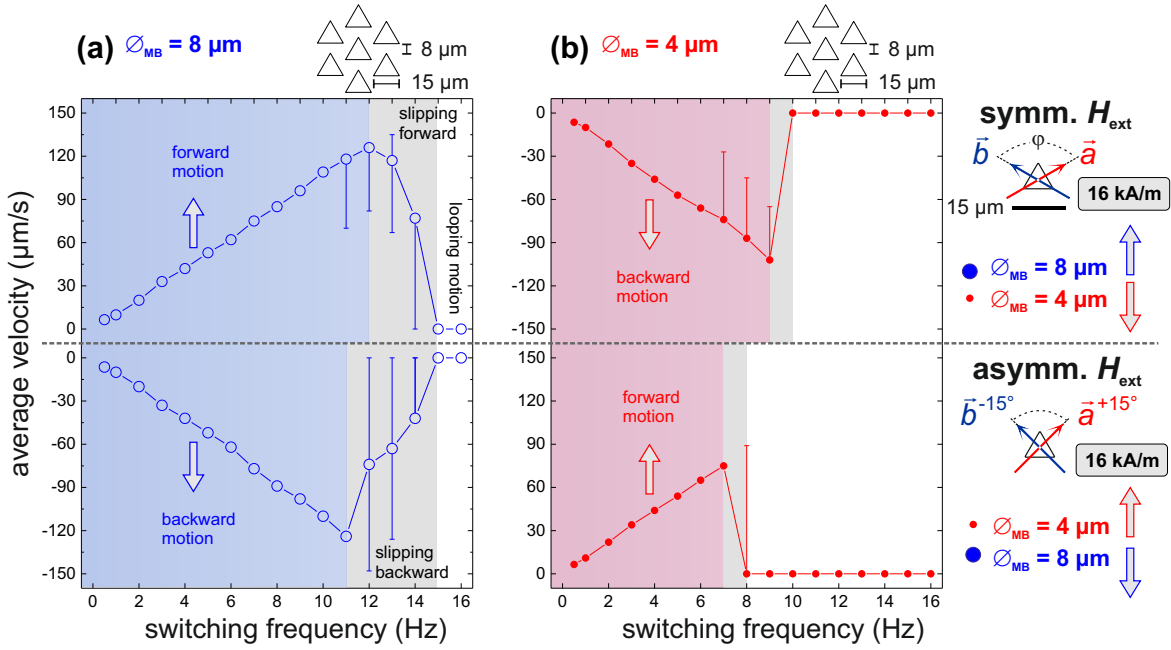
continuous forward motion of  $4\ \mu\text{m}$  beads up to the critical frequency ( $f_{crit} = 6\ \text{Hz}$ ), followed by a wide regime of slipping and looping motion at higher  $f_{swit}$ . In the slipping regime, beads still move forward but with a reduced  $v_{ave}$ , due to the inclusions of random looping, as shown in Fig. 5.7 a. Backward motion, enabled by the higher amplitude of magnetic field, is limited to a reduced critical frequency ( $f_{crit} = 4\ \text{Hz}$ ). After the  $f_{crit}$ , the slipping backward motion with drastically reduced  $v_{ave}$  and the looping motion occurs at higher  $f_{swit}$ .

Small  $4\ \mu\text{m}$  MBs show similar behavior on large triangular structures, except a short regime of forward slipping motion (light blue shaded), which leads to an early onset of the looping motion. Comparing the slipping regimes of  $8\ \mu\text{m}$  and  $4\ \mu\text{m}$  beads in Fig. 5.7 a and Fig. 5.7 b, large beads with the higher interactive volume, could follow the fast inverting field gradient FG at the edges of triangles, whereas the small beads could not reach the next higher FG with the high field frequency ( $f_{swit}$ ). An inset in Fig. 5.7 b for  $f_{swit} = 9\ \text{Hz}$ , shows an immobile  $4\ \mu\text{m}$  bead around the vertex. Hence, forward slipping large magnetic particles can be sorted from the non-moving small particles using the non-linear dynamics at a high switching frequency  $f_{swit}$  of the applied field (e.g.  $8\ \text{Hz}$ ).

Overall, the smaller regime for the backward linear motion (red plots in Fig. 5.7) is attributed to the widely spaced magnetic field gradient FG at the edge of the lower neighboring structure. Large size structures do not facilitate the backward motion of MBs. The FG at the lower neighboring structure, responsible for the backward motion, remains less effective on bead's initial position for large structures (see also Fig. 5.4 c and d). Consequently, the beads could not follow the fast changing magnetic fields and show smaller regime of linear motion in backward direction.

Providing the geometric constraint through the size and spacing among structures facilitates the selective movement of one type of MBs, while making the other type non-transportable. To enable the simultaneous separation for both types of beads, the distance between the elements is increased to open multiple paths of motion. For the opposite directed motion of large and small MBs, see Fig. 5.3. Here, we determine the achievable average velocities of  $8\ \mu\text{m}$  and  $4\ \mu\text{m}$  beads, moving across each other for the symmetrically and asymmetrically changing magnetic fields with the field strength of  $16\ \text{kA/m}$ . Large beads move continuously forward up to their critical frequency ( $f_{crit} = 12\ \text{Hz}$ ) as shown in Fig. 5.8 a. On further increase in the switching frequency  $f_{swit}$ , the typical slipping and looping motion occur. By changing  $H_{ext}$  to the asymmetric configuration, the identical motion response is determined in the backward direction for the whole range of applied frequencies.

At equal magnetic field conditions, small beads are moved in the opposite direction (Fig. 5.8 b). Under the fast changing field gradient FG at high  $f_{swit}$ ,  $4\ \mu\text{m}$  beads with low magnetic volume are difficult to move over these widely spaced structures. Therefore,  $f_{crit}$  for their regular bidirectional motion is lower than for the  $8\ \mu\text{m}$  beads. Moreover, a sudden transition from the continuous to looping motion for  $4\ \mu\text{m}$  beads on structures with an inter-structure distance of  $8\ \mu\text{m}$  explains a direct dependence of motion on the interaction volume of a magnetic particle. At the  $f_{swit}$  above the critical



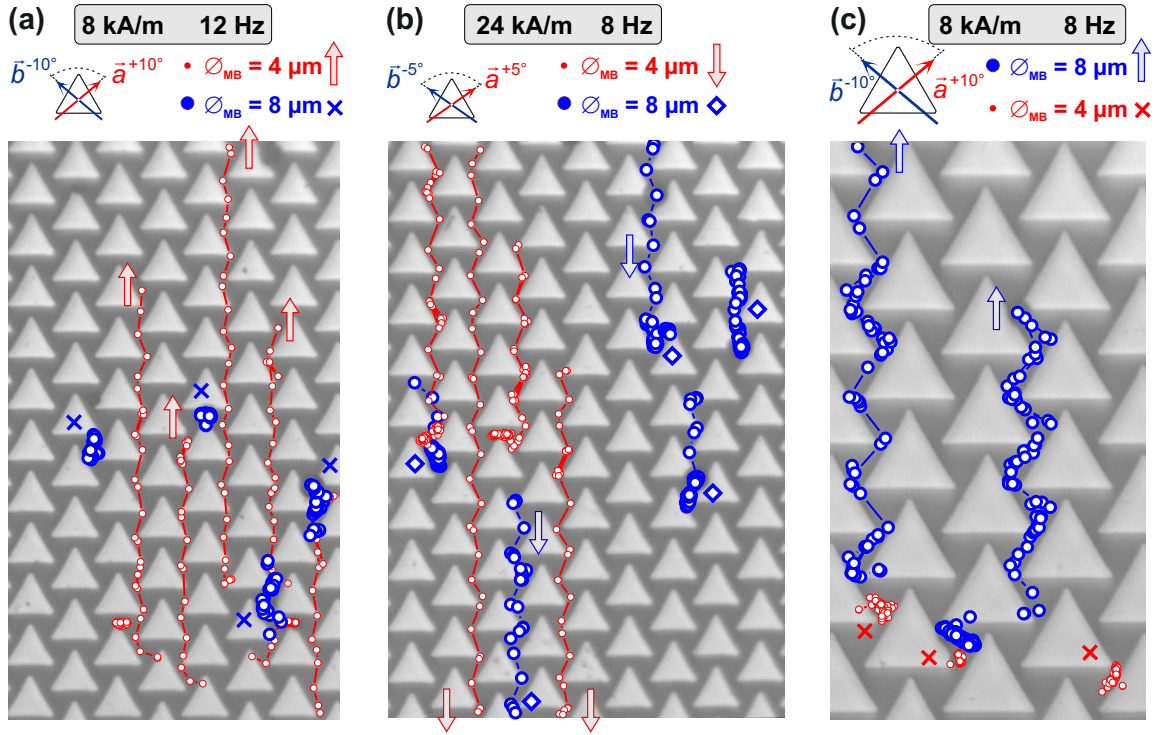
**Figure 5.8:** Average velocity  $v_{ave}$  vs switching frequency  $f_{swit}$  plots for 8  $\mu\text{m}$  and 4  $\mu\text{m}$  MBs under the symmetric and asymmetric applied field with a fixed amplitude of 16 kA/m for the simultaneous bidirectional movements. (a) 8  $\mu\text{m}$  beads exhibit forward and reverse motion at respective symmetric and asymmetric  $H_{\text{ext}}$ . (b) 4  $\mu\text{m}$  beads move in opposite direction at equal applied field conditions. Regimes of MB motion are labeled. Error bars represent the secondary response of motion. Reproduced from Ref. 64 with permission © 2018 Wiley-VCH.

limit, the 4  $\mu\text{m}$  beads move back and forth just around a single triangle. In contrast, the 8  $\mu\text{m}$  beads slip along the fast inverting FG at edges due to their higher effective volume and thus are yet reachable to the next higher FG. The MB size dependent different critical frequency leads to its different achievable velocity. Compare the average velocity of 8  $\mu\text{m}$  and 4  $\mu\text{m}$  beads in Fig. 5.8 a and b.

### 5.2.2 Microbeads Separation Schemes

The geometrically constrained arrangement of magnetic patterns generates the closely spaced stray magnetic field gradient and allows the easy movement of small size MBs, while hinders the motion of large MBs. Thus, 4  $\mu\text{m}$  particles can be selectively transported to a target location on the chip with the restricted motion of 8  $\mu\text{m}$  particles. Experimental results for this selective separation are presented in Fig. 5.9. Under the asymmetrically changing magnetic field with a lower amplitude of 8 kA/m, a group of 4  $\mu\text{m}$  particles is transported forward, whereas 8  $\mu\text{m}$  particles are kept immobile around adjacent patterns, as shown by the movement paths in Fig. 5.9 a.

For a selective transport in the backward direction, the higher field amplitude of 24 kA/m with a small change in the field asymmetry allows the movement of small size MBs, whereas blocks the motion of large MBs. Exemplary results in Fig. 5.9 b

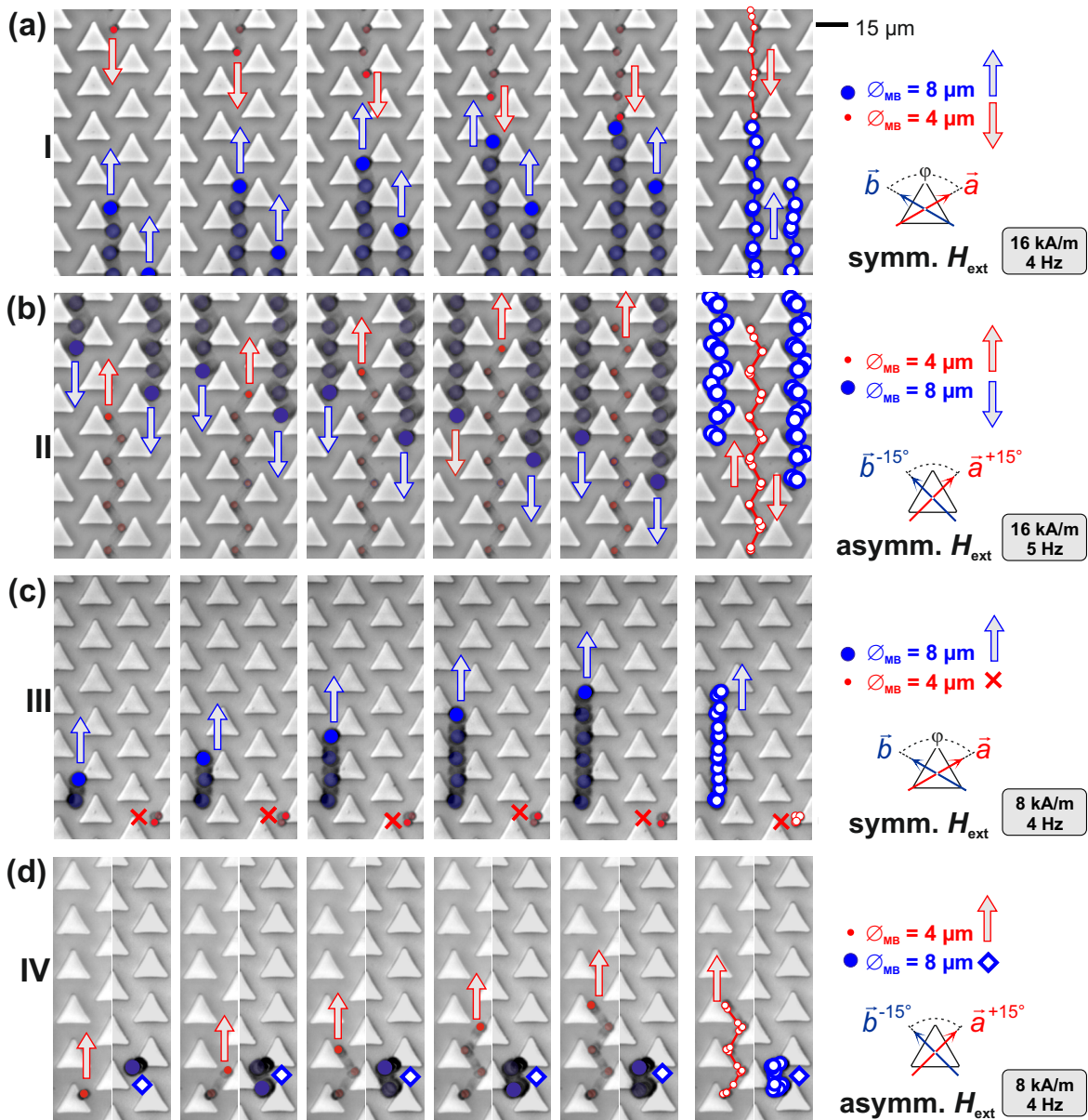


**Figure 5.9:** Small MBs with  $4\ \mu\text{m}$  diameter are moving continuously forward while  $8\ \mu\text{m}$  beads are looping. (b) An ensemble of  $4\ \mu\text{m}$  beads is moving backward against the impaired motion of  $8\ \mu\text{m}$  beads. (c) The slipping movement of  $8\ \mu\text{m}$  beads and immobile response of  $4\ \mu\text{m}$  beads for their selective sorting in the non-linear regime of motion is shown. Magnetic field configurations are labeled.

illustrate the linear backward motion of  $4\ \mu\text{m}$  beads versus the impaired backward motion of  $8\ \mu\text{m}$  beads with an  $H_{ext}$  changing between  $\vec{a}^{+5^\circ}$  and  $\vec{b}^{-5^\circ}$ . Even this small asymmetry in applied  $H_{ext}$  reduces the effect of field gradient from the edge of lower neighboring structure (responsible for backward motion, see also Fig. 5.4 c and d) on the initial position of  $8\ \mu\text{m}$ . Hence, the backward movement is impaired. Meanwhile,  $4\ \mu\text{m}$  beads move continuously backward, without being effected by the FG from the neighboring structure.

Another way to enable the size selective separation is the use of nonlinear dynamics. Particularly, if both types of particles move preferentially in the same direction for a constant  $H_{ext}$  condition. For  $H_{ext}$  above the critical frequency of MBs on large magnetic elements, making small beads non-reachable to the fast changing magnetic field gradient at the vertex of triangles and allowing the large beads to slip, leads to their selective separation. Results of this separation scheme in Fig. 5.9 c show the forward slipping motion of  $8\ \mu\text{m}$  beads and the immobile response of  $4\ \mu\text{m}$  beads.

To achieve a simultaneous separation in a mixture of MBs, multiple movement patterns depending on the size of MBs are needed along a magnetic pathway. This is enabled by moving large and small magnetic MBs in opposite directions on widely spaced magnetic structures. For a constant external field strength, equal stray field gradients differently effective on different size MBs guide them in opposite directions.



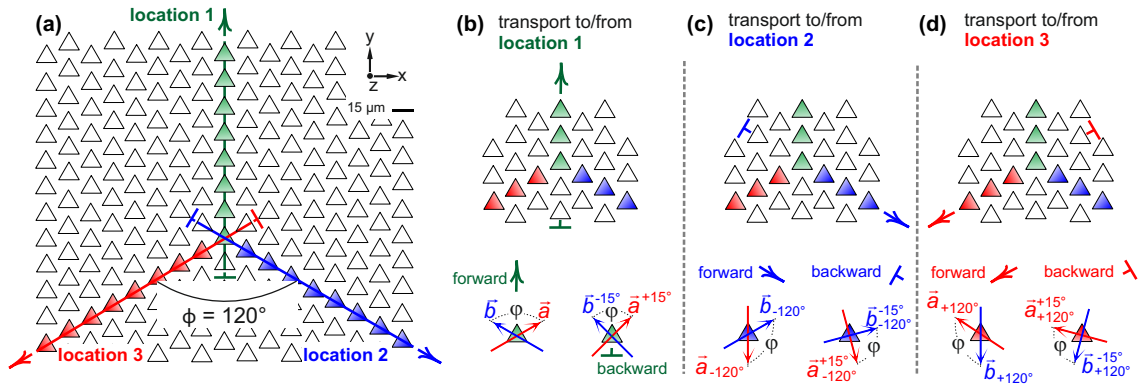
**Figure 5.10:** (a) The forward movement of  $8 \mu\text{m}$  beads with a simultaneous backward motion of  $4 \mu\text{m}$  beads for the symmetrically switching magnetic field with an amplitude of  $16 \text{ kA/m}$  is shown. (b) For the asymmetric  $H_{ext}$ ,  $8 \mu\text{m}$  beads move backward with a curled path of motion, while  $4 \mu\text{m}$  beads move edge-to-edge in the forward direction. (c) A symmetric  $H_{ext}$  with a reduced field amplitude of  $8 \text{ kA/m}$  moves large  $8 \mu\text{m}$  beads forward, whereas small  $4 \mu\text{m}$  beads remain immobile. (d) For the asymmetric  $H_{ext}$  with the reduced field strength, small  $4 \mu\text{m}$  beads move forward, while large  $8 \mu\text{m}$  beads move back and forth between three neighboring structures. Reproduced from Ref. 64 with permission © 2018 Wiley-VCH.

Fig. 5.10 a shows the forward movement of  $8 \mu\text{m}$  beads with the simultaneous backward motion of  $4 \mu\text{m}$  beads for an  $H_{ext}$  switching between  $\vec{a}$  and  $\vec{b}$ . Asymmetrically switching  $H_{ext}$  with the same field amplitude enables the opposite directed motion of large and small MBs as shown in Fig. 5.10 b. With the reduced strength of applied field

( $H_{ext} = 8$  kA/m) the decreased magnitude of stray field gradient FG still moves the large  $8\ \mu\text{m}$  bead forward, while the small  $4\ \mu\text{m}$  bead remains immobile (Fig. 5.10 c). The immobility of the small bead occurs due to its initial position being too far from the effective FG of the next structure. Alternatively, now the asymmetric  $H_{ext}$  with the reduced field strength moves  $4\ \mu\text{m}$  bead edge-to edge forward, while the  $8\ \mu\text{m}$  bead moves back and forth with no clear direction of transport (Fig. 5.10 d). This back and forth wobbling motion of  $8\ \mu\text{m}$  is related to the closely competing FG at both sides of the magnetic structures. See Movie 5.1-5.4. in Appendix-E.1.3 for the separating motion of MBs, shown in Fig. 5.10.

## 5.3 Trilateral Transport of Microbeads

With a control on the directed motion of microbeads (MBs), their transport to an arbitrary location on the magnetic chip is now possible. A sketch of the magnetic surface in Fig. 5.11 a depicts the 3-line symmetry (indicated as colored arrays) for the transport towards three exemplary target locations 1 (straight upwards), 2 (right diagonal downwards) and 3 (left diagonal downwards). Directions of forward and backward motion along the paths are assigned with arrow heads and flat tails. Fig. 5.11 b depicts the upward transport to location 1 (forward motion) and from location 1 to the starting position (backward motion) along a vertical array (green) with the respective symmetric and asymmetric applied field. The transport to and from location 2 and location 3 can be achieved by an angular shifting of the switching  $H_{ext}$  by  $-120^\circ$  and  $+120^\circ$  respectively from the original position. For example,  $H_{ext}$  changing between  $\vec{a}_{-120^\circ}$  and  $\vec{b}_{-120^\circ}$  enables the forward motion towards location 2. Fig. 5.11 c and Fig. 5.11 d indicate the pathways of bidirectional motion with the shifted orientations of switching  $H_{ext}$  for the corresponding location 2 and 3.



**Figure 5.11:** A sketch of trisymmetric magnetic structures showing the transport directions towards location 1, location 2 and location 3. (b) A vertical array indicates a straight upward and downward path with symmetrically ( $\vec{a}$  and  $\vec{b}$ ) and asymmetrically ( $\vec{a}^{+15^\circ}$  to  $\vec{b}^{-15^\circ}$ ) changing  $H_{ext}$ . (c) The transport to and from location 2 is achieved at  $H_{ext}$  switching between  $\vec{a}_{-120^\circ}$  and  $\vec{b}_{-120^\circ}$  for the forward direction and  $\vec{a}^{+15^\circ}$  and  $\vec{b}^{-15^\circ}$  for backward direction along the right diagonal array (blue). (d) Similarly, the transport to and from location 3 occurs along the left diagonal array (red) for shifting the position of switching  $H_{ext}$  to  $+120^\circ$  from its original configuration.

At the symmetric ( $\vec{a}$  and  $\vec{b}$ ) and asymmetric configuration ( $\vec{a}^{+15^\circ}$  and  $\vec{b}^{-15^\circ}$ ) of  $H_{ext}$ , large and small particles can be transported in opposite directions as shown in Tab. 5.1. For the asymmetric fields, shifting the second field state from  $\vec{b}^{-15^\circ}$  to  $\vec{b}_{-180^\circ}^{-15^\circ}$  does not affect the motion response of  $4\mu\text{m}$  particles but inverts the motion of  $8\mu\text{m}$  particles (see Appendix-C.3). With  $H_{ext}$  switching between  $\vec{a}^{+30^\circ}$  and  $\vec{b}_{-180^\circ}^{-30^\circ}$ , the forward movement of  $4\mu\text{m}$  particles is still attained but the directional motion of  $8\mu\text{m}$  particles is locked as indicated in Tab. 5.1. The reason is discussed in the coming section.

Field sequence	①	②	③	④		
Field amplitude, $H_{ext} = 16 \text{ kA/m}$						
Motion for $\varnothing_{MB} = 4 \mu\text{m}$	⊥	↑	↑	↑	forward	↑
Motion for $\varnothing_{MB} = 8 \mu\text{m}$	↑	⊥	↑	×	backward	⊥
					locked	×

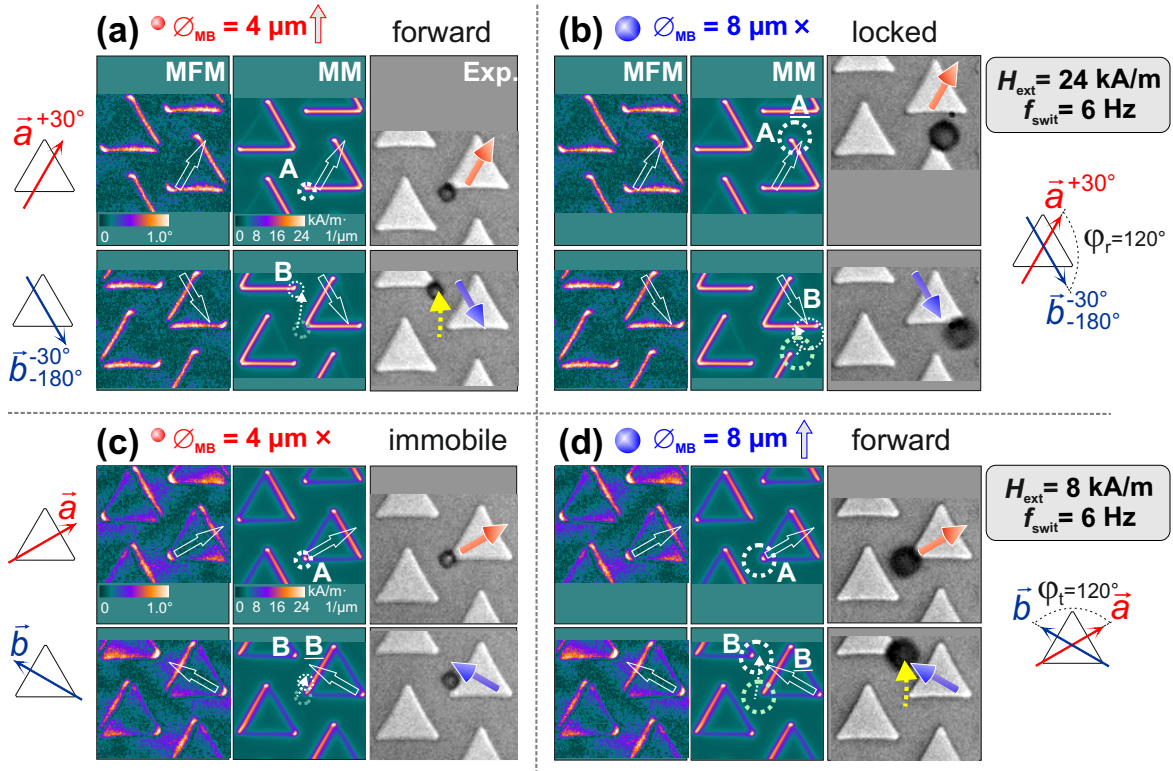
**Table 5.1:** Directed motion of MBs with  $4 \mu\text{m}$  and  $8 \mu\text{m}$  diameters under the symmetric and asymmetric field configurations with a fixed amplitude of  $H_{ext}$  ( $16 \text{ kA/m}$ ).

A proof of concept to confirm the functionality of this trisymmetric magnetic surface is the reproduction of particle movements by rotating the chip in x-y plane. This alternative method confirms the motion response of large and small particles along all six paths of these hexagonally arranged structures. Changing the direction of moving particles using the chip rotation with a single  $H_{ext}$  configuration is shown in Movie 5.5-5.8 in Appendix-E.1.3

### 5.3.1 Selective Movement of MBs from a Mixture

Separation efficiency of magnetic microbeads on a chip can be described as the number of separated beads in a mixture of two different types of beads in a shortest time. Simultaneous bidirectional motion of MBs unlikely provide high separation efficiency, since the oppositely moving MBs hinder each others motion on a magnetic pathway. Because of the magnetic heterogeneity (Sec. 3.2), even the selective movement of one type of MBs becomes very difficult at the investigated applied field conditions. The challenge lies in achieving the controlled directed movement for individual ensembles of different MBs without the cross movement. In other words, the efficiency of the selective separation relies on a simultaneous control of mixed ensembles of MBs. The individual  $H_{ext}$  conditions with the associated amplitude and asymmetry, enabling the separation of one type of MBs and the simultaneous locking of other type, can disclose high separation efficiency.

Exemplary results for the selective separation of single MBs, are shown in Fig. 5.12. An applied magnetic field  $H_{ext}$  directing parallel to one edge of the triangle generates the stray fields ( $H_{str}$ ) around the other two edges, as shown by MFM and MM simulations in Fig. 5.12 a and Fig. 5.12 b. A  $4 \mu\text{m}$  bead with a small magnetic volume has its initial position at the vertex for the field condition  $\vec{a}^{+30^\circ}$ . After the field is switched to  $\vec{b}_{-180^\circ}^{-30^\circ}$ , the bead moves forward through the inverted stray field gradient FG along the edge B towards the vertex B. For the initial state  $\vec{a}^{+30^\circ}$ , the large  $8 \mu\text{m}$  bead attains its starting position at the vertex A near to the opposite edge A of the neighboring structure (Fig. 5.12 b). After the field is switched to  $\vec{b}_{-180^\circ}^{-30^\circ}$ , the initial position of the  $8 \mu\text{m}$  bead at the apex, being already closer to the inverted FG at the B and vertex



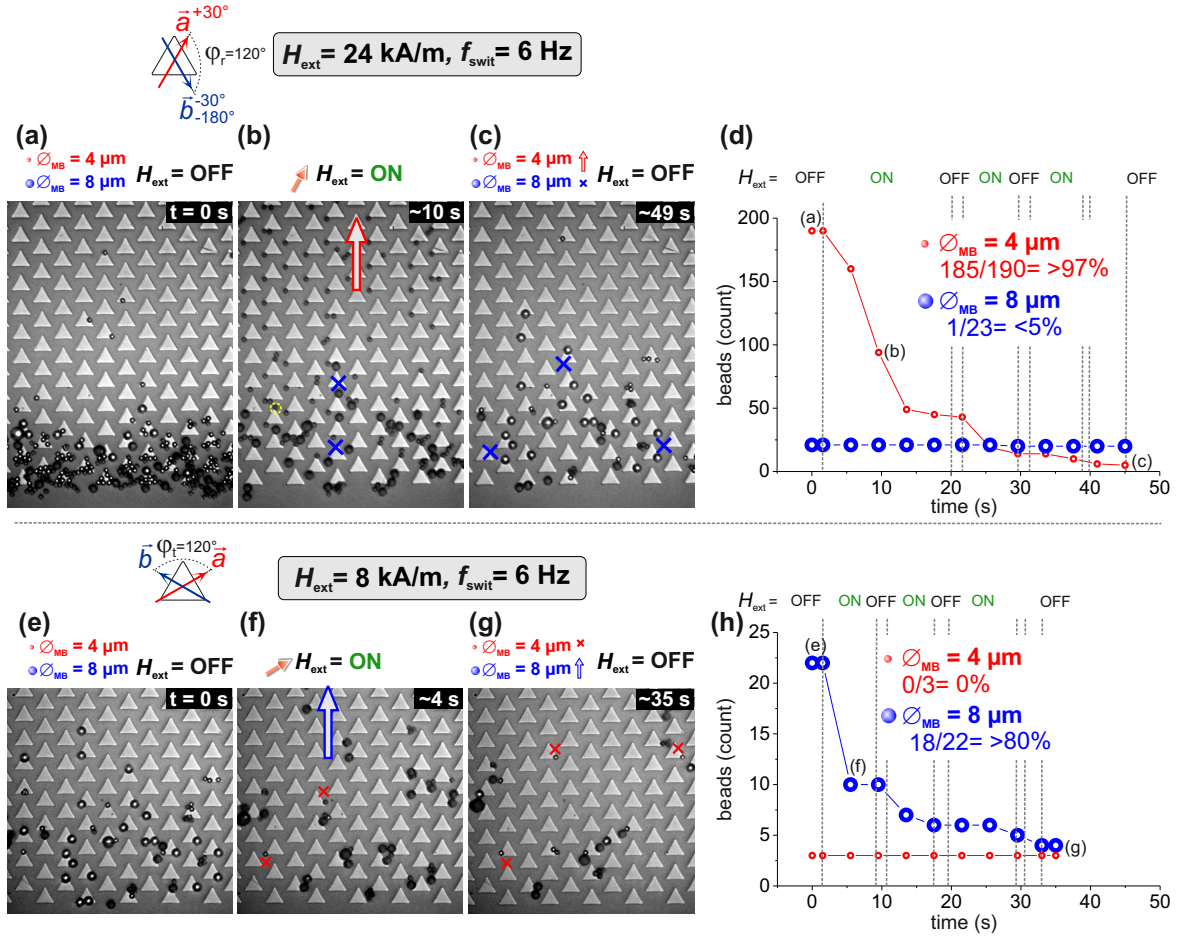
**Figure 5.12:** (a) Stray magnetic field gradient  $FG$  at a higher strength ( $24 \text{ kA/m}$ ) magnetic field and the corresponding positions of a  $4 \mu\text{m}$  bead. The bead moves tip-to-tip forward on switching the field direction from  $\vec{a}^{+30^\circ}$  to  $\vec{b}^{-30^\circ}$ . (b) Stable positions of an  $8 \mu\text{m}$  bead at the tip  $A$  near to the opposite edge  $\underline{A}$  for the equivalent  $H_{ext}$ . After the field is switched to  $\vec{b}^{-180^\circ}$ , the  $FG$  at the vertex  $B$  blocks the bead's lateral motion. (c) The reduced  $FG$  at a lower field strength ( $8 \text{ kA/m}$ ) and corresponding positions of the  $4 \mu\text{m}$  bead, before and after the switching of the symmetric  $H_{ext}$ . The small  $4 \mu\text{m}$  bead is immobile due to the lower  $FG$  at the edge  $\underline{B}$  for the field state  $\vec{b}$ . (d) Large  $8 \mu\text{m}$  bead positioned at the structures' interface moves forward at the equal  $H_{ext}$  conditions.

$B$ , causes a lock in its lateral motion along the vertical array.

On applying the symmetric magnetic field with a reduced strength ( $H_{ext} = 8 \text{ kA/m}$ ), the directed motion of the small and large beads can be inverted. Both beads are now symmetrically positioned along the field direction for the initial state  $\vec{a}$  as shown in Fig. 5.12 c and d, in contrast to their shifted positions in Fig. 5.12 a and b. On changing the field direction from  $\vec{a}$  to  $\vec{b}$ , the  $4 \mu\text{m}$  bead does not reach the next element, because of its low interaction volume and the lower magnitude of field gradient at  $\underline{B}$  (Fig. 5.12 c), whereas the large  $8 \mu\text{m}$  bead moves forward following the inverted field gradient (Fig. 5.12 d).

The selective separation of MB ensembles is presented in Fig. 5.13 as a region of observation on the magnetic chip with a heterogeneous mixture of  $4 \mu\text{m} + 8 \mu\text{m}$  diameter beads (approx. 190 and 20 in number respectively). The initial field state  $\vec{a}^{+30^\circ}$  with the higher strength ( $H_{ext} = 24 \text{ kA/m}$ ) positions single  $4 \mu\text{m}$  and  $8 \mu\text{m}$  beads at





**Figure 5.13:** (a) Region of observation on the magnetic chip with a heterogeneous mixture of magnetic beads with  $4 \mu\text{m}$  and  $8 \mu\text{m}$  diameters at  $H_{ext} = \text{OFF}$ . (b) Position of the moving beads at the initial field state  $\vec{a}^{+30^\circ}$ . Applied field switching with a fixed strength and switching frequency ( $24 \text{ kA/m}$ ,  $6 \text{ Hz}$ ) moves the  $4 \mu\text{m}$  beads tip-to-tip upward, whereas the  $8 \mu\text{m}$  beads are locked. Most small beads are separated within initial 10 seconds. (c) Locked  $8 \mu\text{m}$  beads are left behind. (d) MBs count versus time depict the forward separated  $4 \mu\text{m}$  beads.  $H_{ext}$  with a reduced field strength of  $8 \text{ kA/m}$  inverts the MBs separating motion. (e) Earlier locked  $8 \mu\text{m}$  beads. (f)  $8 \mu\text{m}$  and  $4 \mu\text{m}$  beads are confined at the field state  $\vec{a}$ .  $H_{ext}$  switching between  $\vec{a}$  and  $\vec{b}$  moves the large beads forward, whereas the small beads remain immobile. (g) Most of  $8 \mu\text{m}$  beads are separated upwards. (h) Immobile  $4 \mu\text{m}$  beads are left now. (j) MBs count versus time depict the forward separated  $8 \mu\text{m}$  beads.

the respective left vertex and at the interface of magnetic structures. The confined positions of MBs are shown in Fig. 5.13 b. Magnetic field changing between  $\vec{a}^{+30^\circ}$  and  $\vec{b}_{-180^\circ}^{-30^\circ}$  with a constant switching frequency of  $6 \text{ Hz}$  transport the  $4 \mu\text{m}$  beads tip-to-tip forward. Meanwhile, the  $8 \mu\text{m}$  beads move back and forth between the top and side vertex (left or right) of adjacent structures.

Fig. 5.13 b displays the positions of single moving  $4 \mu\text{m}$  beads and the absence of MBs clusters within the first 10 sec of an applied field ( $H_{ext} = \text{ON}$ ). An almost complete upwards separation of small MBs is achieved in approx. 49 sec with a simultaneous

locked motion of large MBs (indicated blue in Fig. 5.13 c). Fig. 5.13 d shows the trend of selective separation as decreasing number of  $4\ \mu\text{m}$  beads (count) against the time (s) for  $H_{ext}$  application. From a total 190 small MBs, 5 beads are still on the chip, which results in an overall separation efficiency of more than 97%. For the  $H_{ext}$  switching between  $\vec{a}^{+30^\circ}$  and  $\vec{b}_{-180^\circ}^{-30^\circ}$ , the number of large beads remains constant before (Fig. 5.13 a) and after (Fig. 5.13 c) the selective forward movement of  $4\ \mu\text{m}$  beads. A rapid separation during the first sequence of field ( $H_{ext} = \text{ON}$ ) is attributed to the high frequency of switching fields, transporting more than 75% beads of the total number. Changing between  $H_{ext} = \text{ON}$  and  $H_{ext} = \text{OFF}$  determines the slipping tendency of the locked  $8\ \mu\text{m}$  beads, at the one hand and repositions the  $4\ \mu\text{m}$  beads for the directed motion, on the other hand.

The less than 100% separation efficiency of small MBs is related to their occasional trapping at the secondary magnetic potential for high switching frequencies of  $H_{ext}$ . An example is shown as yellow highlighted MB position in Fig. 5.13 b. Nevertheless, experiments reveal that the preferential sites for  $4\ \mu\text{m}$  beads are the left and right vertexes of triangles on this field gradient landscape. Switching the magnetic field OFF and ON during the magnetic separation confirms a continuous forward motion of small MBs and a persistence locked motion of large MBs (Appendix-E.1.3 Movie 5.9).

Changing the orientation of switching  $H_{ext}$  (now symmetric) together with a reduced amplitude of 8 kA/m inverts the motion response of large and small particles. Fig. 5.13 e shows the previously locked  $8\ \mu\text{m}$  beads at  $H_{ext} = \text{OFF}$ . Magnetic field switching with a lower field strength moves the  $8\ \mu\text{m}$  beads forward as shown in Fig. 5.13 f by MBs positions at the structures' interface for the initial field  $\vec{a}$ . More than 75% of large MBs are moved upwards within the first 4 seconds of the field application.

The micrograph in Fig. 5.13 g shows that the  $8\ \mu\text{m}$  beads are selectively moved forward and the immobile  $4\ \mu\text{m}$  beads (indicated red, 3 in number) are left behind on the chip surface after  $H_{ext}$  switching between  $\vec{a}$  and  $\vec{b}$  for 35 seconds. From a total approx. 22 free moving particles, 4 particles are still present on the region of observation. This gives a separation efficiency of more than 80%. The lower efficiency of large particles (compared to more than 97% for small particles) is due to the blockage of the magnetic path by immobile small size particles and particle agglomerates. Repositioning the particles with  $H_{ext} = \text{ON}$  and OFF confirms a simultaneous forward motion of large MBs and immobile motion of small MBs (Appendix-E.1.3 Movie 5.10).

One sequence of asymmetrically changing higher strength  $H_{ext}$  enables the forward movement of small particles and lock the motion of large particles. Alternatively, small particles remain immobile, whereas large particles are movable with the second sequence of the symmetrically changing lower strength  $H_{ext}$ . This manipulation technique ensures the separation of the whole population of both type of particles, one after another. Small particles are separated first, by exploiting their naturally occurring easy motion. Movement of large beads is hindered by immobile small particles along the magnetic corridors. Yet, the mixed populations of magnetic particles are

now separable with high purity through a controlled motion of single particles.

## Discussion

Independent of the MBs position on the chip surface, the continuously changing direction of an in-plane applied magnetic field moves the single MBs along a triangular patterned magnetic surface. Determined by the sizes of MBs and magnetic patterns, a working range of  $H_{ext}$  strength and orientation is revealed for a directed bilateral motion of MBs. A field strength below a threshold limit does not move the MBs. Likewise, a field strength above the threshold field switches the directional movement due to the inversion of field gradient landscape at the patterns' interface. The same is valid for the degree of asymmetry in the  $H_{ext}$  direction. At the symmetrically applied field, the asymmetric field gradients at the triangles' interface are adjustable with the strength of  $H_{ext}$  to obtain a biased directional MB motion. Asymmetry in the  $H_{ext}$  direction moves the MB in reverse direction, facilitating a bidirectional control by adjusting the direction of  $H_{ext}$ . However, there exists a critical limit for the directional asymmetry. Moving MBs get trapped in opposite gradients and move in a closed loop at a single triangle, if the directional asymmetry crosses the threshold.

## Summary

The hexagonal arrangement of NiFe triangular structures, providing trisymmetric magnetic pathways enables the free lateral motion of magnetic MBs on a chip. The strength and asymmetry of  $H_{ext}$ , generating the tunable stray magnetic field gradient confine the MBs differently on the structures, depending on the size of MB. Single MBs with differently confined positions on the triangular magnetic structures can be moved in different directions along the inverting field gradient using a square wave modulated magnetic field. By this a simultaneous two-way motion of different microbeads is enabled. A size selective separation is demonstrated on a mixture of microbeads' populations with a high separation efficiency. The functionality of this triangular hexagonal magnetic surface is confirmed by moving different sized magnetic microbeads along all six paths with the chip rotation at single  $H_{ext}$  configurations.

# Chapter 6

## Multilateral Motion of Microbeads on a Hexasymmetric Magnetic Surface

Taking the advantage of high throughput in a free-flow system, the separation of biological cells was achieved with multiple targets of magnetic MBs.<sup>21</sup> Despite the advantage of magnetically patterned microchips, enabling a control on a single particle in a flow-less microfluidic environment and the separation of multiple types MBs remains challenging. On the population level, multiple sizes MBs were quantitatively sorted above soft magnetic pillars, but with spectrum overlaps of separated MBs, resulting in a reduced separation efficiency.<sup>26</sup> The separating motion of different size single MBs,<sup>65</sup> and recently, the separation of paramagnetic and diamagnetic MBs<sup>32</sup> was achieved on hexagonal arrays of magnetic bubble domains.

In this work, the controlled directed motion along an array of circular MSs is shown (Sec 4.2.1). A 2-D hexagonal distribution of MSs facilitates the movement of single MBs and their populations along hexasymmetric magnetic pathways on the chip surface. However, a simultaneous multilateral motion of multiple size MBs for their easy separation is very challenging due to the following reasons:

**Firstly**, since MBs show different MPM depending on their size around a single circular MS (Sec. 3.3), the applied  $H_{ext}$  for the directed MB motion along an array of circular MSs is expected to be different for different sizes of the MB. The motion of the MB with a diameter equaling the distance among circular MSs is achieved with the optimized amplitudes and angular asymmetries of an in-plane rotating  $H_{ext}$ . We label the  $H_{ext}$  optimization an order, i.e.  $1^{st} H_{ext}$ , which enables the MB motion along an array of MSs. The motion of a MB with a smaller or larger diameter becomes difficult on these hexagonal MSs. This requires individual  $H_{ext}$  optimization orders for the directed motion of smaller ( $2^{nd} H_{ext}$ ) and larger MB ( $3^{rd} H_{ext}$ ). Now, the underlying  $4^{th}$  order of  $H_{ext}$  optimization ( $4^{th} H_{ext}$ ) can be determined to move three different size MBs at the same time.

**Secondly**, as the order of driving  $H_{ext}$  is adjusted relative to  $4^{th} H_{ext}$  to enable the separation of MBs, the magnetic heterogeneous response of MBs largely dominates.

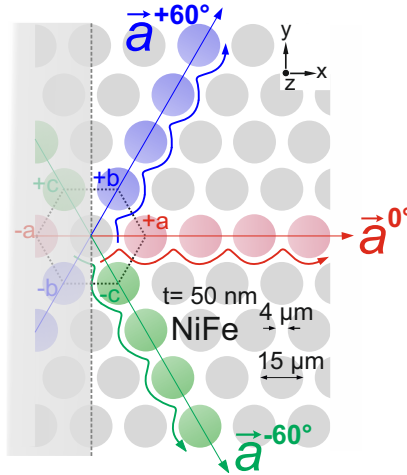
This causes instead a random MBs' motion. This problem is solved by analyzing the degree of heterogeneity for each MB size and attaining an order out of it ( $5^{\text{th}} H_{ext}$ ).

**Thirdly**, even with the  $5^{\text{th}}$  optimized order of  $H_{ext}$  for the simultaneous separation, it remains difficult to keep the laterally moving small, medium and large MBs on their separating paths, because they are moving in their transition regimes. The effect of surface imperfections increased there, too.

Yet, with definite strengths and offsets, an in-plane elliptically rotating  $H_{ext}$  drives a single MB through a precise spatio-dynamical control on the magnetization states of hexagonally arranged NiFe disks. The changing magnetic domain states of soft disk patterns generate the varying stray magnetic field gradient at the MS's interface, through which the MB can be moved along a disk-array. The resultant varying MB speed directly relates to its varying angular phase lag around the disk, which is adjustable with  $H_{ext}$  optimizations. Matching orders of  $H_{ext}$  optimizations facilitate the separation of multiple size MBs, due to their different MPM (see eq. 1.19).

## 6.1 Hexasymmetric Magnetic Surface

A sketch of a 2D hexagonal arrangement of 50 nm thin disk shaped NiFe magnetic structures (MSs) in Fig. 6.1 highlights the threefold vertex symmetry (colored arrays) on a sixfold (vertex and edge symmetry) pattern scheme. A horizontal array of the closely spaced structures as a reference direction  $\vec{a}^{0^\circ}$  (red array), together with two neighboring arrays ( $\vec{a}^{+60^\circ}$ , blue array and  $\vec{a}^{-60^\circ}$ , green array) provide magnetic pathways for the trilateral directed movement of magnetic MBs along discrete MSs. The diameter of the MS is  $15 \mu\text{m}$  with an inter-structure spacing of  $4 \mu\text{m}$ .



**Figure 6.1:** A sketch of 2D hexagonal arrangement of 50 nm thick NiFe structures indicates a threefold vertex symmetry (colored arrays) on a sixfold (vertex and edge symmetries) pattern scheme. Three exemplary pathways for a moving particle are shown along  $\vec{a}^{0^\circ}$  (red array),  $\vec{a}^{+60^\circ}$  (blue array) and  $\vec{a}^{-60^\circ}$  (green array). The diameter of magnetic structures and the inter-structure spacing are indicated.

## 6.2 Trilateral Motion of a Microbead

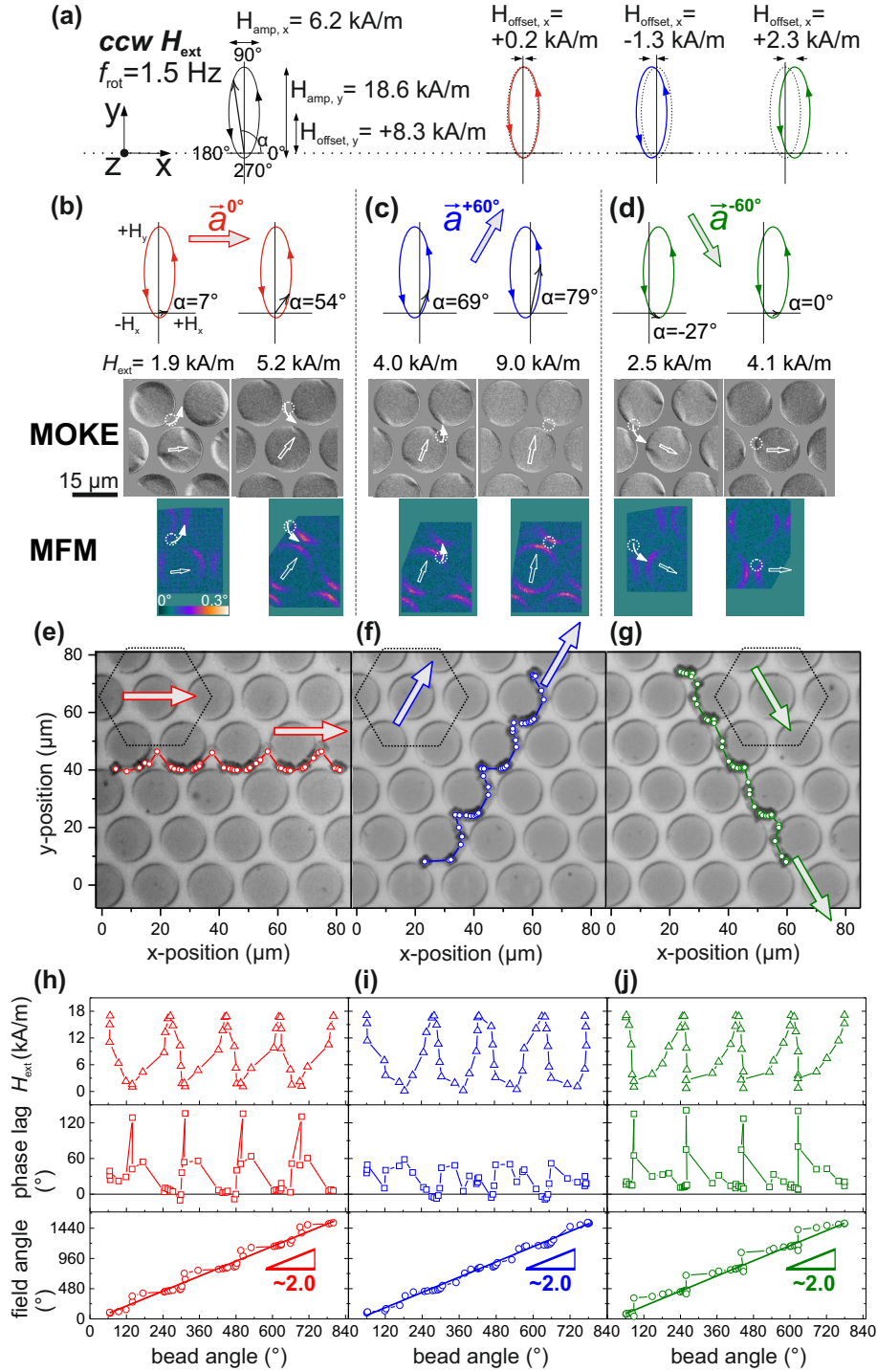
An in-plane rotating  $H_{ext}$  with varying strength moves the magnetic MB asymmetrically along the changing magnetization states of disk arrays. Depending upon the MB starting position and the instantaneous orientation and strength of  $H_{ext}$ , the MB may follow the moving magnetization of the disk (strongly magnetized) or it may lag behind (weakly magnetized). This lagged behind position of a moving bead can be utilized for its hopping to its neighboring disk under the time-varying  $H_{ext}$  for a directed motion along the disk array. Basically, the MB movement pattern is composed of alternative circulating and hopping motion.

Fig. 6.2 a shows a sketch of a counter clockwise rotating applied magnetic field (ccw  $H_{ext}$ ) with a fixed field frequency of 1.5 Hz and different in-plane amplitudes,  $H_x=6.2$  kA/m and  $H_y=18.6$  kA/m. A large field offset ( $H_{offset,y}=+8.3$  kA/m) in +y-direction further increases the field asymmetry to change the magnetization states of the disk arrays with the time-varying  $H_{ext}$ . Fixing the field offset along the vertical plane and changing the offset along the horizontal plane (Fig. 6.2 a), provides the off-centered elliptically rotating  $H_{ext}$  configurations with low-order ( $H_{offset,x}=+0.2$  kA/m, red) and high-order asymmetries ( $H_{offset,x}=-1.3$  kA/m, blue and  $+2.3$  kA/m, green) required for the selectable trilateral movement of the MBs.

MB directed motion along a disk array is achieved through the controlled hopping of a moving particle from one structure to the next. For a rotating field with  $H_{offset,x}=+0.2$  kA/m a moving bead with  $4\ \mu\text{m}$  diameter is hopped in  $\vec{a}^{0^\circ}$  direction at the changing field orientations  $\alpha$  from  $7^\circ$  to  $54^\circ$  with respective lower and higher amplitude of  $H_{ext}$  (Fig. 6.2 b). At the equal static conditions of  $H_{ext}$ , MOKE imaging of 50 nm thick NiFe magnetic patterns reveals the respective weakly and strongly (onion domain state) magnetized states. MFM imaging performed at a height of 500 nm over the magnetic structures describes the expected lower and higher magnitude of the field gradient FG, which causes MB hopping in  $\vec{a}^{0^\circ}$  direction due to its delayed angular position with respect to the disk magnetization.

For the MB movement in  $\vec{a}^{+60^\circ}$  direction, it is driven with an increased field offset along the x-axis ( $H_{offset,x}=-1.3$  kA/m), as indicated in Fig. 6.2 c. The magnetized onion domain states of disks are determined at  $H_{ext}=4.0$  kA/m and 9.0 kA/m with the respective coarse and fine distribution at the opposite edges of disks along  $H_{ext}$ . As indicated Fig. 6.2 c, the MB is also positioned along the  $H_{ext}$  orientation at the disk perimeter. Already lagging behind the field orientation  $\alpha = 69^\circ$ , the MB is hopped to the next disk due to its increased delay ( $\alpha = 79^\circ$ ) relative to the rotating  $H_{ext}$ . MFM images exemplify its hopping towards the near reaching stronger FG.

To move the bead in the  $\vec{a}^{-60^\circ}$  direction, the offset ( $H_{offset,x}=+2.3$  kA/m) of the rotating  $H_{ext}$  is increased in opposite direction (+x-axis), as shown by the exemplary results in Fig. 6.2 d. The MB is hopped from the weakly magnetized state of a disk to the strongly magnetized state of the next disk under  $H_{ext}$  changing from  $\alpha = -24^\circ$  to  $\alpha = 0^\circ$  with the amplitude from 2.5 kA/m to 4.1 kA/m. At equal  $H_{ext}$  conditions, the MB hopping motion towards the higher FG is depicted on MFM maps.



**Figure 6.2:** (a) An off-centered elliptical  $H_{ext}$  with varying  $x$ -axis offsets for the trilateral motion (b-d) of a  $4 \mu\text{m}$  bead. Changing magnetization states (MOKE images) and the varying magnitude of stray magnetic field gradients (MFM images) of NiFe disks depict the hopping motion of MB at corresponding static field conditions of the rotating  $H_{ext}$ . (e)-(g) Motion paths of MB in  $\vec{a}^{-0^\circ}$ ,  $\vec{a}^{+60^\circ}$  and  $\vec{a}^{-60^\circ}$  directions. (h)-(j)  $H_{ext}$  amplitude, angle and the phase lag of MB plotted versus bead angle determine the features of motion under the time-varying  $H_{ext}$ . Slopes between the field and bead angles represent a half MB's circulation for one rotation of ccw  $H_{ext}$ .

Fig. 6.2 e-g show the exemplary trilateral travelled paths of the bead under respective x-axis offsets of an elliptical  $H_{ext}$ . To maintain the direction of moving beads on these closely packed magnetic structures, a periodicity in the movement patterns must be attained, which is determined by plotting the salient features of motion in Fig. 6.2 h-j. Composed of alternative circulating and hopping movement patterns, the trilateral transport of a  $4\ \mu\text{m}$  bead is disclosed by plotting the asymmetrically varying field amplitude (kA/m), field angle  $\varphi_H$  ( $^\circ$ ) and phase lag  $\Delta$  ( $^\circ$ ) vs. the bead angle  $\varphi_{MB}$  ( $^\circ$ ) for corresponding directions.

Alternating decreasing and increasing  $H_{ext}$  drives the bead along in  $\vec{a}^{0^\circ}$  with the alternating rotational ( $\varphi_{MB} \approx$  from  $60^\circ$  to  $120^\circ$ ) and hopping motion patterns ( $\varphi_H \approx$  from  $180^\circ$  to  $240^\circ$ ) as shown in Fig. 6.2 h. For the low strength of rotating  $H_{ext}$ , the moving bead halts during the field rotations, which causes a large phase lag,  $\Delta > 130^\circ$  between the field and bead angular positions around the disk. During the higher strength of rotating  $H_{ext}$ , the bead follows the field rotations closely ( $\Delta \approx 10^\circ$ ) despite its occasional pinning at the structure's interface. Pinning of the moving bead and then the negative phase lag ( $\Delta < 0^\circ$ ) occur due to the competing stray fields at structure's interface, when the higher amplitude of rotating  $H_{ext}$  has its instantaneous orientation parallel to the magnetic array.

MB movement in  $\vec{a}^{+60^\circ}$  direction as cumulative MB angle under the slower decreasing and faster increasing  $H_{ext}$  is shown in Fig. 6.2 i. The moving MB stops ( $\Delta \approx 60^\circ$ ) at the low strength of  $H_{ext}$  and then moves forward on the same disk under the fast changing  $H_{ext}$ , which results in a reduced phase lag ( $\Delta \approx 10^\circ$  at  $\varphi_{MB} \approx 240^\circ$ ). After the hopping motion, the MB starts rotational motion on the next pattern ( $\Delta \approx 0^\circ$ ).

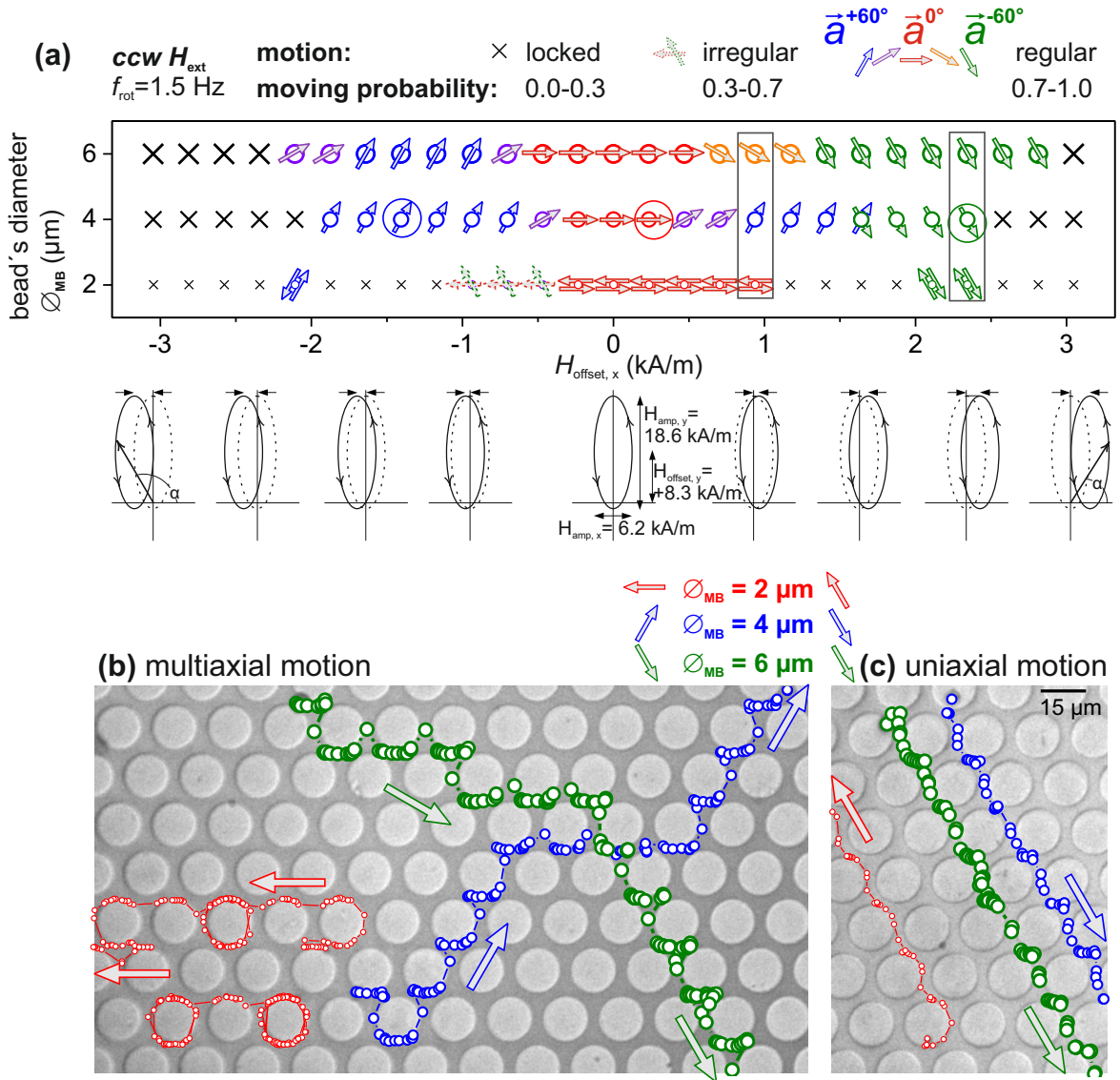
The MB's periodic dynamics in the  $\vec{a}^{-60^\circ}$  direction is shown in Fig. 6.2 j under faster decreasing and slower increasing  $H_{ext}$ . Starting its motion at  $\varphi_{MB} \approx 60^\circ$ , MB is partially rotated around the disk, but then it is stopped at low amplitude  $H_{ext}$ , which results in a larger phase lag  $\Delta > 120^\circ$ . For the higher strength of time-varying  $H_{ext}$ , the MB hops to the next disk and then it is driven along the magnetized state of the disk under the increasing strength of  $H_{ext}$ . The MB completes its periodic motion in the  $\vec{a}^{-60^\circ}$  direction and  $\Delta$  reduces again for the field orientation being parallel to the magnetic array. The controllable motion of a  $4\ \mu\text{m}$  MB in three lateral directions is shown in Appendix-E.1.4 Movie 6.1 to Movie 6.3.

### 6.3 Trilateral Separation of Multiple Size Microbeads

Changing the x-axis offset of an elliptical rotating  $H_{ext}$  can drive the microbeads along multiple arrays on this hexalateral magnetic surface. Directed motion of MBs can be locked at the extreme x-axis offsets. To realize the simultaneous separation of multiple size MBs, the response of simultaneously moving MBs was analyzed with a comprehensive experimental study. A phase diagram in Fig. 6.3 a summarizes the motion behavior of MBs with  $2\ \mu\text{m}$ ,  $4\ \mu\text{m}$  and  $6\ \mu\text{m}$  diameter versus the changing x-axis offsets ( $H_{offset,x}$ ) of an asymmetrically rotating in-plane  $H_{ext}$ .



For largely off-centered fields such as  $H_{offset,x} = -3.1$  and  $+3.1$  kA/m, MB's directional motion is locked by the incomplete circulating motion and the exclusion of hopping motion. In consequence, the beads move back and forth at the perimeter of the single disk. Shifting the elliptically rotating  $H_{ext}$  towards horizontal origin opens the trilateral pathways for the directed movement for a  $4 \mu\text{m}$  bead (encircled values). Large MBs with  $6 \mu\text{m}$  exhibit similar response, except a little wider regime for the directional motion which is attributed to their larger magnetic volume. Small  $2 \mu\text{m}$  diameter MBs with the low magnetic volume are difficult to transport across neighboring structures at the presently applied  $H_{ext}$  conditions. Yet, it is possible to obtain their regular movement at specific  $H_{ext}$  offsets, as indicated in Fig. 6.3 a.



**Figure 6.3:** Phase diagram summarizes the motion response of MBs with  $2 \mu\text{m}$ ,  $4 \mu\text{m}$  and  $6 \mu\text{m}$  diameter versus changing  $H_{offset,x}$  of an elliptically rotating  $H_{ext}$  on the hexalateral magnetic surface. Regimes of the motion and motion probability are indicated. Exemplary results for the simultaneous multiaxial (b) and uniaxial (c) motion of MBs are presented.

Using the size of MBs as a control parameter, a window of asymmetrically rotating  $H_{ext}$ , enabling the separating motion is disclosed. Single MBs with three different sizes can be simultaneously moved in three lateral directions (indicated in Fig. 6.3 a). For certain  $H_{ext}$  asymmetries, three different MBs can be simultaneously guided along a single axis on the magnetic chip. This indicates the significance of experimentally determined fifth order of the  $H_{ext}$   $5^{th}$   $H_{ext}$  which includes the optimized amplitudes in the x-y plane, their ratio and the angular asymmetry of  $H_{ext}$ . Depending on the MB's initial position on the magnetic structures, small  $2 \mu m$  beads might trap at the opposite magnetic potential of the disk. This results in a motion in the opposite direction along the other side of the same array.

Indeed, an elliptically rotating  $H_{ext}$ , with its adjustable asymmetry with respect to hexagonal magnetic arrays at the chip plane is able to drive small, medium and large MBs in a single and multiple directions. Time-varying field gradients around NiFe periodic disk arrays can control the motion of multiple size MBs simultaneously by compensating and differentiating their size dependent magnetophoretic mobility. Fig. 6.3 b and c show the exemplary trajectories of  $2 \mu m$ ,  $4 \mu m$  and  $6 \mu m$  diameter MBs for their uniaxial (for  $H_{offset,x} = +2.3$ ) and multiaxial motion (for  $H_{offset,x} = +0.9$ ). See Appendix-E.1.4 Movie 6.4 and Movie 6.5.

## Discussion

The efficient separation of single magnetic MBs on a chip, being a problem,<sup>5</sup> becomes even more difficult for multiple MBs due to the magnetic and surface imperfections. To solve this problem, the circular magnetic structures (MSs) in square<sup>66</sup> and hexagonal<sup>65</sup> periodicity were employed with various sequences of applied magnetic fields. Nonlinear (frequency dependent) dynamics of MBs limits the separation efficiency,<sup>4</sup> because of the mutual effects of inherent magnetic asymmetry of hard magnetic patterns and the magnetic heterogeneity of the MBs, together with unfavorable size combinations of MB and MS.<sup>66</sup> Provided by the complex control parameters, a separation window of a few degrees hinders the simultaneous separation of different sized MBs.

In the application context, the on-chip separation efficiency<sup>26</sup> is still far below than the flow based technique<sup>4,67</sup>. This is likely due to the separating motion of differently labeled MBs along the same pathway. Increasing the throughput requires fast speed motion of MBs, which leads to the agglomeration of MBs. Ideally, separating MBs should not hinder each others motion for the whole populations. This is possible with a hexalateral magnetic surface, where MBs can be sorted in different directions with a control on single moving MBs.

In this work, we show that the MB separating motion is achievable during its linear motion (low frequency regime). The flexibility in controlling the magnetization states of soft magnets opens the room for the strength and orientation adjustments of an in-plane rotating  $H_{ext}$ . This facilitates a control on the MB motion with high resolution in space and time. After achieving the directed motion along a single magnetic array

under the working rotational frequency of  $H_{ext}$ , the motion along six-fold symmetric pathways is possible. For a continuously driving  $H_{ext}$ , a magnetic particle can be steered along all six magnetic paths (Appendix-D.4). This confirms the complete functionality of this magnetic surface. Effects of slight uniaxial magnetic anisotropy in NiFe disk structures were not observed to impair the MB motion.

For a continuously driving  $H_{ext}$ , a magnetic particle with a single movement pattern does not help in the separation of different particles. Nor, a different size particle will spontaneously move in the same path or will take a separating path, because the applied magnetic fields are not programmed to manipulate the particles selectively. Therefore, to enable the particle separation along freely moving  $H_{ext}$ , first the multiple movement patterns have to be determined.

A moving particle, showing three distinct movement patterns with the adjustable offsets of the rotating  $H_{ext}$  is a model system (Appendix-D.1). The controlled trilateral motion of a magnetic particle ( $4\ \mu m$ ) lays the foundation for multiple particles sorting. At an optimized configuration of the rotating  $H_{ext}$ , a simultaneous separating motion of three different size particles is realizable (Appendix-D.2). This manipulation platform is equally applicable to separate the same size magnetic particles, relying on their different magnetic content. In the presented manipulation technology, the size dependent different response of MBs during their transition from the linear to nonlinear motion offers the separation opportunities, controlled by the applied frequency of  $H_{ext}$  (Appendix-D.3).

## Summary

Using an off-centered in-plane rotating  $H_{ext}$ , the directed MB motion can be achieved on a hexalateral magnetic chip. The changing strength, orientation and speed of an elliptical rotating  $H_{ext}$  enables a spatiodynamical control on the magnetization states of soft periodic MSs. Stray magnetic field gradients varying in time and space at the structure's interface are able to move the MBs along magnetic arrays. Using the size of magnetic MBs as a control parameter, a simultaneous motion of three different MBs is achievable in three lateral directions. From the regime of MBs locked motion to their steering along multiple pathways a control on MBs transport is simplified with an in-plane elliptically rotating  $H_{ext}$ . A solution for the sorting of magnetic MBs driven along the traveling magnetic potential energy landscape on a chip has been provided.

## Chapter 7

# Magnetic Manipulation of a Social Amoeba (Cells)

The manipulation of a single molecule facilitates the study of a complex multi-protein system inside a biological cell.<sup>68-70</sup> Understanding the interaction among the molecules, proteins and genes inside living cells provide information about the pathological state of cells, which can be helpful for timely drugs and therapies, for example in the case of tumorigenesis.<sup>71</sup> On the other hand, the controllable position, transport and separation of the whole cell on a microchip are primary requirements for research and biotechnological applications.<sup>4,5</sup>

Owing to the possibility of 3-D tracking and sub-nanometer spatial resolution, optical tweezers have become a mature tool for the manipulation of living cells.<sup>68,70</sup> Despite the use of magnetic MBs as an isolation carrier of molecules and proteins from the cell (immunomagnetic purification), MB-based manipulation could not receive much attention in the field of cell mechanics. Using optical tweezers, providing the 3-D control on the MB inside the cell, was the preferred analysis method.<sup>68</sup> However, magnetic manipulation still enables the intracellular analysis, which is limited with optical tweezers.<sup>68</sup> Because of the contrasting refractive index in complex sub-cellular structures, optical tweezer can not always operate selectively.<sup>70-72</sup> The application of externally applied magnetic fields, just selective to the magnetic MBs without interference to the biological system, makes it an ideal tool for investigations of living cells with a control on the single molecule.<sup>68</sup>

In vivo analysis of biomolecules inside a cell with magnetic tweezers rely on microrheology, where a single MB (as a magnetic probe) attached with the molecules exerts the forces and enables their measurements on these molecules within the cell.<sup>71,72</sup> Forces from a few pN<sup>71</sup> to hundreds of pN,<sup>72</sup> were generated inside a *Dictyostelium* cell. The viscoelastic response of the cell was determined through the force measurements of MBs by fitting the modeled data with experiments.<sup>71</sup>

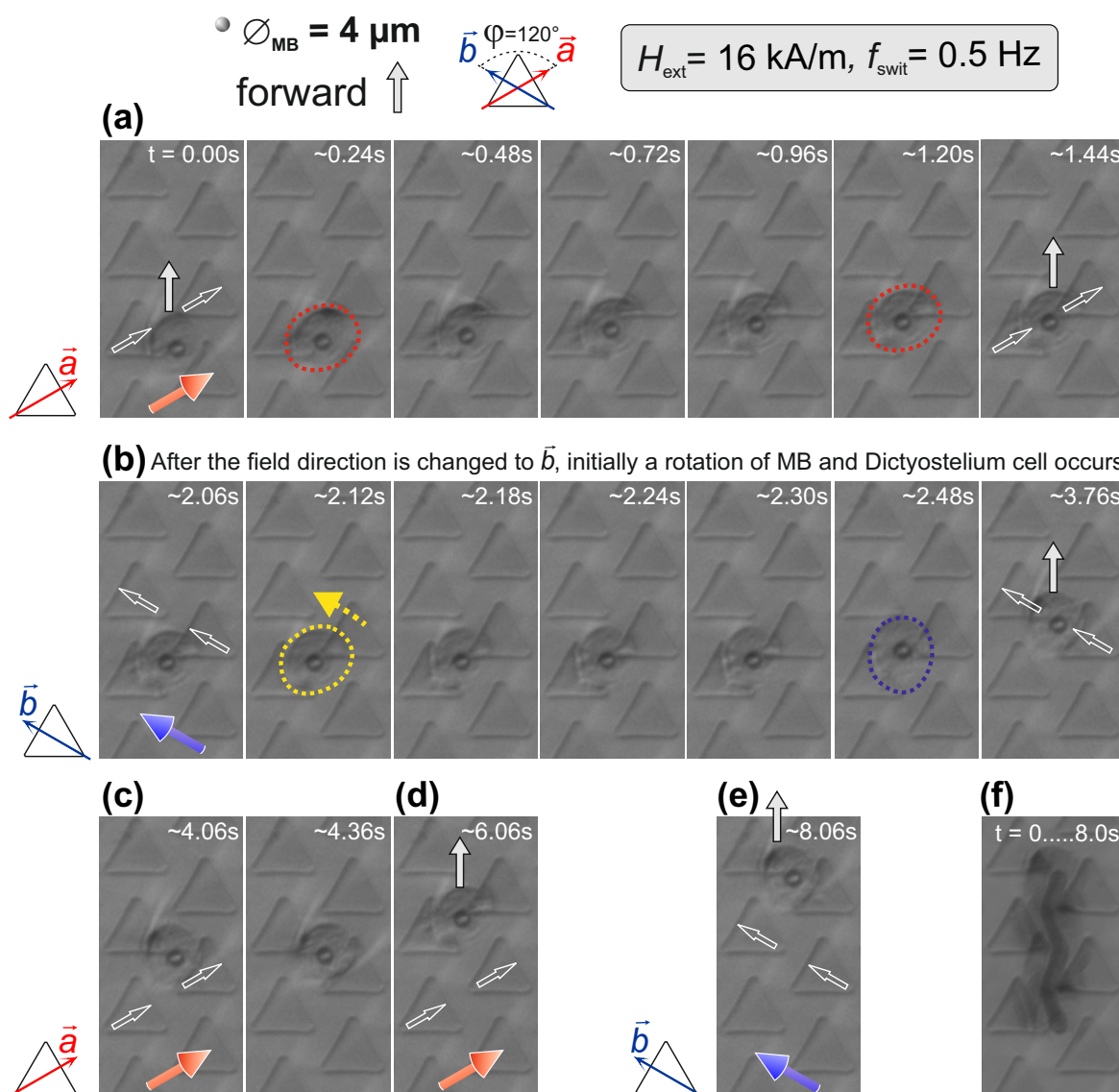
Unlike prokaryotic cells (e.g. bacteria), eukaryotic cells have a complex subcellular structure, multiple organelles for the associated functions, thus have their own

metabolism system. *Dictyostelium discoideum* (aka social amoeba or slime mold) is a eukaryotic organism with a size of 10-20  $\mu\text{m}$ .<sup>69</sup> Due to its accessibility, *Dictyostelium* is known as a conventional model to study fundamental cellular processes in cell biology and physiological studies.<sup>69,73</sup> The complete information of its genome sequence and genetic tractability makes it a valuable model organism for the treatment of infectious diseases caused by pathogens (bacteria or viruses). Such an infection model promotes a systematic analysis of infection-relevant host cells on a molecular level by phagocytosis (engulfing of a solid particle by the cell).<sup>69</sup> With the unknown functions, 41 genes are reported that are common in humans and in *Dictyostelium*.<sup>69</sup> Similar measurement results on motor proteins in *Dictyostelium* and human cancer cells<sup>70</sup> further validate the scope of *Dictyostelium* as a model organism for the fundamental knowledge about genetic and neurological diseases.<sup>69,70</sup>

In the last years, the research on the magnetic manipulation of *Dictyostelium* focused either on its intracellular investigations<sup>61,68,71,72</sup> or on the migration of cell aggregations.<sup>73</sup> At the same time, a free and controllable transport of the whole *Dictyostelium* cell, providing a platform to perform intracellular studies on a magnetic chip has not been shown yet to our knowledge.

In this chapter, a proof of concept for the directed movement of a *Dictyostelium* cell is presented. A single MB with 4  $\mu\text{m}$  diameter, engulfed inside the cell is moved forward on the surface of trisymmetric NiFe magnetic structures under the similar magnetic field conditions as used for the MB alone. Fig. 7.1 shows the exemplary response of a forward moving *Dictyostelium* cell at a magnetic field  $H_{ext}$  changing its direction between  $\vec{a}$  and  $\vec{b}$  with a switching frequency  $f_{swit} = 0.50$  Hz. Starting with the MB position at a vertex of a triangular magnetic structure MS, it follows the field direction  $\vec{a}$  by moving towards the field gradient FG at the MSs' interface. With the apparent fix position inside the *Dictyostelium* cell, the forward movement of the MB occurs through the FG at the edge of the MS, until it reaches the next vertex as shown in Fig. 7.1 a. (see Sec. 5.1.2).

Since the applied  $f_{swit}$  of the field was kept below the critical frequency of the MB carrying the *Dictyostelium* along, the MB waits for the inverted FG on changing the field direction from  $\vec{a}$  to  $\vec{b}$ . Fig. 7.1 b shows the next movement step. Since the *Dictyostelium* cell is dragged along with MB on the magnetic surface during its motion, it effects the MB movement in return. Positioned symmetrically at the MSs' interface, the MB is under the simultaneous effect of forward and backward FG. For its directed motion, it must find a biased field gradient on the hexagonal magnetic energy landscape. As the field direction is changed to  $\vec{b}$ , MB initially rotates around its own axis and then is moved to the FG at the next vertex. With the observed fix position of the MB inside the *Dictyostelium* cell, the MB's rotation naturally rotates also the cell. Fig. 7.1 b indicates the cell rotation by its initial (yellow encircled) and final position (blue encircled) before the forward motion. The origin of MB's self rotation is unknown. Fig. 7.1 c-e shows repeating movement steps for the changing position of  $H_{ext}$ . A complete record of the transport is shown in Fig. 7.1 f. See Appendix-E.1.5 Movie 6.1.



**Figure 7.1:** Micrographs show the exemplary forward motion of a Dictyostelium cell with a  $4 \mu\text{m}$  diameter MB, engulfed inside the cell. (a) For the field direction  $\vec{a}$ , the MB moves forward to the field gradient at the structures' interface. (b) On switching the field to  $\vec{b}$ , initially a self rotation and then the directional motion occurs. (c)-(e) Repeating steps of forward motion under the changing direction of external magnetic field  $H_{ext}$ . The amplitude and switching frequency of  $H_{ext}$  are labeled. (f) A full record of motion is shown. The MB and cell positions are indicated by upward arrows, before and after their directed movements.

## Discussion and Summary

Magnetic structures-based magnetic tweezers on the chip surface provide the local magnetic forces at the level of a single cell. Using the arbitrary signal of  $H_{ext}$ , the stray magnetic field gradient on MSs are fully controllable in time and space to manipulate the target analytes. It is possible to control the position and motion of a biological organism with a magnetic microparticle, engulfed inside it on a magnetic microchip.

The presented example of a forward moving *Dictyostelium* cell in Fig 7.1 provides a basic insight. The fix position of MB inside the cell during the transport of MB-cell conjugate is understood as the effective magnetic force on the MB, which is high enough for the directed motion on the magnetic surface, however, still low to cause a displacement of MB at the intracellular level. Control experiments show that the MB is movable inside the cell only at high amplitude magnetic field, e.g. 80 kA/m. Naturally, the achievable maximum speed of the MB, translocating the cell along, decreased drastically due to the different hydrodynamic conditions. Experiments reveal that an approx.  $6\times$  to  $10\times$  reduction in the critical frequency  $f_{crit}$  of an engulfed MB occurs when compared to the  $f_{crit}$  of the mere MB. Interestingly, the lower strength of  $H_{ext}$  (e.g. 4 and 8 kA/m) is already sufficient to induce the magnetic forces on the MB for the actuation of *Dictyostelium*. Experiments performed on large engulfed MBs (8  $\mu\text{m}$  diameter) indicate that the MSs should be placed more distant on the chip to facilitate the lateral movement of *Dictyostelium*.

# Chapter 8

## Conclusions and Outlook

The controlled motion of microparticles enables the transport, separation and diagnostics of magnetically labeled biological molecules on a microchip. However, the progress and implementation of a magnetic chip based LoC device is highly dependent on the separation of differently labeled analytes. Together with a reproducible movement of single magnetic particles, a highly efficient separation of different types of particles is challenging on a chip surface. Particularly, the problem of separating the mixed populations of particles, resulting in the purity of the separation protocol, did not receive much attention.

Suspended in a few  $\mu\text{l}$  aqueous medium, superparamagnetic-microbeads SPM-MBs have been freely moved and separated on the surface of magnetic microchips during this thesis. Lithographically deposited soft micromagnetic structures allow the control in their magnetization domain state with an externally applied in-plane magnetic field  $H_{ext}$ . Using the geometry of MSs together with various amplitudes and orientations of  $H_{ext}$ , the separating motion of mixed MBs has been achieved at a single MB and population level by a direct control on the magnetization states and thus, on the magnetic field gradient FG landscapes on soft MSs.

**Chapter 3** An accurate response of a single moving MB was confirmed by simulating the MB movement patterns for its linear and looping motion, while taking the exact micromagnetic configuration of the bead moving structure and the distribution of iron oxide nanoparticles inside the bead into account. The understanding of the increased magnetic force on the moving bead for the increased amplitude of  $H_{ext}$  has been achieved. The effect of shape and size of the MS on the speed of MBs was determined. Small disks with  $30\ \mu\text{m}$  diameter provide  $\approx 2\times$  higher speeds of MBs than on rings and disks with  $60\ \mu\text{m}$  diameter. The heterogeneous magnetic response of single MBs has been quantified for the population for MBs with diameter varying from  $2\ \mu\text{m}$  to  $12\ \mu\text{m}$  in their high speed regime (i.e. critical frequency).

For the MB transport along a magnetic track MT, a compromise among the MB diameter, size and geometry of MT and the strength of applied magnetic field  $H_{ext}$  has been found for the maximum achievable average velocity  $v_{ave}$ . An approx.  $2\times$  increase



(decrease) in the  $v_{ave}$  is achievable through the particle continuous (looping) motion by changing the rotational frequency  $f_{rot}$  of in-plane  $H_{ext}$ . Using the diameter of magnetic particles as a control parameter, an approx.  $2\times$  higher/lower critical frequency  $f_{crit}$  is revealed on various MTs. This makes it possible to move the different size MBs approx.  $2\times$  faster or slower due to their dissimilar magnetophoretic mobility MPM on the MT.

The practical implementation of these magnetic tracks will require design optimizations to block the particles' motion along the other side of the track. If the adjusted field frequency  $f_{rot}$ , distinguishing the MBs size dependent critical frequency  $f_{crit}$ , will be applied, then one sided magnetic pathways (e.g. zigzag or curvilinear) will transport the large MBs with a faster speed than the small MBs under a rotating  $H_{ext}$ , similar to concentric tracks.<sup>25</sup> The applied  $f_{rot}$  differentiating the continuous and looping (or locked) motion of mixed populations of MBs, resulting in their separable velocities will enable the particle filtering. For immunomagnetic separation of biological cells, the sizes of magnetic particles will be chosen as a compromise between MPM and the antibody binding capacity.<sup>74</sup>

**Chapter 4** The directed motion of the MBs on 1-D arrays MAs of symmetric (asymmetric) magnetic structures with an asymmetrically (symmetrically) in-plane rotating  $H_{ext}$  has been realized. Independent of the starting position, a unidirectional control on the MBs motion is achievable on arrays of egg-shaped FeCoSiB MSs. On the 1-D arrays of disk-shaped NiFe MSs, the directed motion of MBs has been obtained with elliptically rotating  $H_{ext}$ .

With the advantages and disadvantages of both approaches, it is concluded that the choice of a manipulation method depends on the application. Basic insights have been provided for further research. Egg-shaped structures based magnetic arrays arranged in a network can converge the whole population of particles. This will enable particle counting and quantification with the integrated sensor. These egg-shaped arrays move the particles unidirectional with a  $v_{ave} \approx 100 \mu m/s$ . However, the spontaneous bidirectional motion at the high rotational frequency  $f_{rot}$  of  $H_{ext}$  limits the maximum achievable speed. Blocking the opposite directional motion will need the structures' optimization. The curvature difference at the structures' interface and the distance between structures are of most interest for the required high speed and directionality of MB's ensembles. 1-D arrays of disk-shaped NiFe MSs were extended to the 2-D magnetic surface for the particle separation.

**Chapter 5** A free and selectable movement of MBs is achievable on NiFe triangular trisymmetric magnetic structures on the chip. With the MB size dependent differently confined positions, the underlying movements for a simultaneous two-way motion have been revealed. Using the selective amplitude and sequence of an in-plane square wave  $H_{ext}$ , the populations of different MBs have been selectively moved from a heterogeneous mixture with a separation efficiency of  $>97\%$ .

Eliminating the dependence on ensemble averaging (the conventional tool, e.g. flow cytometry), trisymmetric magnetic surfaces facilitate the high degree separation with a simultaneous control on single MBs and their populations. Together with a high

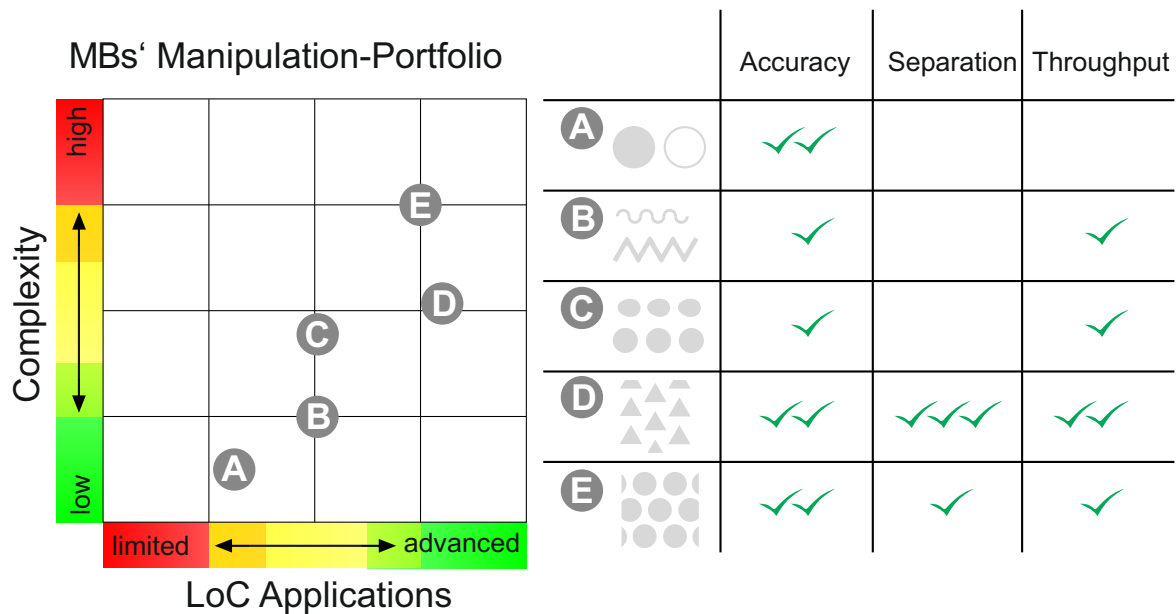
throughput, this leads to accurate and fast diagnostics. This 2-D magnetic surface has a bright scope for the multilateral separation of mixed MBs with multiple populations. This will require further research on the optimization of geometric and magnetic parameters of the existing scheme. Multiple biological analytes, labeled to different types of MBs will be sortable at required areas on the microchip. With the triangular structure geometry, these magnetic arrays are adaptable to an arbitrary structural network for the integration of possible functions, e.g. counting, collecting and sensing of magnetically tagged biological entities along with flowing suspension<sup>75</sup> on a single chip. Furthermore, this platform is also compatible with the label free cell manipulation through negative magnetophoresis.<sup>76</sup> A proof-of-concept for the motion of MBs' doublets and triplets, as shown in Appendix-C.4, highlights the scope of 2-D trisymmetric magnetic surface for movable magnetic MBs' carpet<sup>77</sup> and for the arrangement and assembly of MBs<sup>15</sup> on the chip surface.

**Chapter 6** A controlled directed motion of the complete population of MBs has been realized on the NiFe disk-shaped hexasymmetric magnetic structures HMSs with an applied  $H_{ext}$ , asymmetrically rotating in the chip plane. Simply adjusting the amplitude and orientation asymmetry of elliptical  $H_{ext}$  along one axis opens the possibility of single MBs' steering along trilateral magnetic arrays. MBs with three different sizes have been simultaneously moved in three lateral directions with a common sequence of elliptically rotating  $H_{ext}$ . Demonstrated for the first time, the separating motion of multiple magnetic particles at a single MB level highlights the scope of soft magnetic hexagonal surfaces. Enabling the efficient separation of multiple populations MBs will require future research on following aspects: distance optimization between the MB moving circular magnetic structures, use of MBs with other sizes and higher magnetic content, improvement in the sequence of  $H_{ext}$ .

Similar to flow-based MBs separation by magnetic deflection,<sup>67</sup> multilateral movements will determine that the MBs' ensembles are separated apart. The efficiency will maximize with the elimination of overlapped histograms of multiple MBs' populations.<sup>26</sup> Like the programmable single MB manipulation,<sup>30,41,43,78</sup> a programmed scheme, composed of arbitrary sequences of elliptical  $H_{ext}$  will enable arbitrary movements on magnetic microchips. Initial efforts have disclosed the MBs size dependent motion. With a comprehensive understanding, the possibilities of advanced manipulation methods are explorable now.

**Chapter 7** The selectable transport of a *Dictyostelium* cell with a single magnetic MB inside it has been shown for the first time on a magnetic microchip. This will facilitate intracellular studies, based on the remotely controllable magnetic forces. To deal with the variation in results,<sup>71</sup> an analysis on the population of cells will provide the generally valid viscoelastic behavior. Determining the critical size with high magnetic content of the MB will increase magnetic forces. The role of magnetic structures for the force maximization is substantial. Studying the underlying physiological roles of single molecules and proteins on the cell functions will provide the fundamental knowledge about genetic and neurological diseases.<sup>69,70</sup>

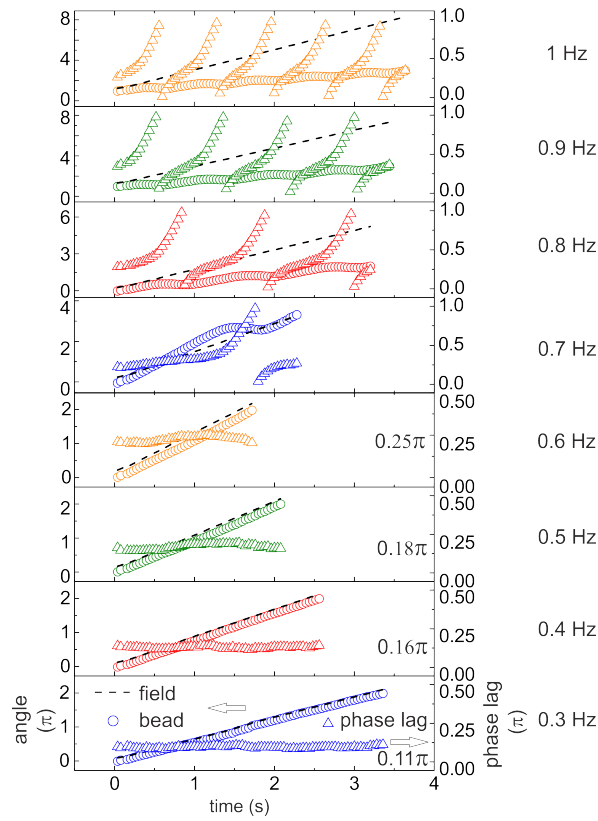
**Final Words** An accurate motion of a magnetic microbead ensures its reproducible and reliable transport on the microchip surface. Achieving quantitative understanding of the beads' populations confirms their accurate separation. A MBs' manipulation portfolio shown in Fig. 8.1 depicts the LoC functionalities achieved on various micromagnetic structures investigated in this thesis. A high throughput (MB  $v_{ave} \approx 0.1$  mm/s) is realizable for the MB's guided motion on a 1-D magnetic pathway. Freely moving different beads on a 2-D triangular surface can be separated simultaneously as well as selectively. The separation of MBs' populations is possible with high efficiency. MBs' populations can be transported with a high throughput (MBs  $v_{ave} \approx 0.12$  mm/s). On symmetrically patterned magnetic surface the separation of three different size beads is realizable at a single bead level.



**Figure 8.1:** MBs' manipulation portfolio shows the attainable functionalities vs. the level of manipulation complexity on various magnetic surfaces presented in this thesis.

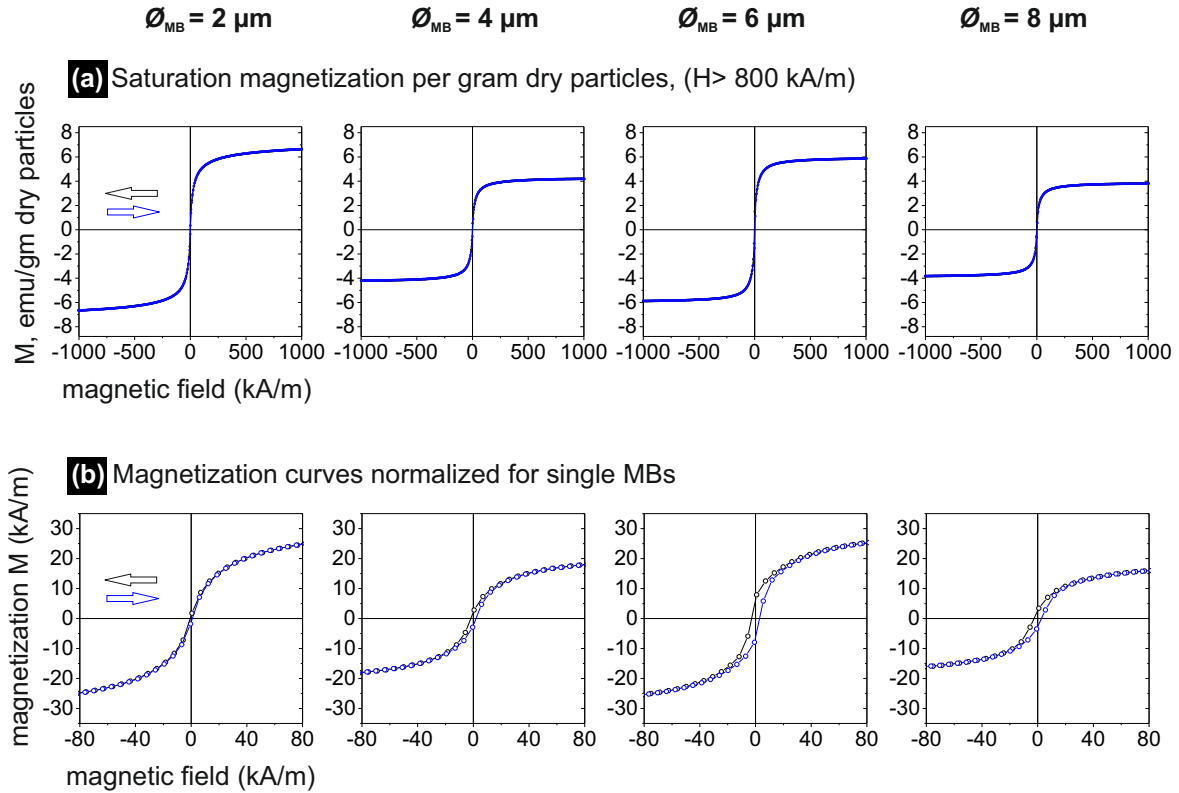
# Appendix-A

## A.1 Phase Lag Dependence on the Speed of a Microbead



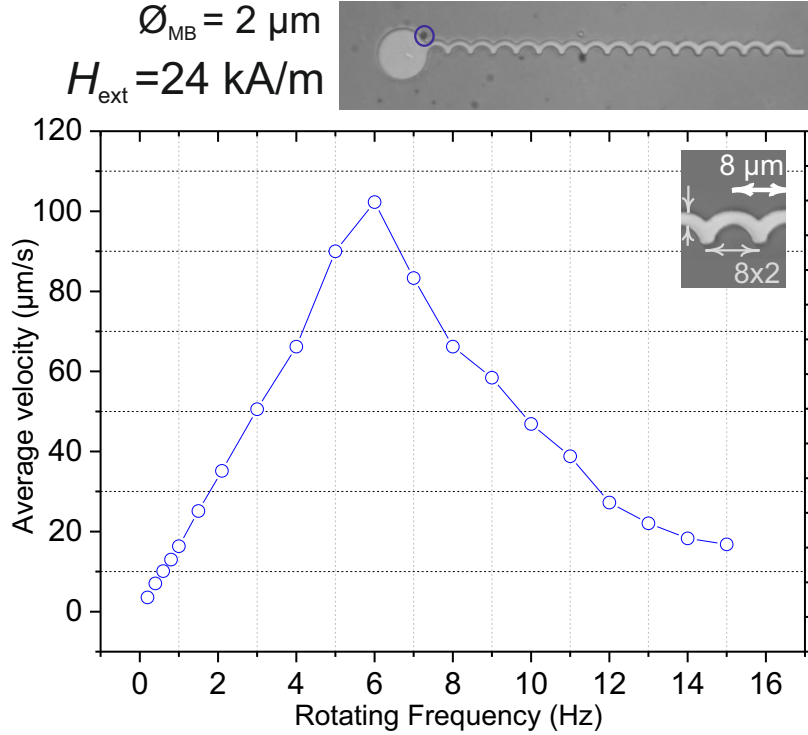
**Figure Appendix-A.1:** Field angle, bead angle, and phase lag are plotted versus time for an  $8\ \mu\text{m}$  diameter bead. The time required for one complete rotation of the bead around a disk with  $30\ \mu\text{m}$  diameter is shown for varying rotational frequencies of a homogeneously rotating in-plane magnetic field. For the analogous motion, the amplitude of MB's phase lag increases with increasing the rotational field frequency. An approx. phase lag of  $0.11\pi$ ,  $0.16\pi$ ,  $0.18\pi$ , and  $0.25\pi$  is experimentally determined for the respective field frequencies of 0.3, 0.4, 0.5, and 0.6 Hz. For the field frequency above 0.6 Hz, an alternating tear-off and recapture of the bead result a periodic looping motion. See also Fig. 3.4

## A.2 Normalized Magnetization of Single Microbeads with Different Sizes



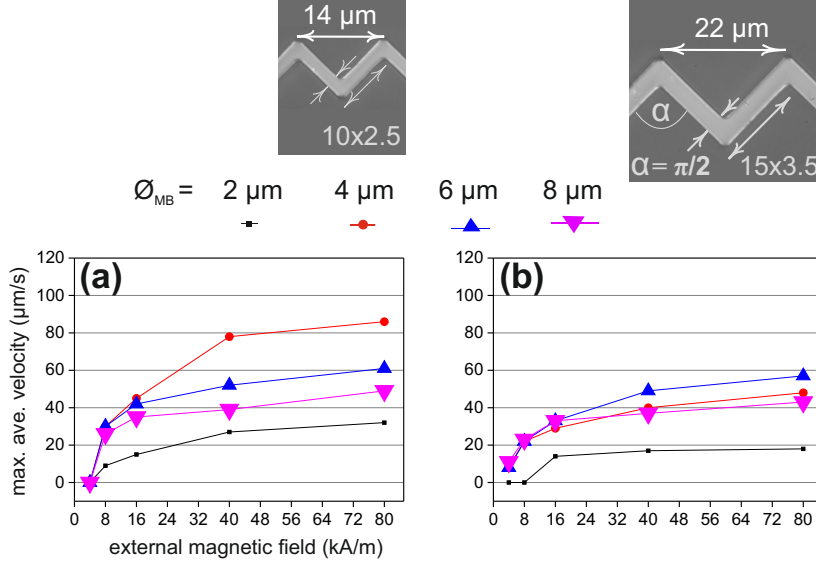
**Figure Appendix-A.2:** (a) Ensemble averaged magnetization curves provided by Micromod, measured by the vibrating sample magnetometer (VSM) on approximately  $3.36 \cdot 10^9$  particles. (b) Magnetization (kA/m) is calculated from (a,  $M$  in emu/g) with the approximated magnetic content for the single MB in mass and volume (shown in Fig. 3.5 c). Then, the numerical differentiation of magnetization results in the susceptibility  $\chi$  for single MBs with corresponding sizes, as listed in Fig. 3.5 c. The origin of the coercive field by MBs with diameter,  $\varnothing_{MB} = 4 \mu\text{m}$ ,  $6 \mu\text{m}$  and  $8 \mu\text{m}$  is unknown. However, no effects of these coercive fields were observed at the single MB level during the experiments.

### A.3 Linear Increase and Decrease in the Velocity of a MB



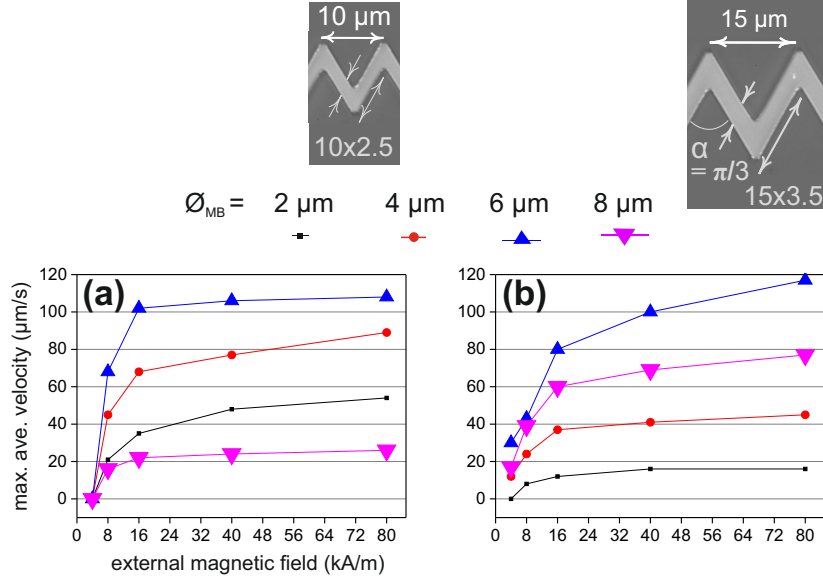
**Figure Appendix-A.3:** Average velocity of a  $2 \mu\text{m}$  bead during its directed motion on a convex magnetic track MT. A linear increase and decrease in the velocity is determined around its critical frequency  $f_{\text{crit}} \approx 6 \text{ Hz}$ . After the  $f_{\text{crit}}$  of MB, the reduced  $v_{\text{ave}}$  from the looping motion at higher rotational frequencies of  $H_{\text{ext}}$  is equivalent to the  $v_{\text{ave}}$  during MB's continuous motion at lower field frequencies due to the small period length of the MT. In effect, similar speeds can be achieved in the regimes of continuous and looping motion with a factor of  $f_{\text{rot}}$ , e.g. 4 and 8 Hz produce the similar  $v_{\text{ave}}$ . Dimensions of MT and the amplitude of  $H_{\text{ext}}$  are indicated.

## A.4 $H_{ext}$ Amplitude defining the MB's Velocity on Zigzag Tracks with $\alpha = \pi / 2$



**Figure Appendix-A.4:** MBs' size dependent average velocity ( $v_{ave}$ ) around their critical frequency  $f_{crit}$  for different amplitudes of an in-plane rotating magnetic field. (a) MBs start moving at the threshold amplitude of  $H_{ext}$  (8 kA/m). On the increased amplitude of  $H_{ext}$ , the nonlinear increase in  $v_{ave}$  is related to the dissimilar magnetophoretic mobility MPM of different MBs. (see eq. 1.19). At high magnetic fields ( $H_{ext} = 40$  kA/m and 80 kA/m), the small increment in  $v_{ave}$  is due to the magnetic saturation of MBs. For magnetic fields below the threshold limit (e.g.  $H_{ext} = 4$  kA/m), the weak field gradient FG at the next tip could not actuate the MB. Meanwhile, the FG at the opposite tip across the track width attracts the MB, which hinders the directed motion (b) As discussed in 3.4.5, the larger distance between the MB moving magnetic features (tips) causes a reduced MPM of particles. Large MBs are movable already at  $H_{ext} = 4$  kA/m, due to the wider track. MB sizes and lateral dimensions of NiFe magnetic tracks are indicated in  $\mu\text{m}$ . The tracks are 30 nm thick.

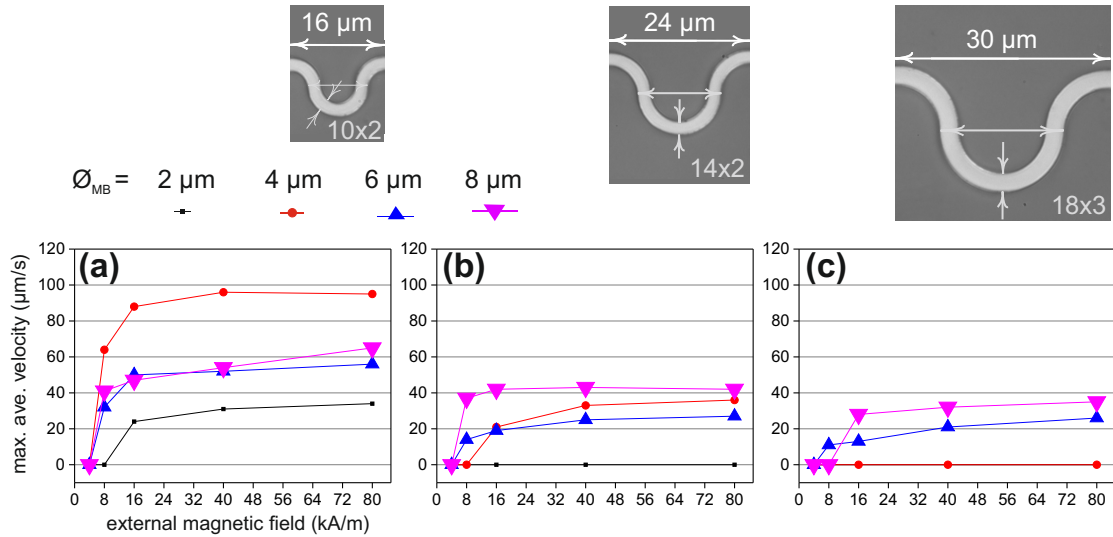
## A.5 $H_{ext}$ Amplitude defining the MB's Velocity on Zigzag Tracks with $\alpha = \pi / 3$



**Figure Appendix-A.5:** MBs' size dependent average velocity ( $v_{ave}$ ) around their critical frequency  $f_{crit}$  for different amplitudes of an in-plane rotating magnetic field. (a) MBs start moving at the threshold amplitude of  $H_{ext}$  (8 kA/m). On the increased amplitude of  $H_{ext}$ , the nonlinear increase in  $v_{ave}$  is related to the dissimilar magnetophoretic mobility MPM of different MBs. For large MBs with 6 μm and 8 μm diameters, almost no increase in  $v_{ave}$  for  $H_{ext}$  increased from 16 to 80 kA/m is due to a size restrain, as discussed in 3.4.5. (b) Due to widely spaced tips on large tracks, large MBs show an increment in  $v_{ave}$ , explaining the effect of stronger field gradient FG at high  $H_{ext}$ . Small MBs show lower  $v_{ave}$  on large tracks, again due to the size restrain, as discussed in 3.4.5. MB sizes and lateral dimensions of NiFe magnetic tracks are indicated in μm. The tracks are 30 nm thick.

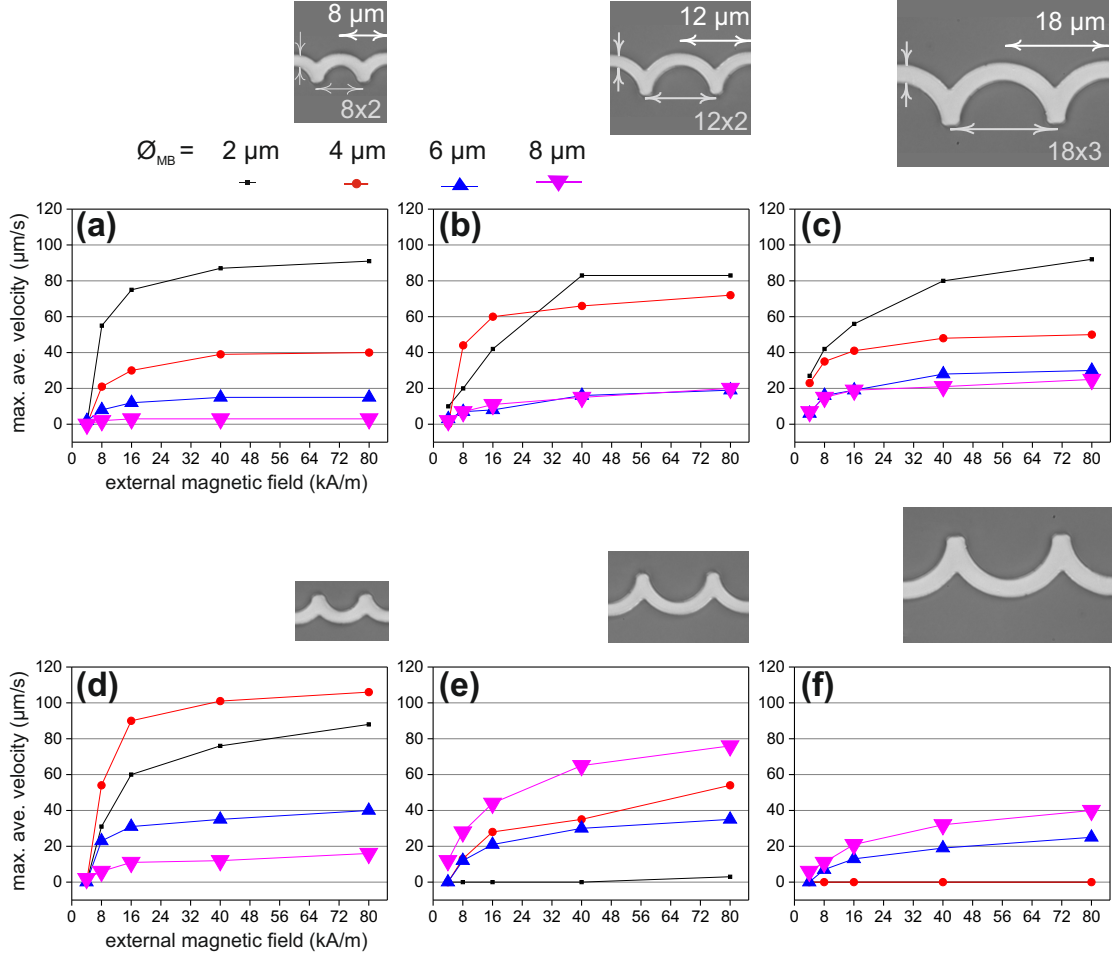


## A.6 $H_{ext}$ Amplitude defining the MB's Velocity on Curvilinear Tracks



**Figure Appendix-A.6:** MBs' size dependent average velocity  $v_{ave}$  around their critical frequency ( $f_{crit}$ ) for different amplitudes of an in-plane rotating magnetic field ( $H_{ext}$ ). (a) Except 2 μm MB, others start moving at a threshold amplitude of  $H_{ext}$  (8 kA/m). On the increased amplitude of  $H_{ext}$ , the nonlinear increase in  $v_{ave}$  is related to the dissimilar magnetophoretic mobility (MPM) of different MBs. For the size optimization among the sizes of MB and MT, as discussed in 3.4.5, 4 μm with higher MPM move faster on small magnetic tracks. (b) Because of the widely spaced field gradient FG maxima on large track the directed motion of MBs is impaired. 2 μm beads remain immobile, even at high amplitude of  $H_{ext}$ . (c) Adverse effects on the motion of small MBs were observed. MB sizes and lateral dimensions of NiFe magnetic tracks are indicated in μm. The tracks are 30 nm thick.

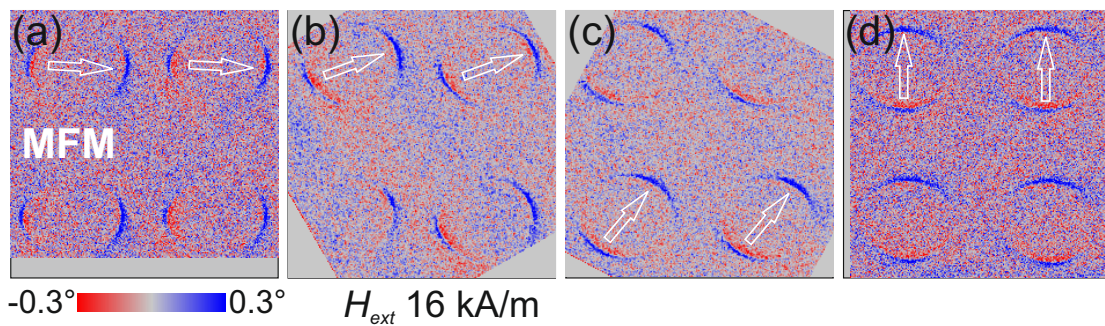
## A.7 $H_{ext}$ Amplitude defining the MB's Velocity on Convex and Concave Tracks



**Figure Appendix-A.7:** MBs' size dependent average velocity ( $v_{ave}$ ) around their critical frequency  $f_{crit}$  for different amplitudes of an in-plane rotating magnetic field. (a) MBs start moving at the threshold amplitude of  $H_{ext}$  ( $8\ \text{kA/m}$ ). On the increased amplitude of  $H_{ext}$ , the nonlinear increase in  $v_{ave}$  is related to the dissimilar magneto-phoeretic mobility MPM of different MBs. Due to the improper size combination between MB and magnetic track, as discussed in 3.4.5, smaller MBs move faster while larger move slower. (b) On the medium size convex track, the comparable values of MPM of  $2\ \mu\text{m}$   $4\ \mu\text{m}$  result from the best matching of MB size with the periodic length  $\lambda$  of track. (c) On the large convex track, directed motion of large MBs is slightly eased. Now, all MBs can move already at  $H_{ext} = 4\ \text{kA/m}$ , likely related to the track width. (d) Same large size MBs show higher  $v_{ave}$  on the concave track, which indicate the geometric effect of the magnetic structure. (e)-(f) Larger difference between the size of MB and  $\lambda$  of track causes the immobility of small MBs. The effect of track shape is evident. MB sizes and lateral dimensions of NiFe magnetic tracks are indicated in  $\mu\text{m}$ . The tracks are  $30\ \text{nm}$  thick.

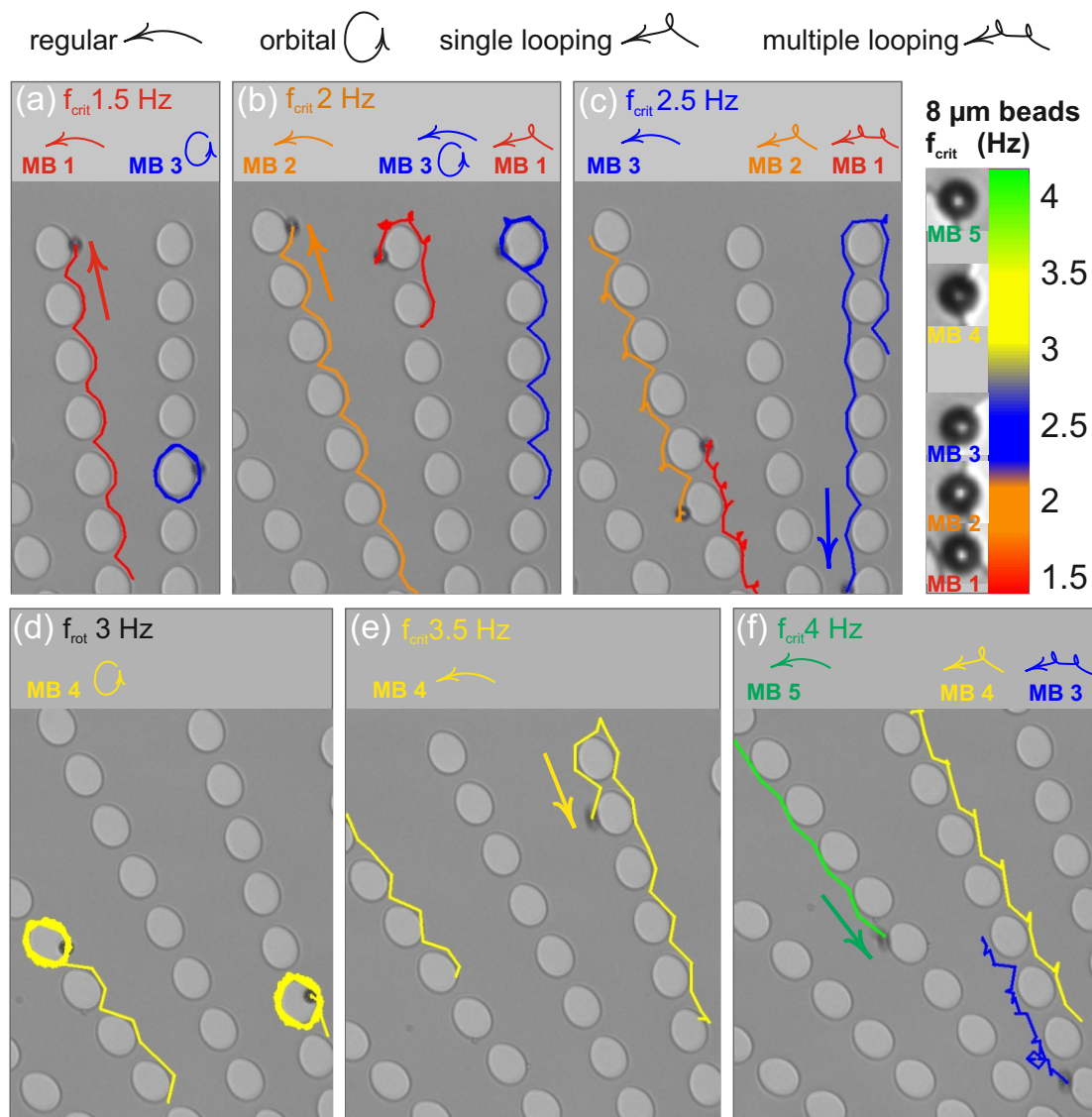
# Appendix-B

## B.1 MFM Imaging on Egg-shaped Magnetic Structures



*Figure Appendix-B.1: Stray field gradients for varying orientations of in-plane applied field. MFM maps were obtained at a height of 500 nm above the 50 nm thick FeCoSiB structures.*

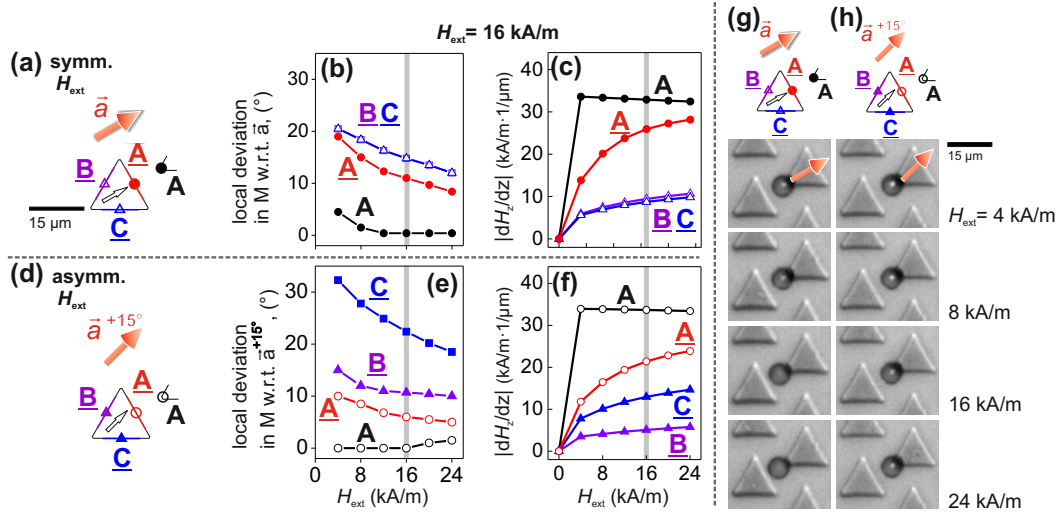
## B.2 Varying Critical Frequencies of Single MBs on a 1-D Magnetic Array



**Figure Appendix-B.2:** Different critical frequencies of single MBs determine the heterogeneous magnetic response of same type of MBs with 8  $\mu\text{m}$  diameter.

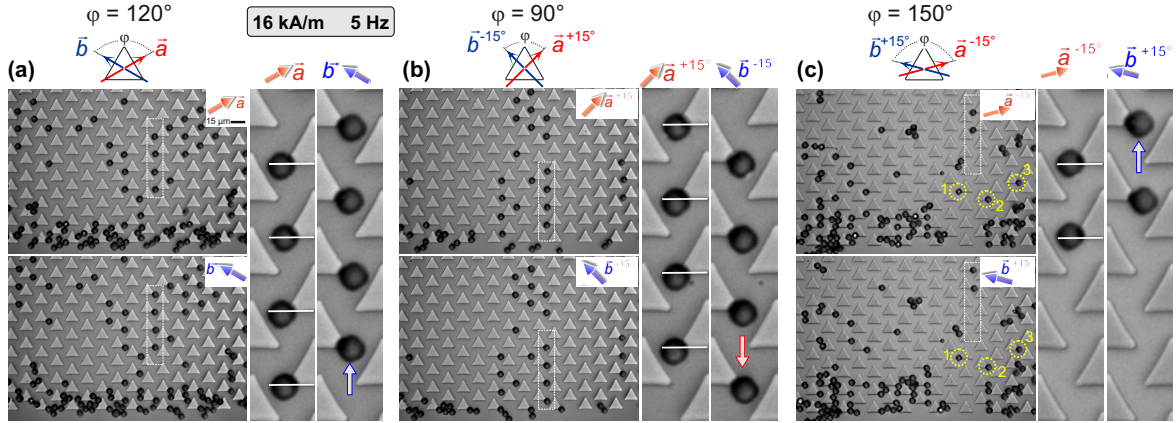
# Appendix-C

## C.1 Local deviation in Magnetization and the Resultant Field Gradient



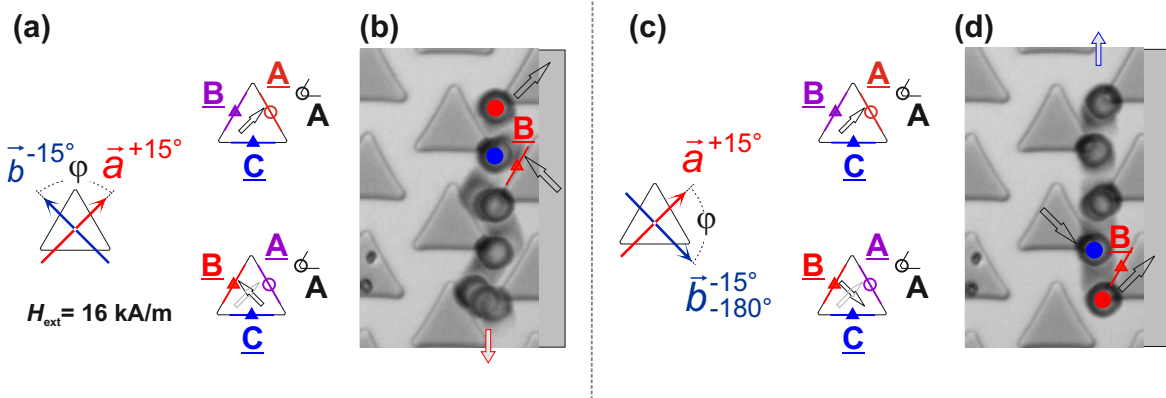
**Figure Appendix-C.1:** The simulated local deviation in the magnetization  $M$  orientation and resulting stray magnetic field gradient  $FG$  at a height of 500 nm above the 50 nm thick NiFe MSs under applied static fields ( $H_{ext}$ ) with the symmetric and asymmetric configuration. (a) The direction of a symmetric field  $\vec{a}$ .  $B$  and  $C$  represent the center of adjacent edges. (b) The small deviation in  $M$  at the vertex  $A$ , while the large deviations at the opposite and adjacent edges occur. (c) The magnitude of  $FG$  increases at the edges  $A$ ,  $B$  and  $C$  on increasing the strength of  $H_{ext}$ . At the vertex  $A$ , it reaches the saturation already at low strength  $H_{ext}$ . (d) An asymmetric applied field  $\vec{a}^{+15^\circ}$  with its direction becoming parallel to the edge  $B$  and perpendicular to the edge  $C$ . (e) The resultant decreased and increased deviation in the local  $M$  occurs at the edges  $B$  and  $C$  respectively. The magnetization at the opposite edge  $A$  now has twice a reduced deviation, comparing to its values for the symmetric field. (f)  $FG$ s with the consequent reduced magnitudes at the edges  $A$  and  $B$  and an increased magnitude at the  $C$ . (g)-(h) The stable position of a magnetic bead with 8 μm diameter under the increasing strength of  $H_{ext}$  for the symmetric and asymmetric  $H_{ext}$ . Reproduced from Ref. 64 with permission © 2018 Wiley-VCH.

## C.2 Motion of MBs' Ensembles under Symmetric and Asymmetric Fields



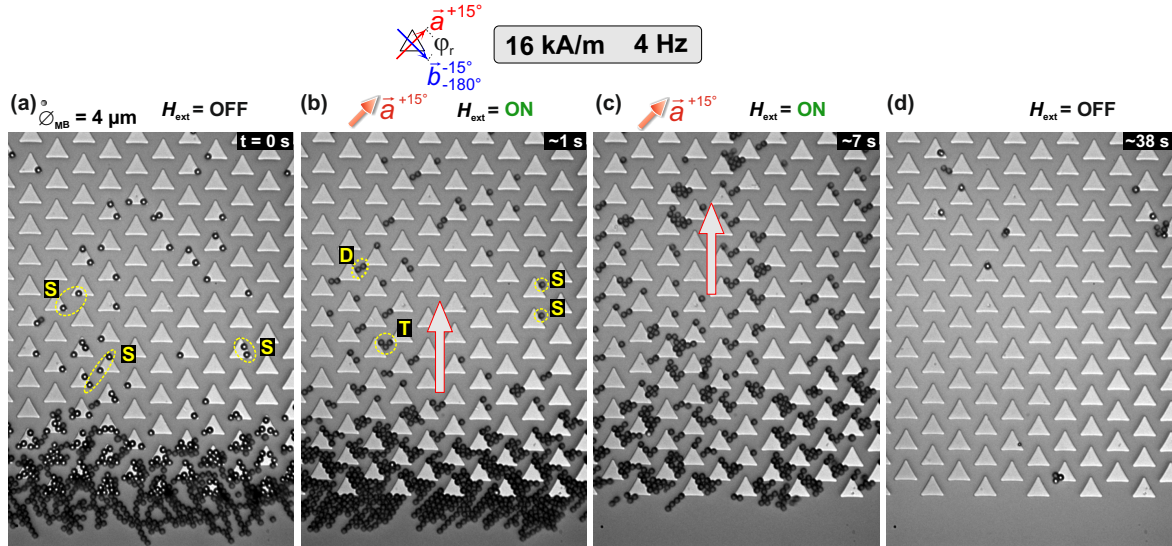
**Figure Appendix-C.2:** Micrographs show the stable positions of  $8 \mu\text{m}$  MBs during the forward motion under a symmetrically changing magnetic field with an opening angle  $\varphi = 120^\circ$ . (b) Downward shifted positions of the backward moving beads for an asymmetrically changing field with a small opening angle  $\varphi = 90^\circ$ . (c) Upward shifted positions of the beads. They move intermittently forward for the large opening angle  $\varphi = 150^\circ$  of an asymmetrically changing field. The intermittent motion is due to the distant field gradients at the structures' interface.

### C.3 Inversion of a MB's Directed Motion with an Inversion of Field Direction



**Figure Appendix-C.3:** (a)-(b) Curling backward movement of a MB with  $8 \mu\text{m}$  diameter under the applied magnetic fields changing between  $\vec{a}^{+15^\circ}$  and  $\vec{b}^{-15^\circ}$ . (c) Changing the orientation of the field state  $\vec{b}^{-15^\circ}$  by  $180^\circ$ , i.e.  $\vec{b}_{-180^\circ}^{-15^\circ}$  changes the sense of magnetization rotation and thus the resultant stray field gradients around the magnetic structures. The bead's directional motion from its initial position at the vertex of a single triangle (indicated red) is likely affected by the direction of changing magnetic field (indicated blue). Moreover, the magnetic field gradients from the adjacent structures are also expected to influence the direction of bead's motion. The backward moving beads are observed to move forward after inverting the field direction from  $\vec{b}^{-15^\circ}$  to  $\vec{b}_{-180^\circ}^{-15^\circ}$ . The exemplary response of this new (straight forward) path of MB's motion is shown in (d), comparing to the typical curling backward motion (b).

## C.4 MBs' High Yield Transport and Patterning Possibilities

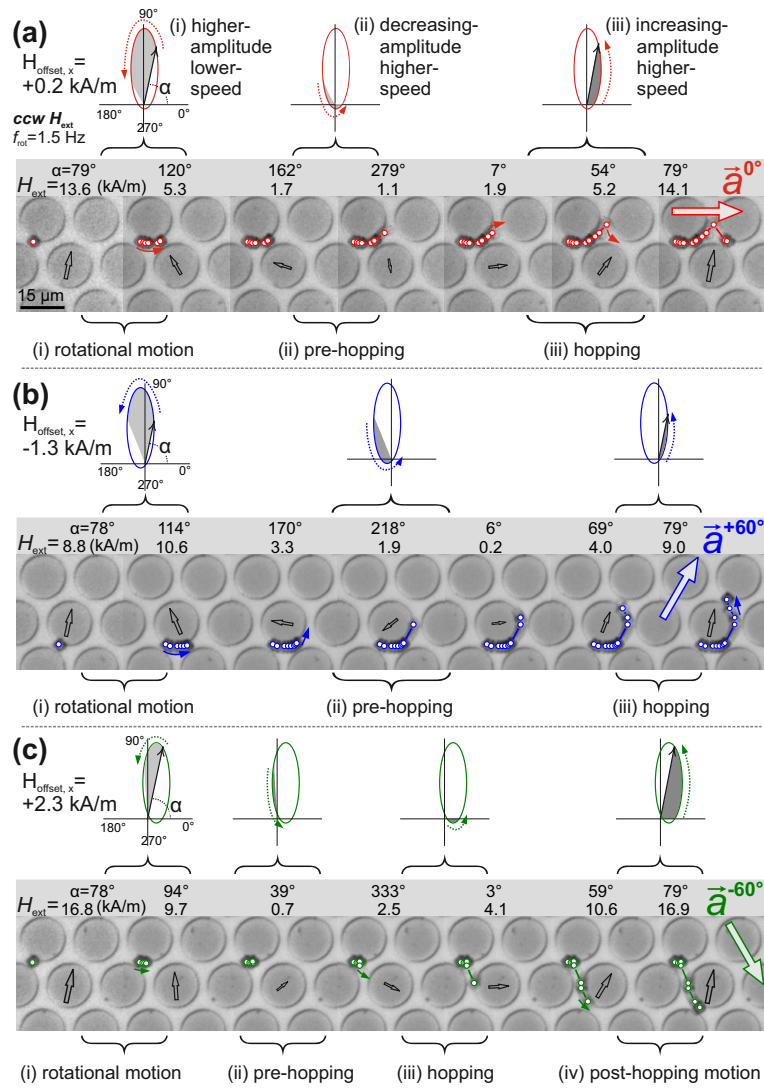


**Figure Appendix-C.4:** (a) Microbeads with  $4 \mu\text{m}$  diameter MBs, randomly dispersed at the magnetic boundary of the chip. (b) A static image of the forward moving beads shows their stable positions along the field direction. Depending on the initial position and local concentration of MBs, they move as singlets, doublets and triplets, which can be used for increased throughput of a process. (c) Asymmetrically changing magnetic fields with a switching frequency of  $4 \text{ Hz}$  transport the MBs' assemblies upward across the observation area, without any blockage through the magnetic pathways. (d) A complete transport is achieved in 38 seconds of the magnetic field application



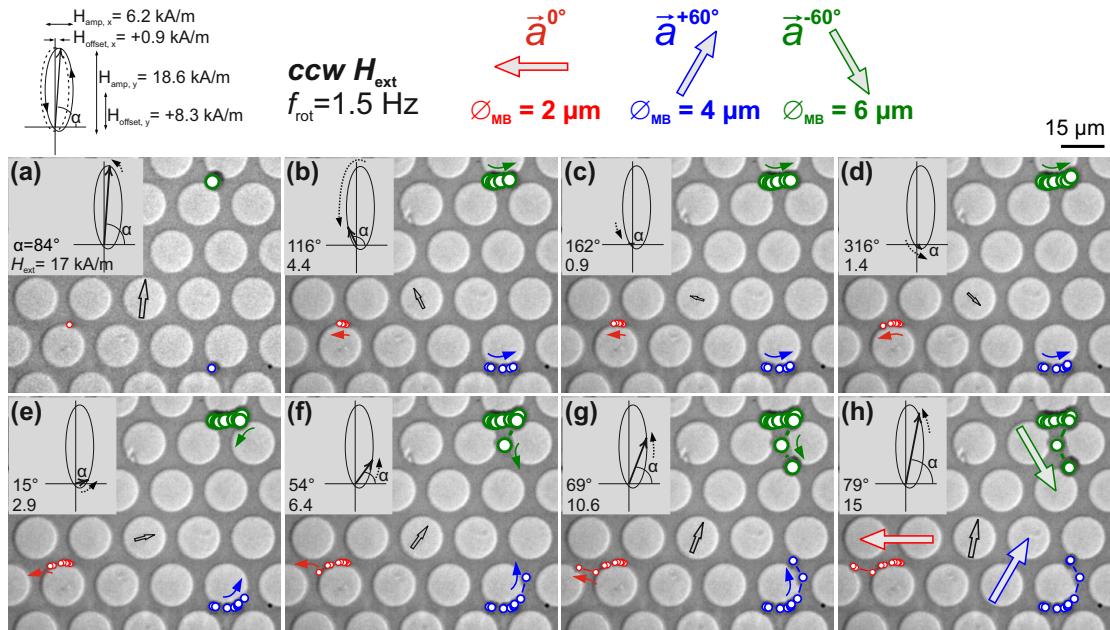
# Appendix-D

## D.1 Trilateral Movement Patterns of a MB



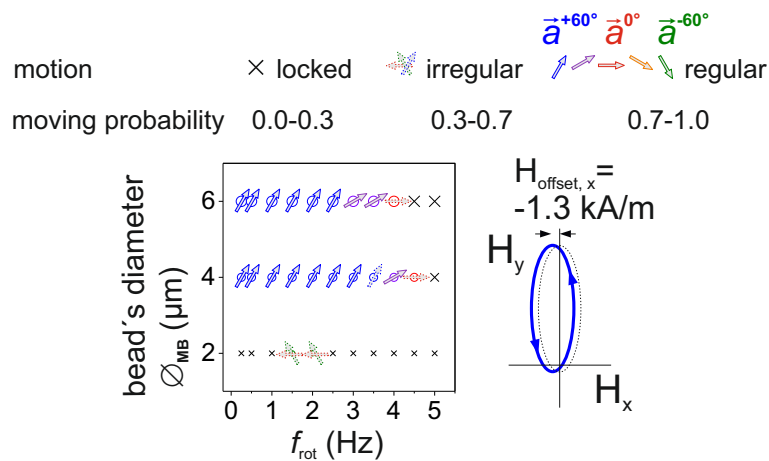
*Figure Appendix-D.1: An off-centered rotating  $H_{\text{ext}}$  with varying  $x$ -axis offsets for the trilateral motion of a  $4 \mu\text{m}$  bead. See also Fig. 6.2*

## D.2 Trilateral Separation of Multiple MBs



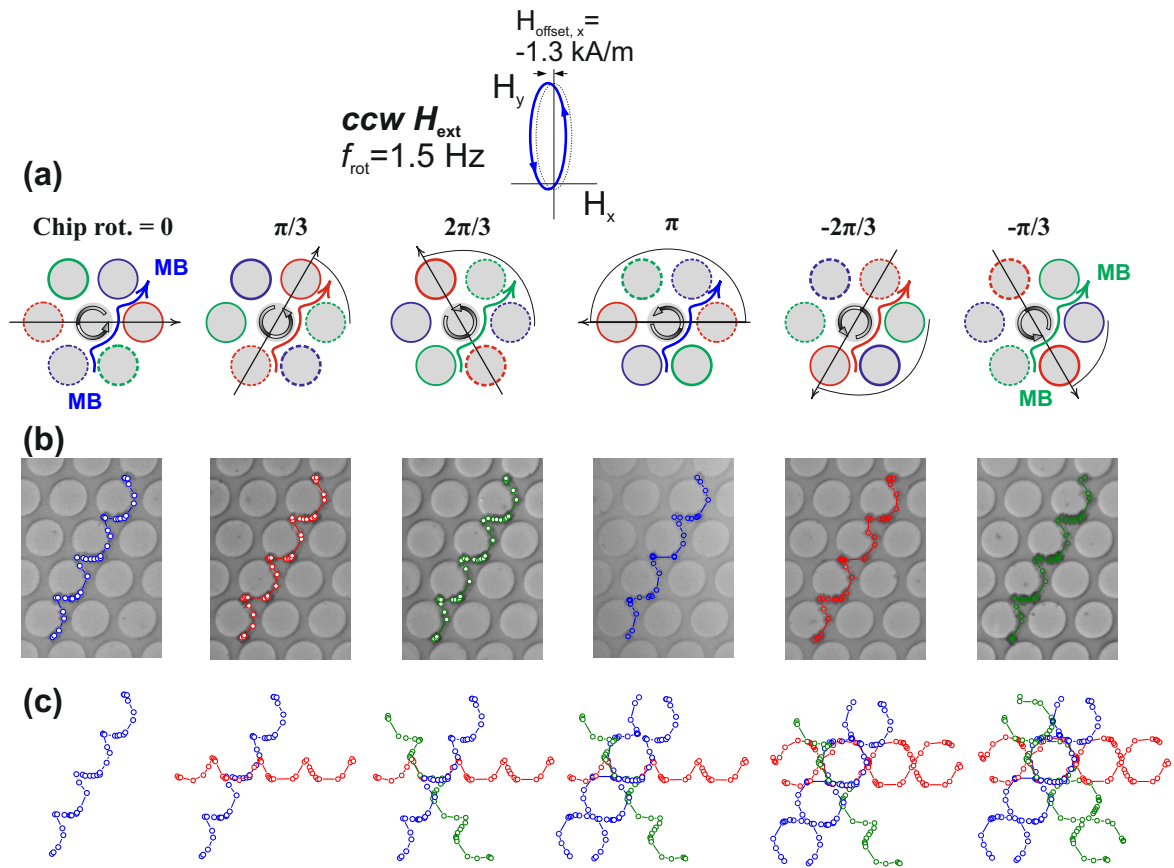
**Figure Appendix-D.2:** Simultaneous trilateral separating motion of MBs with  $2 \mu\text{m}$ ,  $4 \mu\text{m}$  and  $6 \mu\text{m}$  diameter. See also Fig. 6.3

## D.3 MBs' Motion Depending on the Rotational Frequency of Applied Field



**Figure Appendix-D.3:** Phase diagram shows the motion response of MBs with  $2 \mu\text{m}$ ,  $4 \mu\text{m}$  and  $6 \mu\text{m}$  diameters versus the varying rotational frequency of an elliptical rotating  $H_{\text{ext}}$  on the hexagonal magnetic surface.

## D.4 Hexalateral Motion for a MB based on the Chip Rotation



*Figure Appendix-D.4: A magnetic bead with  $4 \mu\text{m}$  diameter is movable along all six pathways of the magnetic surface with a fixed sequence of an elliptical rotating  $H_{\text{ext}}$ .*

# Appendix-E

## E.1 Movie Captions

### E.1.1 Movies-Chapter 3

**Movie 3.1** An  $8\ \mu\text{m}$  MB circulates continuously around a NiFe disk with diameter of  $30\ \mu\text{m}$  with a homogeneously rotating magnetic field with an amplitude of  $16\ \text{kA/m}$  at a frequency of  $0.6\ \text{Hz}$ . See also Fig. 3.3 and 3.4.

**Movie 3.2** The MB moves with a single looping at the field frequency above the critical frequency of the MB, i.e.  $0.7\ \text{Hz}$  for a homogeneously rotating magnetic field with an amplitude of  $16\ \text{kA/m}$ .

**Movie 3.3** At higher field frequency of  $0.9\ \text{Hz}$ , the MB shows multiple looping motion for a homogeneously rotating magnetic field with an amplitude of  $16\ \text{kA/m}$ .

**Movie 3.4** The number of loopings increases for an applied field with the reduced amplitude of  $8\ \text{kA/m}$ . The field has a fixed rotational frequency of  $0.9\ \text{Hz}$ .

**Movie 3.5** Loopings occur with a larger number on further reduced field amplitude of  $4\ \text{kA/m}$ . The field has a fixed rotational frequency of  $0.9\ \text{Hz}$ . See also Fig. 3.3 and 3.4.

**Movie 3.6** The MB moves with a drastically slow speed at a rotational frequency of  $10\ \text{Hz}$  of the rotating magnetic field with an amplitude of  $16\ \text{kA/m}$ .

**Movie 3.7** The continuous and looping transport of a MB with  $2\ \mu\text{m}$  diameter is shown on a NiFe curvilinear track for the respective rotational frequency of  $1.5$  (below its critical frequency) and  $2.0\ \text{Hz}$  (above its critical frequency) of a rotating magnetic field with an amplitude of  $16\ \text{kA/m}$ . See Fig. 3.8. The MB transport is controllable with an approx.  $2\times$  decrease in its speed during the periodic looping motion, as shown in Tab. 3.1.

**Movie 3.8** The continuous and looping transport of a MB with  $4\ \mu\text{m}$  diameter is shown on a curvilinear track for the respective rotational frequency of  $2.7$  and  $3.0\ \text{Hz}$  of a rotating magnetic field with an amplitude of  $16\ \text{kA/m}$ .

**Movie 3.9** The continuous and looping transport of a MB with  $6\ \mu\text{m}$  diameter is shown on a curvilinear track for the respective rotational frequency of 1.5 and 1.7 Hz of a rotating magnetic field with an amplitude of 16 kA/m.

**Movie 3.10** The continuous and looping transport of a MB with  $8\ \mu\text{m}$  diameter is shown on a curvilinear track for the respective rotational frequency of 1.5 and 1.7 Hz of a rotating magnetic field with an amplitude of 16 kA/m.

**Movie 3.11** The continuous and looping transport of a MB with  $2\ \mu\text{m}$  diameter is shown on a NiFe Zigzag track for the respective rotational frequency of 0.45 and 0.50 Hz of a rotating magnetic field with an amplitude of 16 kA/m. See Fig. 3.10. The MB transport is controllable with an approx.  $2\times$  decrease in its speed during the periodic looping motion, as shown in Tab. 3.2.

**Movie 3.12** The continuous and looping transport of a MB with  $4\ \mu\text{m}$  diameter is shown on a Zigzag track for the respective rotational frequency of 1.20 and 1.30 Hz of a rotating magnetic field with an amplitude of 16 kA/m.

**Movie 3.13** The continuous and looping transport of a MB with  $6\ \mu\text{m}$  diameter is shown on a Zigzag track for the respective rotational frequency of 2.80 and 3.0 Hz of a rotating magnetic field with an amplitude of 16 kA/m.

**Movie 3.14** The continuous and looping transport of a MB with  $8\ \mu\text{m}$  diameter is shown on a Zigzag track for the respective rotational frequency of 2.0 and 2.50 Hz of a rotating magnetic field with an amplitude of 16 kA/m.

## E.1.2 Movies-Chapter 4

**Movie 4.1** An  $8\ \mu\text{m}$  MB moves continuous in a biased direction on a 1-D array of asymmetric FeCoSiB patterns for a homogeneously rotating magnetic field with an amplitude of 16 kA/m at a frequency of 1.2 Hz. See also Fig. 4.2.

**Movie 4.2** For the high rotational frequency of 3.2 Hz, the MB shows looping motion at an applied magnetic field with an amplitude of 16 kA/m. See also Fig. 4.2.

**Movie 4.3** Two  $8\ \mu\text{m}$  MBs move unidirectional, independent of their starting positions on a 1-D magnetic array, confirming a biased motion induced by the asymmetric patterns. The applied magnetic field has an amplitude of 16 kA/m and rotational frequency of 0.5 Hz.

## E.1.3 Movies-Chapter 5

**Movie 5.1** An ensemble of  $8\ \mu\text{m}$  MBs is moving forward (blue), while MBs with  $4\ \mu\text{m}$  diameter simultaneously move backward (red) for fields changing between  $\vec{a}$  and  $\vec{b}$  with an amplitude of 16 kA/m at a frequency of 4 Hz. Magnetic element edge length

is  $15\ \mu\text{m}$ . Edge to tip separation is  $8\ \mu\text{m}$ . See also Fig. 5.10 a.

**Movie 5.2** On switching between the asymmetric field directions  $\vec{a}^{+15^\circ}$  and  $\vec{b}^{-15^\circ}$ , ensembles of MB with  $8\ \mu\text{m}$  diameter move backward along the curled red paths while beads with  $4\ \mu\text{m}$  diameter move forward from edge to edge along the straight blue paths. Magnetic field amplitude is  $16\ \text{kA/m}$  and the field switching frequency is  $5\ \text{Hz}$ . See Fig. 5.10 b.

**Movie 5.3** Symmetric magnetic fields switching between  $\vec{a}$  and  $\vec{b}$  with the reduced field strength of  $8\ \text{kA/m}$  result in a selective forward motion of  $8\ \mu\text{m}$  MBs, while the  $4\ \mu\text{m}$  MBs are immobile. See Fig. 5.10 c.

**Movie 5.4** Asymmetric magnetic fields switching between  $\vec{a}^{+15^\circ}$  and  $\vec{b}^{-15^\circ}$  with a field strength of  $8\ \text{kA/m}$  allow the  $4\ \mu\text{m}$  particles to move forward, while cause the  $8\ \mu\text{m}$  particles to jump back and forth between two structures. See Fig. 5.10 d.

**Movie 5.5** The backward motion of  $4\ \mu\text{m}$  MBs is changed to forward motion along another pathway different by  $120^\circ$  after rotating the magnetic chip by  $-30^\circ$  for a fixed sequence of symmetric fields switching between  $\vec{a}$  and  $\vec{b}$  with an amplitude of  $16\ \text{kA/m}$  at a frequency of  $1\ \text{Hz}$ . The change in MBs' directed motion is consistent with the motion achieved by applied field sequence 1 and sequence 4, as shown in Tab. 5.1.

**Movie 5.6** The forward moving  $8\ \mu\text{m}$  MBs are locked after rotating the magnetic chip by  $+30^\circ$  for a fixed sequence of symmetric magnetic fields switching between  $\vec{a}$  and  $\vec{b}$  with an amplitude of  $16\ \text{kA/m}$  at a frequency of  $1\ \text{Hz}$ . The change in MBs' motion is consistent with the motion achieved by applied field sequence 1 and sequence 4, as shown in Tab. 5.1. The locked motion is confirmed also for  $-30^\circ$  chip rotation.

**Movie 5.7** The forward motion of  $4\ \mu\text{m}$  MBs is continued to another pathway different by  $60^\circ$  after rotating the magnetic chip by  $+30^\circ$  for a fixed sequence of asymmetric magnetic fields switching between  $\vec{a}^{+15^\circ}$  and  $\vec{b}^{-15^\circ}$  with an amplitude of  $16\ \text{kA/m}$  at a frequency of  $1\ \text{Hz}$ . The achieved control in directed motion is consistent with the results for applied field sequence 2 and sequence 3, as shown in Tab. 5.1.

**Movie 5.8** The backward moving  $8\ \mu\text{m}$  MBs are moved forward along another pathway different by  $120^\circ$  after rotating the magnetic chip by  $+30^\circ$  for a fixed sequence of symmetric fields switching between  $\vec{a}^{+15^\circ}$  and  $\vec{b}^{-15^\circ}$  with an amplitude of  $16\ \text{kA/m}$  at a frequency of  $1\ \text{Hz}$ . The change in MBs' directed motion is consistent with the motion achieved by applied field sequence 2 and sequence 3, as shown in Tab. 5.1.

**Movie 5.9** A population of  $4\ \mu\text{m}$  MBs is selectively moved forward, while  $8\ \mu\text{m}$  MBs are locked with the magnetic fields changing between  $\vec{a}^{+30^\circ}$  and  $\vec{b}_{-180^\circ}^{-30^\circ}$  with an amplitude of  $24\ \text{kA/m}$  at a frequency of  $6\ \text{Hz}$ . A separation efficiency of more than  $97\%$  is confirmed by counting small particles in a heterogeneous mixture of small and large particles. See also Fig. 5.13 a-d.

**Movie 5.10** A population of  $8\ \mu\text{m}$  MBs is moved forward selectively, while  $4\ \mu\text{m}$  MBs are immobile for the magnetic fields changing between  $\vec{a}$  and  $\vec{b}$  with an amplitude of  $8\ \text{kA/m}$  at a frequency of  $6\ \text{Hz}$ . A separation efficiency of more than  $80\%$  is

achievable for large particles. See also Fig. 5.13 e-h.

### E.1.4 Movies-Chapter 6

**Movie 6.1** A  $4\ \mu\text{m}$  MB moves in  $\vec{a}^{0^\circ}$  direction for an x-axis offset = +0.2 kA/m of an in-plane elliptically rotating magnetic field. The applied field amplitudes are  $H_x=6.2$  kA/m and  $H_y=18.6$  kA/m and the field rotational frequency is 1.5 Hz. With a fixed field asymmetry in y-axis, a small asymmetry in +x-axis enables the MB's transport along the  $\vec{a}^{0^\circ}$  magnetic array. See also Fig. 6.2.

**Movie 6.2** A  $4\ \mu\text{m}$  MB moves in  $\vec{a}^{+60^\circ}$  direction for an x-axis offset = -1.3 kA/m of an in-plane elliptically rotating magnetic field. With a fixed field asymmetry in y-axis, a medium asymmetry in -x-axis enables the MB's transport along the  $\vec{a}^{+60^\circ}$  magnetic array.

**Movie 6.3** A  $4\ \mu\text{m}$  MB moves in  $\vec{a}^{-60^\circ}$  direction for an x-axis offset = +2.3 kA/m of an in-plane elliptically rotating magnetic field. With a fixed field asymmetry in y-axis, a large asymmetry in +x-axis enables the MB's transport along the  $\vec{a}^{-60^\circ}$  magnetic array.

**Movie 6.4** Single MBs with  $2\ \mu\text{m}$ ,  $4\ \mu\text{m}$  and  $6\ \mu\text{m}$  diameters move multiaxial with the elliptically rotating in-plane magnetic field at a field frequency of 1.5 Hz. With a fixed field asymmetry in y-axis, an asymmetry of +0.9 kA/m in x-axis results in a simultaneous separating movement of MBs with the multiple sizes. See also Fig. 6.3 a and b.

**Movie 6.5** Single MBs with  $2\ \mu\text{m}$ ,  $4\ \mu\text{m}$  and  $6\ \mu\text{m}$  diameters move uniaxial with the elliptically rotating in-plane magnetic field at a frequency of 1.5 Hz. With a fixed field asymmetry in y-axis, an asymmetry of +2.3 kA/m in x-axis results in a simultaneous uniaxial motion of MBs with multiple sizes. See also Fig. 6.3 a and c.

### E.1.5 Movies-Chapter 7

**Movie 7.1** A *Dictyostelium* cell moved forward with the help of a  $4\ \mu\text{m}$  diameter MB inside the cell for the applied field direction changing between  $\vec{a}$  to  $\vec{b}$ . The field amplitude is 16 kA/m and the field switching frequency is 0.5 Hz. See also Fig. 7.1.

# Acknowledgments

It was an enjoyment for me to work on the project *Magnetic surfaces for the manipulation of superparamagnetic particles*. I humbly express my gratitude to Prof. Dr.-Ing. Jeffrey McCord for offering me this exciting project and trusting in my abilities. During my research over five years in the group of Nanoscale Magnetic Materials - Magnetic Domains, I had excellent working equipment and best imaginable colleagues around me.

I would like to thank all former and current colleagues of the NanoMag-group for their friendly attitude. Thomas von Hofe, Mikhail Kustov, Julia Trützscher, Onur Urs, Babak Mozooni, Rasmus Holländer, Finn Klingbeil, Matic Jovičević Klug, Cai Müller, Farzaneh Karimian, Enno Lage, Findan Block and Simon Jarausch, you guys inspired me. Thanks to Babak and Onur for getting me started by introducing me to the microscopes and equipments in the labs. I thank to Rasmus, Finn, and Findan for their supporting computer experiments on microbeads. The interesting discussions with Enno, Matic, Rasmus, Finn, and Findan always motivated me. The time spent with my office colleagues Onur, Farzaneh, Fasheng and Findan will be among my best memories. I thank my master thesis students namely Qaisar Latif, Sughosh Deshpande and Shehroz Bhatti for their fruitful research contributions to this project. In the last year, the teamwork with Shehroz Bhatti helped to the solution of a complex problem. I do not find words to thank Enno for his contributions at various stages of this project. The useful scientific discussions with Enno and the trust given by Jeffrey played a major role to achieve the goals in this thesis. My gratitude to Enno, Rasmus, Finn, Findan, Farzaneh, Matic and Jeffrey for providing the valuable feedback at different stages during the writing of this thesis. I specially acknowledge the proofreading of this thesis by my colleagues. My sincere thanks to Ellen Riemer for her helpful and happy attitude.

Many thanks to Prof. Dr. Christine Selhuber-Unkel for her idea of manipulating the biological cell with the magnetic particle. I would like to thank Nils Lukat and Sandra Sindt for their valuable contributions. Furthermore, I am thankful to Antonio Malave and other colleagues for their guidance in clean room facilities and Matthias Burmeister and Berndt Neumann for providing the workshop services related to this project. I greatly acknowledge the financial support provided by German Research Foundation (DFG, grant no. MC9/15-1). Lastly, I thank to my parents for their continuous support throughout my academic carrier and to my wife Sidra Umer for being patient with me and supportive of my working routine.



# Publication and Conference

## Publications

- U. Sajjad, R. B. Holländer, F. Klingbeil, and J. McCord. Magnetomechanics of superparamagnetic beads on a magnetic merry-go-round: from micromagnetics to radial looping. *Journal of Physics D: Applied Physics* 50(13):135003, 2017
- U. Sajjad, E. Lage, J. McCord, A trisymmetric magnetic microchip surface for free and two-way directional movement of magnetic microbeads. *Advanced Materials Interfaces* 1801201, 2018

## Conferences

- U. Sajjad, R. B. Holländer, F. Klingbeil, S. Deshpande, Q. Latif, J. McCord. Advanced locomotion of microbeads on ferromagnetic surfaces. *11th International Conference on the Scientific and Clinical Applications of Magnetic Carriers* Vancouver, Canada, 2016
- U. Sajjad, E. Lage, J. McCord. A trisymmetric magnetic microchip surface for unrestricted two-way directional movement of magnetic microbeads. *The Joint European Magnetic Symposia* Mainz, Germany, 2018

# Bibliography

- [1] J. M. Ramsey, S. C. Jacobson, and M. R. Knapp. Microfabricated chemical measurement systems. *Nature Medicine*, 1:1093, 1995.
- [2] K. Sato, M. Tokeshi, T. Odake, H. Kimura, T. Ooi, M. Nakao, and T. Kitamori. Integration of an immunosorbent assay system: analysis of secretory human immunoglobulin a on polystyrene beads in a microchip. *Analytical Chemistry*, 72(6):1144, 2000.
- [3] E. Verpoorte. Focus beads and chips: new recipes for analysis. *Lab Chip*, 3:60N, 2003.
- [4] S. Rampini, P. Li, and G. U. Lee. Micromagnet arrays enable precise manipulation of individual biological analytesuperparamagnetic bead complexes for separation and sensing. *Lab Chip*, 16:3645, 2016.
- [5] B. Lim, P. Vavassori, R. Sooryakumar, and C. G. Kim. Nano/micro-scale magnetophoretic devices for biomedical applications. *Journal of Physics D: Applied Physics*, 50(3):033002, 2017.
- [6] Lab-on-a-chip. [www.gene-quantification.de](http://www.gene-quantification.de).
- [7] M. Schena, D. Shalon, R. W. Davis, and P. O. Brown. Quantitative monitoring of gene expression patterns with a complementary dna microarray. *Science*, 270(5235):467, 1995.
- [8] B.-I. Haukanes and C. Kvam. Application of magnetic beads in bioassays. 11, 1993.
- [9] A. Manz, N. Graber, and H. M. Widmer. Miniaturized total chemical analysis systems: A novel concept for chemical sensing. *Sensors and Actuators B: Chemical*, 1(1):244, 1990.
- [10] A. G. J. Tibbe, B. G. de Grooth, J. Greve, P. A. Liberti, G. J. Dolan, and L. W. M. M. Terstappen. Optical tracking and detection of immunomagnetically selected and aligned cells. *Nature Biotechnology*, 17:1210, 1999.

- 
- [11] B. D. Plouffe, S. K. Murthy, and L. H. Lewis. Fundamentals and application of magnetic particles in cell isolation and enrichment: a review. *Reports on Progress in Physics*, 78(1):016601, 2015.
- [12] L. E. Helseth, T. M. Fischer, and T. H. Johansen. Paramagnetic beads surfing on domain walls. *Phys. Rev. E*, 67:042401, 2003.
- [13] B. Yellen, G. Friedman, and A. Feinerman. Printing superparamagnetic colloidal particle arrays on patterned magnetic film. *Journal of Applied Physics*, 93(10):7331, 2003.
- [14] K. Gunnarsson, P. E. Roy, S. Felton, J. Pihl, P. Svedlindh, S. Berner, H. Lidbaum, and S. Oscarsson. Programmable motion and separation of single magnetic particles on patterned magnetic surfaces. *Advanced Materials*, 17(14):1730, 2005.
- [15] B. B. Yellen, O. Hovorka, and G. Friedman. Arranging matter by magnetic nanoparticle assemblers. *Proceedings of the National Academy of Sciences*, 102(25):8860, 2005.
- [16] H. Lee, A. M. Purdon, and R. M. Westervelt. Manipulation of biological cells using a microelectromagnet matrix. *Applied Physics Letters*, 85(6):1063, 2004.
- [17] R. K. Adair. Constraints on biological effects of weak extremely-low-frequency electromagnetic fields. *Phys. Rev. A*, 43:1039, 1991.
- [18] T. Grahl and H. Märkl. Killing of microorganisms by pulsed electric fields. *Applied Microbiology and Biotechnology*, 45(1):148, 1996.
- [19] N. Pamme and C. Wilhelm. Continuous sorting of magnetic cells via on-chip free-flow magnetophoresis. *Lab Chip*, 6:974, 2006.
- [20] Y. Jung, Y. Choi, K.-H. Han, and A. B. Frazier. Six-stage cascade paramagnetic mode magnetophoretic separation system for human blood samples. *Biomedical Microdevices*, 12(4):637, 2010.
- [21] J. D. Adams, U. Kim, and H. T. Soh. Multitarget magnetic activated cell sorter. *Proceedings of the National Academy of Sciences*, 105(47):18165, 2008.
- [22] A. Chen, T. Byvank, W.-J. Chang, A. Bharde, G. Vieira, B. L. Miller, J. J. Chalmers, R. Bashir, and R. Sooryakumar. On-chip magnetic separation and encapsulation of cells in droplets. *Lab Chip*, 13:1172, 2013.
- [23] P. Li, D. Kilinc, Y. F. Ran, and G. U. Lee. Flow enhanced non-linear magnetophoretic separation of beads based on magnetic susceptibility. *Lab on a Chip*, 13(22):4400, 2013.
- [24] L. Chang, M. Howdyshell, W.-C. Liao, C.-L. Chiang, D. Gallego-Perez, Z. Yang, W. Lu, J. C. Byrd, N. Muthusamy, L. J. Lee, and R. Sooryakumar. Magnetic tweezers-based 3d microchannel electroporation for high-throughput gene transfection in living cells. *Small*, 11(15):1818, 2015.

- 
- [25] B. Lim, S. R. Torati, K. W. Kim, X. Hu, V. Reddy, and C. Kim. Concentric manipulation and monitoring of protein-loaded superparamagnetic cargo using magnetophoretic spider web. *Npg Asia Materials*, 9:e369, 2017.
- [26] C. Murray, E. Pao, P. Tseng, S. Aftab, R. Kulkarni, M. Rettig, and D. Di Carlo. Quantitative magnetic separation of particles and cells using gradient magnetic ratcheting. *Small*, 12(14):1891, 2016.
- [27] K. van Ommering, J. H. Nieuwenhuis, L. J. van Ijzendoorn, B. Koopmans, and M. W. J. Prins. Confined brownian motion of individual magnetic nanoparticles on a chip: Characterization of magnetic susceptibility. *Applied Physics Letters*, 89(14):142511, 2006.
- [28] S. S. Shevkoplyas, A. C. Siegel, R. M. Westervelt, M. G. Prentiss, and G. M. Whitesides. The force acting on a superparamagnetic bead due to an applied magnetic field. *Lab Chip*, 7:1294, 2007.
- [29] X. Hu, S. R. Goudu, S. R. Torati, B. Lim, K. Kim, and C. Kim. An on-chip micromagnet frictionometer based on magnetically driven colloids for nano-bio interfaces. *Lab Chip*, 16:3485, 2016.
- [30] E. Rapoport and G. S. D. Beach. Architecture for directed transport of superparamagnetic microbeads in a magnetic domain wall routing network. *Scientific Reports*, 7:2045, 2017.
- [31] A. van Reenen, Y. Gao, A. H. Bos, A. M. de Jong, M. A. Hulsen, J. M. J. den Toonder, and M. W. J. Prins. Accurate quantification of magnetic particle properties by intra-pair magnetophoresis for nanobiotechnology. *Applied Physics Letters*, 103(4):043704, 2013.
- [32] J. Loehr, M. Loenne, A. Ernst, D. de las Heras, and T. M. Fischer. Topological protection of multiparticle dissipative transport. *Nature Communications*, 7:11745, 2016.
- [33] L. Huang, S. Bian, Y. Cheng, G. Shi, P. Liu, X. Ye, and W. Wang. Microfluidics cell sample preparation for analysis: Advances in efficient cell enrichment and precise single cell capture. *Biomicrofluidics*, 11(1):011501, 2017.
- [34] M. Almeida, García-Montero A. C., and Orfao A. Cell purification: A new challenge for biobanks. *Pathobiology*, 81:261, 2014.
- [35] J. Wu, M. Dong, C. Rigatto, Y. Liu, and F. Lin. Lab-on-chip technology for chronic disease diagnosis. *npj Digital Medicine*, 1:2398, 2018.
- [36] Y. Wang, L. Yu, X. Kong, and L. Sun. Application of nanodiagnostics in point-of-care tests for infectious diseases. *International Journal of Nanomedicine*, 12:4789, 2017.

- [37] J. Gomez-Pastora, X. Xue, I. H. Karampelas, E. Bringas, E. P. Furlani, and I. Ortiz. Analysis of separators for magnetic beads recovery: From large systems to multifunctional microdevices. *Separation and Purification Technology*, 172:16, 2017.
- [38] J. Li, K.-W. Chang, C.-H. Wang, C.-H. Yang, S.-C. Shiesh, and G.-B. Lee. On-chip, aptamer-based sandwich assay for detection of glycated hemoglobins via magnetic beads. *Biosensors and Bioelectronics*, 79:887, 2016.
- [39] T. Salafi, K. K. Zeming, and Y. Zhang. Advancements in microfluidics for nanoparticle separation. *Lab Chip*, 17:11, 2017.
- [40] B. D. Cullity and C. D. Graham. *Introduction to Magnetic Materials*. Wiley-IEEE Press, 2nd edition, 2008.
- [41] G. Vieira, T. Henighan, A. Chen, A. J. Hauser, F. Y. Yang, J. J. Chalmers, and R. Sooryakumar. Magnetic wire traps and programmable manipulation of biological cells. *Phys. Rev. Lett.*, 103:128101, 2009.
- [42] U. Sajjad, R. B. Hollnder, F. Klingbeil, and J. McCord. Magnetomechanics of superparamagnetic beads on a magnetic merry-go-round: from micromagnetics to radial looping. *Journal of Physics D: Applied Physics*, 50(13):135003, 2017.
- [43] A. Sarella, A. Torti, M. Donolato, M. Pancaldi, and P. Vavassori. Two-dimensional programmable manipulation of magnetic nanoparticles on-chip. *Advanced Materials*, 26(15):2384, 2014.
- [44] J. M. D. Coey. *Magnetism and Magnetic Materials*. Cambridge University Press, 2010.
- [45] Q. A. Pankhurst, J. Connolly, S. K. Jones, and J. Dobson. Applications of magnetic nanoparticles in biomedicine. *Journal of Physics D-Applied Physics*, 36(13):R167, 2003.
- [46] micromer-M, [www.micromod.de](http://www.micromod.de) (accessed: March 2016).
- [47] J. Leach, H. Mushfique, S. Keen, R. Di Leonardo, G. Ruocco, J. M. Cooper, and M. J. Padgett. Comparison of faxén’s correction for a microsphere translating or rotating near a surface. *Phys. Rev. E*, 79:026301, 2009.
- [48] M. Zborowski, L. Sun, L. R. Moore, P.S. Williams, and J. J. Chalmers. Continuous cell separation using novel magnetic quadrupole flow sorter. *Journal of Magnetism and Magnetic Materials*, 194(1):224, 1999.
- [49] M. A. M. Gijs. Magnetic bead handling on-chip: new opportunities for analytical applications. *Microfluidics and Nanofluidics*, 1(1):22, 2004.
- [50] Micromagus. [www.micromagus.de](http://www.micromagus.de).
- [51] D. V. Berkov, K. Ramstöck, and A. Hubert. Solving micromagnetic problems. towards an optimal numerical method. *physica status solidi (a)*, 137(1):207, 1993.

- 
- [52] J. McCord. Progress in magnetic domain observation by advanced magneto-optical microscopy. *Journal of Physics D: Applied Physics*, 48(33):333001, 2015.
- [53] A. Hubert and R. Schäfer. *Magnetic domains: The analysis of magnetic microstructures*. Springer, Berlin, 1998.
- [54] D. Rugar, H. J. Mamin, P. Guethner, S. E. Lambert, J. E. Stern, I. McFadyen, and T. Yogi. Magnetic force microscopy: General principles and application to longitudinal recording media. *Journal of Applied Physics*, 68(3):1169, 1990.
- [55] W. Rave A. Hubert and S. L. Tomlinson. Imaging magnetic charges with magnetic force microscopy. *Physica Status Solidi B Basic Research*, 204:817, 1997.
- [56] Technical note TN00031, [www.nanosurf.com](http://www.nanosurf.com).
- [57] C. A. Schneider, W. S. Rasband, and K. W. Eliceiri. Ih image to imagej: 25 years of image analysis. *Nature Methods*, 9:671, 2012.
- [58] C. P. Gooneratne, R. Kodzius, F. Li, I. G. Foulds, and J. Kosel. On-chip magnetic bead manipulation and detection using a magnetoresistive sensor-based micro-chip: Design considerations and experimental characterization. *Sensors*, 16(9):1369, 2016.
- [59] D. T. Grob, N. Wise, O. Oduwole, and S. Sheard. Magnetic susceptibility characterisation of superparamagnetic microspheres. *Journal of Magnetism and Magnetic Materials*, 452:134, 2018.
- [60] E. Rapoport and G. S. D. Beach. Transport dynamics of superparamagnetic microbeads trapped by mobile magnetic domain walls. *Phys. Rev. B*, 87:174426, 2013.
- [61] M. Monticelli, D. V. Conca, E. Albisetti, A. Torti, P. P. Sharma, G. Kidiyoor, S. Barozzi, D. Parazzoli, P. Ciarletta, M. Lupi, D. Petti, and R. Bertacco. Magnetic domain wall tweezers: a new tool for mechanobiology studies on individual target cells. *Lab Chip*, 16:2882, 2016.
- [62] M. Monticelli, E. Albisetti, D. Petti, D. V. Conca, M. Falcone, P. P. Sharma, and R. Bertacco. Towards an on-chip platform for the controlled application of forces via magnetic particles: A novel device for mechanobiology. *Journal of Applied Physics*, 117(17):17B317, 2015.
- [63] A. D. Henriksen, N. Rozlosnik, and M. F. Hansen. Geometrical optimization of microstripe arrays for microbead magnetophoresis. *Biomicrofluidics*, 9(5):054123, 2015.
- [64] U. Sajjad, E. Lage, and J. McCord. A trisymmetric magnetic microchip surface for free and two-way directional movement of magnetic microbeads. *Advanced Materials Interfaces*, 0:1801201, 2018.
- [65] P. Tierno, F. Sagus, T. H. Johansen, and T. M. Fischer. Colloidal transport on magnetic garnet films. *Phys. Chem. Chem. Phys.*, 11:9615, 2009.

- [66] Y. Ouyang, M. A. Tahir, D. J. Lichtenwalner, and B. B. Yellen. Origin of multiplexing capabilities of multifrequency magnetic ratchets. *Phys. Rev. E*, 85:041407, 2012.
- [67] W. Zhao, T. Zhu, R. Cheng, Y. Liu, J. He, H. Qiu, L. Wang, T. Nagy, T. D. Querec, E. R. Unger, and L. Mao. Label-free and continuous-flow ferrohydrodynamic separation of hela cells and blood cells in biocompatible ferrofluids. *Advanced Functional Materials*, 26(22):3990, 2016.
- [68] E. Monachino, Lisanne M. Spenkelink, and A. M. van Oijen. Watching cellular machinery in action, one molecule at a time. *The Journal of Cell Biology*, 2016.
- [69] S. J. Annesley and P. R. Fisher. Dictyostelium discoideum—a model for many reasons. *Molecular and Cellular Biochemistry*, 329(1):73, 2009.
- [70] K. Norregaard, L. Jauffred, K. Berg-Srensen, and L. B. Oddershede. Optical manipulation of single molecules in the living cell. *Phys. Chem. Chem. Phys.*, 16:12614, 2014.
- [71] A.H.B. de Vries, B. E. Krenn, R. van Driel, and J. S. Kanger. Micro magnetic tweezers for nanomanipulation inside live cells. *Biophysical Journal*, 88(3):2137, 2005.
- [72] B. G. Hosu, K. Jakab, P. Bánki, F. I. Tóth, and G. Forgacs. Magnetic tweezers for intracellular applications. *Review of Scientific Instruments*, 74(9):4158, 2003.
- [73] C. Wilhelm, C. Rivière, and N. Biais. Magnetic control of dictyostelium aggregation. *Phys. Rev. E*, 75:041906, 2007.
- [74] K. E. McCloskey, J. J. Chalmers, and M. Zborowski. Magnetic cell separation: characterization of magnetophoretic mobility. *Analytical Chemistry*, 75(24):6868, 2003.
- [75] M. Helou, M. Reisbeck, S. F. Tedde, L. Richter, L. Bar, J. J. Bosch, R. H. Stauber, E. Quandt, and O. Hayden. Time-of-flight magnetic flow cytometry in whole blood with integrated sample preparation dagger. *Lab on a Chip*, 13(6):1035, 2013.
- [76] M. D. Krebs, R. M. Erb, B. B. Yellen, B. Samanta, A. Bajaj, V. M. Rotello, and E. Alsberg. Formation of ordered cellular structures in suspension via label-free negative magnetophoresis. *Nano Letters*, 9(5):1812, 2009.
- [77] F. Martinez-Pedrero and P. Tierno. Magnetic propulsion of self-assembled colloidal carpets: Efficient cargo transport via a conveyor-belt effect. *Phys. Rev. Applied*, 3:051003, 2015.
- [78] B. Lim, V. Reddy, X. Hu, K. Kim, M. Jadhav, R. Abedini-Nassab, Y.-W. Noh, Y. T. Lim, B. B. Yellen, and C. Kim. Magnetophoretic circuits for digital control of single particles and cells. *Nat Commun*, 14(5):3846, 2014.